Aus dem Institut für Radiologie, Klinik für Strahlenheilkunde
der Medizinischen Fakultät Charité – Universitätsmedizin Berlin

DISSERTATION

**Quantitative Imaging Biomarkers to Characterize the Tumor
Microenvironment in Liver Tumors for Tumor Detection and Therapy
Response Assessment**

**Quantitative bildbasierte Prädiktoren zur Charakterisierung der
Tumormikroumgebung in Lebertumoren für die Tumordetektierung und
Evaluierung des Therapieansprechens**

zur Erlangung des akademischen Grades
Medical Doctor - Doctor of Philosophy (MD/PhD)

vorgelegt der Medizinischen Fakultät
Charité – Universitätsmedizin Berlin

von

Tabea Borde

Datum der Promotion: 26.06.2022

Table of contents

I. Abbreviations

HCC	hepatocellular carcinoma
NASH	non-alcoholic steatohepatitis
MRI	magnetic resonance imaging
DEB-TACE	drug-eluting bead transarterial chemoembolization
TME	tumor microenvironment
ADC	apparent diffusion coefficient
DWI	diffusion-weighted imaging
HIF-1α	hypoxia induced factor-1
VEGF	vascular endothelial growth factor
DCE-MRI	dynamic contrast-enhanced magnetic resonance imaging
ECM	extracellular matrix
pHe	extracellular pH
BIRDS	biosensor imaging of redundant deviation in shifts
AST	aspartate aminotransferase
ALT	alanine aminotransferase
MOLLI	modified look-locker inversion recovery sequence
RE	relative enhancement
H&E	hematoxylin and eosin
PCNA	proliferating cell nuclear antigen
TUNEL	terminal deoxynucleotidyl transferase dUTP nick end labeling
LA-ICP-MS	laser ablation inductively coupled plasma mass spectrometry
SASHA	saturation recovery single-shot acquisition
CEST	chemical exchange saturation transfer

II. Abstract

Deutsch

Diese Forschung wurde original publiziert in:

1. *Borde T, Laage Gaupp F, Geschwind JF, Savic LJ, Miszczuk M, Rexha I, Adam L, Walsh JJ, Huber S, Duncan JS, Peters DC, Sinusas A, Schlachter T, Gebauer B, Hyder F, Coman D, van Breugel JMM, Chapiro J. Idarubicin-Loaded ONCOZENE Drug-Eluting Bead Chemoembolization in a Rabbit Liver Tumor Model: Investigating Safety, Therapeutic Efficacy, and Effects on Tumor Microenvironment. J Vasc Interv Radiol. 2020 Oct;31(10):1706-1716.e1.*

2. *Keller S, Borde T, Brangsch J, Reimann C, Kader A, Schulze D, Buchholz R, Kaufmann JO, Karst U, Schellenberger E, Hamm B, Makowski MR. Assessment of the hepatic tumor extracellular matrix using elastin-specific molecular magnetic resonance imaging in an experimental rabbit cancer model. Sci Rep. 2020 Nov 27;10(1):20785.*

3. *Keller S, Borde T, Brangsch J, Adams LC, Kader A, Reimann C, Gebert P, Hamm B, Makowski M. Native T1 Mapping Magnetic Resonance Imaging as a Quantitative Biomarker for Characterization of the Extracellular Matrix in a Rabbit Hepatic Cancer Model. Biomedicines. 2020 Oct 13;8(10):412.*

Dieser Abstract wurde anteilig aus den oben genannten Publikationen übersetzt und adaptiert.

Zielsetzung:

Ziel der Studien war die Etablierung nicht-invasiver, quantitativer Prädiktoren mittels multiparametrischer MRT (mpMRT) für eine frühere Identifizierung solider Lebertumoren und Charakterisierung tumor- sowie therapie-assoziierter Veränderungen des Tumormikromilieus.

Methodik:

39 weiße Neuseeländer Kaninchen mit orthotop implantierten VX2 Lebertumoren wurden entweder in diagnostische Studienarme randomisiert (N=30) bzw. durchliefen transarterielle Chemoembolisation mit Idarubicin-beladenen Oncozene® Mikrosphären in einem Durchmesser von 40µm (N=5) oder 100µm (N=4). Im diagnostischen Studienarm erfolgte die 3T mpMRT 14, 21 und 28 Tage nach Tumorimplantation und beinhaltete neben einer MOLLI Sequenz für T1 Mapping die Applikation eines Elastin-spezifischen MRT-Kontrastmittels (ESMA, N=12) zur Beurteilung der extrazellulären Matrix. In der Therapiegruppe erfolgte die mpMRT 24-72h post-interventionell und beinhaltete neben dynamischen, kontrastverstärkten (DCE-MRT) und Diffusions-gewichteten (DWI) MRT-Sequenzen eine Biosensor imaging of redundant deviation

in shifts (BIRDS) Sequenz zur Beurteilung des extrazellulären pHs (pHe). Die laborchemische und ex-vivo Analyse umfasste histopathologische und immunhistochemische Färbungen, konfokale Fluoreszenz-Mikroskopie sowie die Elementen-spezifische Laserablations-Massenspektrometrie (LA-ICP-MS) zur Bestimmung der Elastin-spezifischen Kontrastmitteldistribution.

Ergebnisse:

Im nativen T1 Mapping gelang eine Unterscheidung zwischen dem vitalen Tumorrand, dem partiell nekrotisierten Tumorkern und der peritumoralen Umgebung (F(1,43; 34,26) = 106,93, P<0,001). Die Anwendung von ESMA ergab eine verbesserte Abgrenzbarkeit der einzelnen Tumorregionen im Vergleich zu Gadobutrol (χ^2(4) = 65,87; P<0,001) und korrelierte mit der histopathologisch (r=0.84, P<0.001) und mittels LA-ICP-MS gesicherten (r=0,73, P<0,01) extrazellulären Elastinakkumulation. Embolisierte Tumore zeigten eine Devaskularisierung des zuvor hyperenhancenden Tumorrandes in der DCE-MRT (mittleres arterielles Enhancement [%] 8 ± 12 vs. Kontrollen 36 ± 51, P=0,07) sowie eine Zunahme der Diffusionskapazität in DWI (apparenter Diffusionskoeffizient [x10^{-3}mm^2/s] 1,89 ± 0,18 vs. Leber 2,34 ± 0,18, P=0,002) in beiden Mikrosphärengrößen. BIRDS zeigte eine deutliche Tumorazidose prä- (mittlerer pHe Tumor 6,79 ± 0,08 vs. Leber 7,13 ± 0,08, P=0,02) und post-therapeutisch (Tumor 6,8 ± 0,06 vs. Leber 7,1 ± 0,04, P=0,007). Die mittels der mpMRT quantifizierten Therapieeffekte korrelierten mit den Labor- und histopathologischen Analysen in beiden Mikrosphärendurchmessern.

Schlussfolgerung:

Die Kombination aus unterschiedlichen, quantitativen, nicht-invasiven Prädiktoren in der mpMRT erlaubt, den Tumor und die Tumormikroumgebung verlässlich zu charakterisieren sowie therapiebezogene Veränderungen zu quantifizieren. Dies ermöglicht, Lebertumore in früheren Stadien zu detektieren und das Therapieansprechen nach lokoregionären Therapien vorauszusagen.

English

This research was originally published in:

1. *Borde T, Laage Gaupp F, Geschwind JF, Savic LJ, Miszczuk M, Rexha I, Adam L, Walsh JJ, Huber S, Duncan JS, Peters DC, Sinusas A, Schlachter T, Gebauer B, Hyder F, Coman D, van Breugel JMM, Chapiro J. Idarubicin-Loaded ONCOZENE Drug-Eluting Bead Chemoembolization in a Rabbit Liver Tumor Model: Investigating Safety, Therapeutic Efficacy, and Effects on Tumor Microenvironment. J Vasc Interv Radiol. 2020 Oct;31(10):1706-1716.e1.*

2. *Keller S, Borde T, Brangsch J, Reimann C, Kader A, Schulze D, Buchholz R, Kaufmann JO, Karst U, Schellenberger E, Hamm B, Makowski MR. Assessment of the hepatic tumor extracellular matrix using elastin-specific molecular magnetic resonance imaging in an experimental rabbit cancer model. Sci Rep. 2020 Nov 27;10(1):20785.*

3. *Keller S, Borde T, Brangsch J, Adams LC, Kader A, Reimann C, Gebert P, Hamm B, Makowski M. Native T1 Mapping Magnetic Resonance Imaging as a Quantitative Biomarker for Characterization of the Extracellular Matrix in a Rabbit Hepatic Cancer Model. Biomedicines. 2020 Oct 13;8(10):412.*

This abstract was adapted from the above-mentioned publications.

Purpose:

These studies aimed to employ multiparametric MRI (mpMRI) to establish non-invasive, quantitative imaging biomarkers for the early detection of solid liver tumors and the characterization of tumor- and therapy-associated microenvironmental tumor alterations.

Methods:

39 New Zealand White rabbits with orthotopically implanted VX2 liver tumors were subjected to diagnostic study arms (N=30) or underwent drug-eluting bead transarterial chemoembolization (DEB-TACE) with either 40µm (N=5) or 100µm (N=4) idarubicin-loaded Oncozene® microspheres. 3T mpMRI was performed 14, 21, and 28 days following tumor implantation in the diagnostic study groups including a MOLLI sequence for native T1 mapping and a gadobutrol-based and elastin-specific, molecular MRI contrast agent (ESMA, N=12) to evaluate the extracellular matrix. In the treatment arm, mpMRI was performed 24-72h post-TACE and included dynamic contrast-enhanced (DCE) MRI, diffusion-weighted imaging (DWI), and biosensor imaging of redundant deviation in shifts (BIRDS) assessing the extracellular pH (pHe). Laboratory parameters and ex-vivo analysis included histopathological and histochemical staining,

fluorescence confocal microscopy, and element-specific, laser ablation inductively coupled mass spectrometry (LA-ICP-MS) for gadolinium-bound elastin contrast distribution.

Results:

Native T1 mapping accurately distinguished the viable tumor rim from the partly necrotic tumor center and peritumoral surrounding ($F(1.43, 34.26) = 106.93$, $P<0.001$). MpMRI using the elastin-specific contrast agent demonstrated a superior discrimination of the different tumor regions compared to gadobutrol ($\chi^2(4) = 65.87$; $P<0.001$) and significantly correlated with elastin fiber depositions quantified in histopathology ($R = 0.84$, $P<0.001$) and LA-ICP-MS ($R=0.73$, $P<0.01$). Embolized tumors demonstrated a devascularization of the previously hyper-enhanced, viable tumor rim in DCE-MRI (mean arterial enhancement [%] 8 ± 12 vs. controls 36 ± 51, $P=0.07$) as well as post-procedural increases in diffusion in DWI (apparent diffusion coefficient [$x10^{-3}mm^2/s$] 1.89 ± 0.18 vs. liver 2.34 ± 0.18, $P=0.002$) in both microsphere sizes. BIRDS demonstrated profound tumor acidosis pre- (mean pHe tumor 6.79 ± 0.08 vs. liver 7.13 ± 0.08, $P=0.02$), and post-TACE (tumor 6.8 ± 0.06 vs. liver 7.1 ± 0.04, $P=0.007$). The therapeutic effects quantified by mpMRI were confirmed in laboratory analyses and histopathology in both microsphere diameters.

Conclusions:

The combination of different, quantitative, non-invasive imaging biomarkers in mpMRI allows for a reliable characterization and quantification of the tumor and tumor microenvironmental alterations and therapy-related changes following DEB-TACE. Therefore, mpMRI may be used to detect liver tumors in earlier stages and predict tumor response to locoregional therapies.

III. Manteltext

Introduction

Hepatocellular carcinoma (HCC) is the third leading cause of cancer-related deaths worldwide. Incidence rates are still increasing, particularly in Western populations, developing countries in Asia, and northern Africa. This is in part due to the rise of obesity-related non-alcoholic steatohepatitis (NASH) and the fact that hepatitis B and C infection rates continue to persist (1). In addition to laboratory parameters, the current guideline-approved approach to diagnose HCC encompasses radiological imaging such as liver ultrasound, computed tomography, or magnetic resonance imaging (MRI). MRI represents the most sensitive radiological technique to diagnose HCC and can replace biopsies in larger lesions (2, 3). Due to its characteristic arterial blood supply, HCC typically presents with early contrast deposition in the arterial contrast phase and wash-out patterns in the portalvenous and venous phases. However, in a majority of patients, HCC develops on the basis of liver cirrhosis, a state of chronic liver injury characterized by an irreversible scarring and fibrotic remodeling of the liver parenchyma. These background tissue abnormalities can render an early detection of a tumor formation more challenging. As a result of the late onset of clinical symptoms, more than 70% of patients with HCC are diagnosed with an intermediate to advanced stage disease with no amenability for curative treatment (1, 4). The prognosis of patients with an advanced disease is dismal with a 5-year survival rate of < 15% and a median overall survival of 6 to 20 months following diagnosis (5, 6). Therefore, early detection of HCC has a considerable impact on the clinical outcome of the patient. The guideline-approved mainstay of palliative therapy in this large subset of patients are locoregional, liver-directed intra-arterial therapies such as conventional or drug-eluting bead (DEB) transarterial chemoembolization (TACE) (7, 8). These intra-arterial therapies rely on the dual blood supply of the liver and comprise different techniques, chemotherapeutic agents and embolic vectors to locally induce tumor cell death with a reduced systemic drug exposure. These treatments have been shown to prolong overall survival or down-size and bridge the tumor to liver transplant (7, 9). The efficacy of these locoregional, image-guided therapies is largely impacted by a high individuality and variability of the biochemical composition of the tumor microenvironment (TME), which plays a critical role in tumor viability, growth potential, local aggressiveness and tumor responsiveness to treatment (10). The TME largely consists of stromal cells, vascular networks, and an extracellular matrix dominated by collagen and elastin proteins. This highly individual composition of the TME contributes to the carcinogenic phenotype and profoundly influences the tumor's susceptibility to

standardized therapy regimes (10). Particularly the tumor response to hypoxia which is intensified in perpetually proliferating tumor cells without an adequate oxygen perfusion, considerably enhances tumor angiogenesis, hyperglycolysis and acidification of the tumor environment (11-13). These distinctive transformations in pathologically altered tumor tissues are increasingly assessed non-invasively with the help of MRI. The rapid tumor progression of HCC often results in central necrosis within the tumor. The length and duration of tumor hypoxia determines the extent of tumor necrosis (14). The resulting breach of cellular membranes and the degradation of the cellular integrity is inversely correlated to the degree of water diffusion inside the tissue. Thus, increased mobility of water molecules due to dispersed, necrotic cell debris and an increased tumor vascularity lead to a characteristic diffusion profile of HCC that can be non-invasively quantified with the apparent diffusion coefficient (ADC) map in MRI-based diffusion-weighted imaging (DWI) (15). The impedance of water molecule diffusion is, therefore, directly attributable to the tissue cellularity and produces low signal attenuation. By contrast, an increase in the water molecule dynamic due to disintegrated cell compounds generates high ADC values. Thus, DWI presents an auxiliary MRI sequence in the detection and evaluation of aberrant tissue patterns in HCC.

Previous studies of HCC have shown that a mild hypoxic environment leads to an overexpression of hypoxia induced factor-1 (HIF-1α), which stimulates tumor growth, suppresses cell apoptosis, and inhibits tumor differentiation. These effects culminate to form an aggressive, anaplastic tumor cell proliferation (12, 16, 17). Tumor hypoxia in HCC may be even exacerbated by intra-arterial therapies such as TACE when only marginally affected tumor cells do not undergo cell death (18). Insufficient oxygen supply further stimulates the expression of angiogenic mediators such as the vascular endothelial growth factor (VEGF) to expand and reinstate the vascular network of HCC (19). This predominantly HIF-1α induced and dysregulated neo-angiogenesis leads to the characteristic hypervascularity seen in the HCC phenotype (20). In fluoroscopy, this hypervascular vessel pattern is useful for localizing the tumor and forms a visible contrast blush distinct from normal liver parenchyma. Tumor associated neo-vasculature is a hallmark of cancer which is already apparent in premalignant, non-invasive lesions such as in situ carcinomas (10). Therefore, perfusion and permeability-based imaging represent a useful tool to detect early hypervascularity and potentially identify HCC in earlier stages. Within this context, dynamic contrast-enhanced MRI (DCE-MRI) was established to accurately visualize perfusion patterns as well as intra- and extravascular volume fractions (21, 22).

The tumor response to hypoxia and the influential effects of HIF-1α on the TME gradually change in the composition of the extracellular matrix (ECM). Recently, HIF-1α was found to directly

catalyze the cross-linkage of collagen and elastin fibers, as the most abundant structural proteins of the ECM (23). This hypoxia-driven ECM remodeling and the generally enhanced production of ECM components in the course of tumorigenesis contribute to an increased ECM stiffness (24). Schrader et al. have demonstrated that a pathologically reorganized, increased matrix stiffness is directly correlated with tumor cell proliferation and chemotherapeutic resistance in HCC (25). Therefore, an increase in elastin and collagen fibers in the ECM is associated with an increase in the cumulative incidence of HCC (26). Furthermore, elastin is an elastic protein forming an essential component to enable the elasticity of blood vessels. Correspondingly, elastin is also found in subendothelial spaces of sinusoids and with increasing quantity in the aberrant vascular network of HCC due to portal hypertension induced fibrotic remodeling within the liver and tumor (27). Recent attempts to non-invasively study the extent of ECM remodeling led to the development of a molecular elastin-specific MR contrast agent with the capacity to successfully image and quantify the elastin content in cardiovascular diseases on the basis of signal intensity (28-30). The successful implementation of this non-invasive ECM characterization in cardiovascular imaging can be applied to oncologic imaging including the process of liver cirrhosis transforming into HCC. Another potential approach to improve the detectability of HCC in clinical routine is native T1 mapping. Without the use of a contrast medium, native T1 mapping measures longitudinal T1 relaxation times, which primarily depend on the extracellular water volume fraction and vary significantly across different tissue types (31). Consequently, an increased interstitial fluid accumulation such as in tissue edema (32), or an increased, fibrotic ECM reformation were successfully exposed in various organs with high signaling native T1 mapping (33-36). Thus far, there is limited data on the characterization of the TME in liver tumors using native T1 mapping. The substantial impact of a predominantly hypoxia-driven interaction between the tumor and the TME on the extracellular tumor milieu is further intensified by an extensively increased glucose metabolism in cancer cells (37). The tumor-associated reliance on oxygen-independent glycolysis rather than mitochondrial oxidative phosphorylation is further accelerated by HIF-1α induced pathways. This seemingly counterintuitive hyperglycolysis not only preserves tumor energy coverage but also leads to the inevitable metabolic synthesis of large amounts of by-products such as lactate and protons. Their active extracellular transfer and deposition in the interstitial space gradually acidify the surrounding TME. This local, extracellular acidosis creates an intricate tumor niche with pro-tumorigenic and immune evading properties that has been found to be increasingly associated with tumor aggressiveness and resistance to therapy (38, 39). Thus, the extracellular pH (pHe) of the TME can be used as an early indicator for tumor progression as well as therapy responsiveness (40). Based on the complex role of TME acidification in the course of

carcinogenesis, Coman et al. have successfully established a quantitative MR biosensor imaging of redundant deviation in shifts (BIRDS) sequence which is based on the chemical shifts of non-exchangeable protons from macrocyclic chelates to non-invasively generate in vivo pHe maps. The use of this MR-based quantification of the local tumor pH relative to unaffected parenchyma can serve as a clinical and non-invasive biomarker to detect metabolic aberrations in early cancer development and longitudinally assess anticancer therapy responsiveness (41).

Therefore, the purpose of this translational work was to employ multiparametric MRI in order to investigate and establish non-invasive, quantitative imaging biomarkers for the early detection of solid liver tumors. In a second step, this comprehensive multiparametric MRI biomarker panel was used to monitor tumor microenvironmental changes induced by locoregional therapy in a translational orthotopic liver cancer animal model.

Methodology

This research was originally published in:

1. *Borde T, Laage Gaupp F, Geschwind JF, Savic LJ, Miszczuk M, Rexha I, Adam L, Walsh JJ, Huber S, Duncan JS, Peters DC, Sinusas A, Schlachter T, Gebauer B, Hyder F, Coman D, van Breugel JMM, Chapiro J. Idarubicin-Loaded ONCOZENE Drug-Eluting Bead Chemoembolization in a Rabbit Liver Tumor Model: Investigating Safety, Therapeutic Efficacy, and Effects on Tumor Microenvironment. J Vasc Interv Radiol. 2020 Oct;31(10):1706-1716.e1.*

2. *Keller S, Borde T, Brangsch J, Reimann C, Kader A, Schulze D, Buchholz R, Kaufmann JO, Karst U, Schellenberger E, Hamm B, Makowski MR. Assessment of the hepatic tumor extracellular matrix using elastin-specific molecular magnetic resonance imaging in an experimental rabbit cancer model. Sci Rep. 2020 Nov 27;10(1):20785.*

3. *Keller S, Borde T, Brangsch J, Adams LC, Kader A, Reimann C, Gebert P, Hamm B, Makowski M. Native T1 Mapping Magnetic Resonance Imaging as a Quantitative Biomarker for Characterization of the Extracellular Matrix in a Rabbit Hepatic Cancer Model. Biomedicines. 2020 Oct 13;8(10):412.*

The following text describes the already published Material and Methods in detail.

Animal tumor model

All three translational experimental studies (in the following named study A, B and C) were designed in view of the ARRIVE guidelines (42) and conducted in accordance with institutional guidelines under approved Institutional Animal Care and Use Committee protocols as well as approved Animal Welfare Act and regulations of the Federation of Laboratory Animal Science Associations. Adult New Zealand white rabbits (weight 3.8 ± 0.4 kg, Charles Liver Laboratories) were considered as the appropriate tumor model (43, 44). In all three translational studies, tumor implantation was performed equally as previously described (45). In brief, VX2 tumors were injected intramuscularly into the hind limb of donor rabbits and allowed to grow for three weeks until a desirable tumor size of 1-2 cm was obtained. Subsequently, the tumor chunks were explanted and processed. Approximately 0.4 ml of the harvested tumor medium were injected into the left hepatic lobe of the recipient rabbits via mini laparotomy. Auxiliary heat support was applied. The tumors were at least grown for another 2 weeks until a desirable size of 1-2 cm was reached, and further experimental conductance was initialized. All rabbits were pre-operatively anesthetized with either subcutaneous injection of medetomidine hydrochloride (0.25 mg/kg body

weight), and ketamine hydrochloride (30 mg/kg body weight) or a combination of ketamine (30 mg/kg body weight), acepromazine (2 mg/kg body weight), and xylazine (5 mg/kg body weight) depending on availability. Post-operative analgesia was achieved with either a nonsteroidal anti-inflammatory drug (e.g. carprofen 4 mg/kg body weight) for three days or an opioid analgesic (buprenorphine 0,02 mg/kg body weight) following more invasive procedures.

Overall experimental design

In order to ensure an operational overview, the overall experimental design of the three translational studies will be described individually.

The first diagnostic study (A) was designed to evaluate the diagnostic accuracy of T1 mapping and involved a total of 27 rabbits that were randomly stratified into three groups (N = 9). Terminal MRI was acquired 14, 21 and 28 days following intrahepatic tumor implantation (Figure 1). Immediately after image acquisition, animals were sacrificed, after which tumor and liver samples were extracted and processed for histopathological evaluation accordingly.

As part of the aforementioned diagnostic study, twelve rabbits were additionally randomized into four groups following intrahepatic tumor implantation in order to investigate the applicability and efficacy of the elastin-specific contrast agent (study B). Therefore, three groups (N = 3) underwent MRI on two consecutive days equally either two (day 14 + 15), three (day 21 + 22) or four (day 28 + 29) weeks after intrahepatic tumor implantation. Animals were sacrificed after image acquisition. Liver and tumor samples were harvested, and immediately sectioned for histopathological processing as described in the first diagnostic study. An additional longitudinal study arm (N = 3) was subjected to MRI on two consecutive days (14 + 15 and 28 + 29 days) after the original intrahepatic tumor implantation (Figure 2).

The third and preclinical treatment study (C) involved twelve rabbits that were randomly assigned to DEB-TACE with 40 µm (N = 5) or 100 µm (N = 4) Oncozene® microspheres or an untreated, control group (N = 3, Figure 3). In order to investigate potential treatment-induced organ impairments, blood samples were collected pre-TACE, and at 5 min, 24 h and 48 h post-procedurally. Terminal, multiparametric MRI including perfusion, diffusion and pHe-weighted sequences was acquired within 24-72 hours post-TACE or at a simultaneous timepoint for untreated controls. Following image acquisition, animals were euthanized and necropsied. Liver tumors were immediately explanted, sectioned and processed for immunofluorescent and histopathological evaluation.

Image acquisition and analysis

In all three translational study arms, MRI was performed under deep sedation in a 3 Tesla clinical scanner (mMR Biograph for the two diagnostic study groups [A+B], and Prisma Siemens Medical Solutions, Erlangen, Germany for the TACE treatment study arm [C]) using a clinically approved 15-channel RF coil. General image acquisition included T1-weighted and T2-weighted sequences for anatomical imaging in all study groups (repetition time [TR]/ echo time [TE] 5.2/2.5 ms, field of view [FOV] 200 x 200 mm^2, 128 x 128 matrix). T2-weighted spin echo scout images were acquired with respiratory gating.

The first diagnostic study arm (A) specifically included a conventional, anatomical T2-weighted (TR/TE 5500/90 ms, voxel size $0.5 \times 0.5 \times 3.0$ mm^3, FOV 180×180 mm^2) and T1-weighted Dixon sequence (TR/TE 4.76/1.49 ms, voxel size $0.5 \times 0.5 \times 2.0$ mm^3, FOV 272×272 mm^2) in combination with a steady-state precession readout single-shot modified look-locker inversion recovery sequence (MOLLI) (TR/TE 1155/2.45 ms, voxel size $1.0 \times 1.0 \times 3.0$ mm^3, FOV 250×250 mm^2) to acquire native T1 maps. The T1 maps were automatically computed on a pixel-by-pixel basis and immediately available after MRI acquisition. In the generated color map, the signal intensity (SI) of each pixel reflected the absolute T1 value of the underlying tissue. Tumor regions were manually segmented into a central, marginal and peritumoral region.

The second diagnostic study arm (B) additionally included an elastin-specific molecular contrast agent (ESMA; Lantheus Medical Imaging, North Billerica, MA) composed of a D-amino-acid homophenylalanine which is linked to a gadolinium-diethylenetriaminepentaacetic acid complex (30). Animals were scanned on two consecutive days with an intravenous injection of gadobutrol (Gadovist 1.0 mmol/ml, Bayer Healthcare AG, Berlin) on the first day and the intravenous administration of the elastin-specific contrast agent in a clinical dose of 0.2 mmol/kg on the second day. Additional pre-contrast scans were conducted prior to the application of the elastin-specific probe to preclude any residual intrahepatic gadobutrol deposition. A three-dimensional gradient-recalled-echo (GRE) sequence, which is routinely performed for liver imaging in clinical practice due to its thin-section images with fat saturation and high signal-to-noise ratio (46, 47), was acquired before and 20 minutes after contrast injection (T1 volumetric interpolated breath-hold examination (VIBE), TR/TE 5.0/2.18 ms, FOV 180 x 180 mm^2, voxel size 0.7 x 0.7 x 1.0 mm^3, NSA 2). Tumors were similarly segmented into a central and marginal zone. The relative enhancement (RE) was calculated using the formula: $RE = \frac{(SI_{postcontrast} - SI_{precontrast})}{SI_{precontrast}}$

Within the third, translational embolization study (C), contrast-enhanced multidetector CT was acquired pre-TACE to ensure adequate tumor growth prior to the liver-directed intervention. Apart

from common anatomical T1- and T2-weighted sequences, multiparametric MRI included specific sequences to gain a comprehensive estimation of alterations within the TME of untreated liver tumors as well as TME changes following anti-cancer therapy. Tumor perfusion and vascularity were assessed on DCE T1-weighted images using a 3D VIBE sequence with CAIPIRINHA parallel imaging (48, 49) (TR/TE 3.45/1.28 ms, matrix 192 x100, FOV 200 x 120 mm^2, 1 x 2 x 2.5 mm^3). By means of repeated image acquisition before, during, and after the bolus injection of 0.1 mmol/kg intravenous gadolinium (Magnevist, Bayer Healthcare, Germany), consecutively generated DCE-MRI data maps depicted the percentage of tumor and liver enhancement at arterial and venous contrast phases compared to baseline non-contrast imaging data. DWI-MRI contributed to the evaluation of cellularity and diffusion using different b-values (50-800 s/mm^2). The corresponding ADC values were automatically extracted by means of a region of interest placement in the tumor core, tumor rim and normal extra-tumoral parenchyma in single diffusion-weighted images. Subsequently, they were depicted on corresponding ADC maps. In order to non-invasively quantify the extracellular pH, the BIRDS sequence was acquired by measuring chemical shifts of pH sensitive resonances from the macrocyclic chelate DOTP8- (1,4,7,10-tetraazacyclododecane-1,4,7,10-tetrakis-(methylenephospho-nate)) complexed with the paramagnetic TmDOTP5- (Macrocyclis, Inc., Plano, TX) (50, 51) (TR 8 ms, FOV 200 x 200 x 250 mm^2, voxel resolution 8 x 8x 10 mm^3, 2197 rectangular encoding steps. A dual band Shinnar-Le Roux pulse of 640 μs was used for excitation.). The pHe of the tumor, tumor rim and liver parenchyma were calculated from the H2, H3 and H6 chemical shifts as previously described (52).

Drug-eluting bead transarterial chemoembolization procedure

In group C, following adequate tumor growth confirmed by pre-procedural CT, DEB-TACE was performed according to previous procedural reports (43, 53). In summary, after careful surgical cut down of the right femoral artery access, a 3-French vascular sheath (Cook, Inc., Bloomington, IN, USA) was inserted followed by the introduction of a 2-French microcatheter (JB1 catheter; Cook, Inc., Bloomington, IN, USA) into the common hepatic artery. An arteriogram was then performed to identify the tumor as a region of hypervascular blush and to delineate the arterial road map to the left liver lobe. Subsequently, a 0.014" guidewire (Transend wire, Boston Scientific, USA) was selectively placed in the tumor-feeding hepatic artery. A microsphere suspension containing Oncozene® microspheres in either 40 μm or 100 μm diameter was prepared using 15 mg idarubicin per 3 ml microspheres, added to 7.5 mL contrast (Omnipaque 350, GE Healthcare) and 7.5 ml distilled sterile water, and aliquoted into a 0.5 ml syringe for delivery. The microsphere suspension was then slowly injected under real-time fluoroscopy monitoring to

prevent nontarget delivery. The endpoints of the embolization were complete administration of the microsphere suspension or premature stagnation of blood flow, as confirmed by intraprocedural fluoroscopy (54). Digital subtraction angiography, fluoroscopy imaging and cone-beam computer tomography (CT) were performed with a C-arm unit (Allura Clarity FD20, Philips Healthcare, Best, The Netherlands).

Blood laboratory analyses

In order to identify potential treatment-induced organ impairments, blood samples were collected pre-procedurally, and at 5 min, 24 h and 48 h after the completion of the microsphere suspension administration in the third, preclinical experimental treatment study. Laboratory analysis consisted of complete blood count, aspartate aminotransferase (AST), alanine aminotransferase (ALT), alkaline phosphatase, gamma-glutamyltranspeptidase, total bilirubin, albumin, and blood urea nitrogen. VEGF was quantified at the same time points using a Rabbit VEGF ELISA kit (MyBioSource, Inc., San Diego, CA, USA).

Histopathological staining

Immediately following MRI acquisition, animals across all study groups (A-C) were sacrificed under general anesthesia using pentobarbital sodium (300 mg/kg body weight). Tumor and liver samples were harvested and directly prepared for histopathological processing. In all study arms, one part of the explanted hepatic tumors was placed on optimal cutting temperature cassettes, and frozen at -80°C. In the diagnostic study arms, tumor and liver tissues were stored using embedding medium for cryostat sectioning (Tissue-Tek, Sakura Finetek, Torrance, CA, USA) sliced into 10 µm sections and mounted on adhesion slides (SuperFrost Plus, Thermo Scientific, Waltham, MA, USA). In the embolization treatment study (C), one part of the dissected tumor was directly placed in 10%-buffered formalin glass jars and stored at 4°C for subsequent paraffin embedment. For histopathological evaluation, all extracted tissues were cut into 2 - 10 µm slices, deparaffinized, rehydrated in a descending ethanol dilution series and eventually permeabilized in boiling retrieval solution for 40 minutes at 95°C. Across all study arms, samples were stained with hematoxylin and eosin (H&E). Tumor rims were quantified on H&E as an average of 5 measurements in different locations (55). The diagnostic T1-mapping based study (A) samples were additionally stained with Picrosirius red stain to visualize collagen content and tumor composition. The percentage of collagen fibers per region was determined through the ratio of the collagen content with the total area of the region. The diagnostic elastin-based study (B) samples were additionally stained with Miller's elastic van Gieson histochemical stain to visualize and quantify the ECM and

elastic fibers. In order to determine the percentage of elastin fibers per region, a corresponding color profile was automatically segmented and divided by the respective area (e.g., peritumoral region). In order to evaluate and correlate embolization-induced changes of the tumor and TME in treated animals of group C to imaging findings, liver and tumor samples were additionally stained with the proliferating cell nuclear antigen (PCNA) in order to visualize cell viability by staining proliferating cells, and terminal deoxynucleotidyl transferase dUTP nick end labeling (TUNEL) to display apoptotic cells (53). In order to reflect the hypoxic extent in untreated and embolized tissues, the hypoxia marker pimonidazole (Hypoxyprobe, NPI Inc., Burlington, USA) was intraperitoneally injected (50 mg/kg) in group C 2-4 hours before sacrifice as previously described (53). Tumor tissue samples were then stained with pimonidazole antibodies (Hypoxyprobe, NPI Inc., Burlington, USA) accordingly, and HIF-1α to compare the hypoxic degree.

Element specific bioimaging using laser ablation inductively coupled plasma mass spectrometry (LA-ICP-MS)

The LA-ICP-MS analysis for quantitative imaging of gadolinium, iron, zinc, and phosphor was post-mortem performed in study groups A and B as previously described (29). This technique reliably generates quantitative images of detailed regionally specific element distributions, and thereby conducts the capacity to compare the elastin tissue content to the gadolinium-bound elastin-specific probe deposition after contrast administration. For the ICP–MS analysis, samples were immediately embedded in 70% nitric acid at 37°C after image acquisition, and consecutively diluted with deionized water. A scan speed of 45 μm/s with unchanged 800 ml/min helium as transport gas was used in this analysis.

Fluorescence Imaging

Fluorescence imaging was performed in study group C in order to visualize and evaluate intra-tumoral idarubicin distribution after embolization treatment. Representative formalin-fixed tumor samples were washed in deionized water and sucrose, embedded in optimal cutting temperature compound and cryosectioned in 10-μm-thick slices at -20°C using Leica cryostat (Leica Biosystems Imaging, Inc., Buffalo Grove, IL, USA). After DAPI-PBS staining, fluorescent images using blue 405 nm and green 488 nm wave-length channels were produced and incorporated into segmented histogram heat maps based on a previously established heat map scale for idarubicin drug signal analysis (Center for Biological Innovation, Boston Scientific, MA, USA) and

performed using Metamorph microscopy automation and image analysis software (Molecular Devices, LLC., San Jose, CA, USA).

Statistical analysis

Results of the experiments including all quantitative parameters were summarized as mean ± standard deviation. Normality testing was performed individually for all parameters using the Shapiro-Wilk test and corresponding histograms for visualization. The Kruskal-Wallis test was performed to detect coherences of rabbit characteristics and the Mann-Whitney U test to ultimately compare the individual study groups. More specifically, two-way repeated-measures ANOVA was used to compare changes in T1 relaxation times between regions over time using Greenhouse–Geisser correction and Sidak's post hoc test. Additionally, univariate correlations were conducted using Pearson's correlation. Bonferroni corrected t-tests were applied to compare the differences between both, gadobutrol and ESMA contrast agents across all regions and time points. For data robustness, a mixed model was applied to account for the cross-sectional and longitudinal study design in the elastin-based diagnostic study arm (56). A two-tailed $P < 0.05$ was considered statistically significant. Statistical analysis was performed with R (R Project for Statistical Computing, Open Source, version 1.0.143/2017).

Essential new results

This research was originally published in:

1. *Borde T, Laage Gaupp F, Geschwind JF, Savic LJ, Miszczuk M, Rexha I, Adam L, Walsh JJ, Huber S, Duncan JS, Peters DC, Sinusas A, Schlachter T, Gebauer B, Hyder F, Coman D, van Breugel JMM, Chapiro J. Idarubicin-Loaded ONCOZENE Drug-Eluting Bead Chemoembolization in a Rabbit Liver Tumor Model: Investigating Safety, Therapeutic Efficacy, and Effects on Tumor Microenvironment. J Vasc Interv Radiol. 2020 Oct;31(10):1706-1716.e1.*

2. *Keller S, Borde T, Brangsch J, Reimann C, Kader A, Schulze D, Buchholz R, Kaufmann JO, Karst U, Schellenberger E, Hamm B, Makowski MR. Assessment of the hepatic tumor extracellular matrix using elastin-specific molecular magnetic resonance imaging in an experimental rabbit cancer model. Sci Rep. 2020 Nov 27;10(1):20785.*

3. *Keller S, Borde T, Brangsch J, Adams LC, Kader A, Reimann C, Gebert P, Hamm B, Makowski M. Native T1 Mapping Magnetic Resonance Imaging as a Quantitative Biomarker for Characterization of the Extracellular Matrix in a Rabbit Hepatic Cancer Model. Biomedicines. 2020 Oct 13;8(10):412.*

The following text describes the published results in detail.

Across all translational study arms, intrahepatic tumor growth was successfully induced in all animals with a mean tumor size of 11 ± 3 mm in the diagnostic study arms (A+B) and a mean pre-procedural tumor size of 16.5 ± 3 mm in the DEB-TACE treatment study group (C). There was no incidence of adverse events in untreated animals.

Quantification of molecular imaging parameters
Untreated intrahepatic tumors across both, diagnostic and therapeutic study populations, were identified by a hypointense signal output in unenhanced, native T1-weighted images.

Specific imaging findings diagnostic study groups A and B
Corresponding color-coded T1-maps equally identified the tumor region by a high signal accentuation compared to the relatively low, homogenous signal in the healthy liver parenchyma. More specifically, the highest native T1 relaxation times were measured in the tumor core (1721.7 $\pm$ 488.6 ms) followed by the tumor margin (1198.7 $\pm$ 291.3 ms), whereas the peritumoral surrounding (779.7 $\pm$ 212.1 ms) and healthy liver parenchyma (525.9 $\pm$ 185.5 ms) presented with considerably shorter T1 times. Post-hoc tests using Sidak`s correction demonstrated significant

differences in T1 relaxation times between all of the aforementioned regions (P < 0.001). No interaction effect was observed between longitudinal tumor growth and defined regions (F(2.86, 34.26) = 0.74, P = 0.53). Overall, time did not significantly affect tumor representation in native T1 mapping (F(2, 24) = 2.14, P = 0.14).

Following the administration of gadolinium contrast medium in the diagnostic, ESMA-specific as well as the embolic treatment study (A-C), the tumor adapted a linear enhancement around the marginal tumor rim in contrast-enhanced T1-weighted images (Figure 4). After the administration of the elastin-specific contrast agent in group B on the second consecutive imaging day, the tumor enhancement was visually potentiated (Figure 4). Regarding the RE of the elastin-specific probe, the high signal accentuation enabled an accurate distinction between all previously defined tumor regions (tumor core vs. tumor margin vs. peritumoral region, P < 0.001). On the contrary, the RE of gadobutrol could not as reliably distinguish between the tumor and peritumoral surrounding (difference 0.51; P = 0.07) but still accurately discriminated the tumor core and viable tumor rim (difference -0.59; P < 0.05). In detail, the post-hoc comparison analysis revealed significant differences between gadobutrol and elastin-specific contrast uptake in the tumor margin on day 14 (difference 1.86; P < 0.001), day 21 (difference 1.68; P = 0.007), and day 28 (difference 1.81; P < 0.001). Similar differences were observed in the peritumoral region on day 14 (difference 1.01; P = 0.03) and day 28 (difference 1.18; P = 0.005) as well as in the central regions on day 21 (difference 1.44; P = 0.034) and day 28 (difference 1.75; P < 0.001). Across all time points, the RE showed significantly higher values after ESMA injection than gadobutrol administration ($\chi^2(4)$ = 65.87, P < 0.001). No difference in the RE was measured in normal liver parenchyma and dorsal musculature at all time points (P = 1.00).

Specific imaging findings study group C

Imaging findings in the untreated control group in the embolization treatment arm (group C) were consistent with the aforementioned imaging results of a well delineated tumor margin on MRI using T1-mapping and the ESMA contrast agent. Similarly, perfusion- and permeability-based DCE-MRI revealed a hyperenhancement of the tumor rim while the tumor core remained hypovascular (Figure 4). Interestingly, post-embolization, the tumor rim and tumor core remained hypovascular in both embolic vectors (mean arterial enhancement [%] 40 µm 2 ± 3, 100 µm 9 ± 3, control 36 ± 51, P = 0.07). Altogether, embolized tumors revealed considerably less contrast uptake in arterial and late portal venous phase compared with liver parenchyma (liver 81 ± 25, P < 0.001). In untreated animals, DWI revealed the lowest ADC signal intensity in the tumor rim (mean ADC $(1.55 ± 0.09)$ x10^{-3} mm^2/s), without any difference to liver parenchyma (1.62 ± 0.23,

P = 0.65). The corresponding tumor cores presented high ADC values (2.34 ± 0.18, P = 0.001, Figure 4). Following DEB-TACE, tumor rims could not be distinguished anymore in DWI and compared to baseline tumors, embolized tumors showed significantly higher ADC values (40 μm 1.91 ± 0.15, 100 μm 1.85 ± 0.27, control 2.34 ± 0.18, P < 0.001).

In the untreated control animals of the embolization treatment arm (C), BIRDS revealed significantly lower pHe values in the tumor compared to the healthy liver parenchyma (mean tumor pHe 6.79 ± 0.08, liver 7.13 ± 0.08, P = 0.02, Figure 4). The tumor rim, defined as the region of voxels partly (> 50%) outside the tumor defined area, showed a tendency towards lower acidity than tumor cores (7.03 ± 0.14 vs. 6.79 ± 0.08, P = 0.07). Similar results were measured in embolized tumors (40 μm tumor / liver pHe 6.75 ± 0.05 / 7.05 ± 0.07, 100 μm 6.9 ± 0.1 / 7.1 ± 0.03, P = 0.003), with no considerable difference between both embolization treatment groups. Healthy liver parenchyma had consistent pHe values across all imaged animals (P = 0.4).

Chemoembolization procedure and laboratory analysis in study group C

DEB-TACE was technically successful in all embolized animals (N = 9) in study group C with localized contrast deposition within all treated tumors. The mean total volume of delivered microsphere suspension was slightly higher in 40 μm as compared to 100 μm microspheres (mean total volume [ml] 0.49 vs. 0.41, P = 0.04). Complications in suspension delivery occurred in 100 μm microspheres most likely due to increasing viscosity and consecutive clumping within the microcatheter towards the end of the procedure (N = 2). Further adverse events included femoral artery hemorrhage (N = 1) and cardiac arrest under anesthesia during MRI (N = 1). Apart from these intra-procedural adverse events, there was no apparent drug-induced toxicity observed in the animals by daily clinical assessment. Moreover, laboratory analysis revealed no hematologic or renal impairments. Interestingly, in animals treated with 40 μm DEBs, an 18-fold increase in ALT serum levels and a 25-fold increase in AST was observed within the first 24 h post-procedurally compared to baseline (ALT 430.2 ± 165 vs. 23.6 ± 8.1, P < 0.001 and AST 434.2 ± 334 vs. 17.4 ± 5.9, P = 0.02). No further increase was observed after 24 h. On the contrary, 100 μm DEBs merely led to a slight increase in ALT (18 ± 5 vs. 86 ± 50, P = 0.07) but no change in AST (29 ± 14 vs. 93 ± 64, P = 0.16). The additionally obtained laboratory liver parameters remained unaffected. In both microsphere groups, the tumor area was macroscopically distinguished as an area of hepatic necrosis. However, 40 μm DEBs also caused visible parenchymal necrosis in ipsilateral liver segments that were not immediately adjacent to the tumor segment, indicating a non-target penetration of 40 μm microspheres into healthy liver tissue. No extra-hepatic deposition of the embolics was observed. VEGF, as an indicator of neo-angiogenesis, showed no differences in

plasma levels across the untreated and embolized treatment groups (P = 0.10). There was also no difference in VEGF expression levels after tumor embolization in both treatment groups (40 μm 0.25 ± 0.1, 100 μm 0.28 ± 0.03 ng/ml, P = 0.16).

Ex-vivo histopathological analysis

MpMRI findings were reproduced and validated by ex-vivo histopathological analysis. Concurrent across all study arms (A-C), untreated tumors revealed areas of scattered tumor core necrosis with dispersed viable tumor cell islands in the tumor center in H&E staining. A viable tumor rim (0.3 ± 0.5 mm across all analyzed study groups) was found to surround the tumor core with densely packed tumor cells and additionally high expression levels of the proliferation marker PCNA. Hypoxic areas and tumor cells undergoing cell apoptosis were strictly confined to the tumor core across all study groups.

Specific histopathological findings study group A

In order to correlate the signal intensity in native T1 maps with its histopathological counterpart, the collagen content was histologically quantified in all defined tumor regions in group A. Concurrent with the imaging results of native T1 mapping, the collagen expression was significantly different between the tumor and extra-tumoral tissue across all time points (P < 0.001). The highest relative proportions of collagen fibers were measured in the tumor core and tumor rim ([%] 22.8 ± 9.8, 31.8 ± 6.5, respectively). Extra-tumoral regions expressed less collagen content than the intra-tumoral areas (peritumoral region 9.2 ± 2.5, healthy liver parenchyma 0.23 ± 0.18). Imaging-based quantified T1 relaxation times, altogether, highly correlated with the histopathologically determined collagen stain area (r = 0.64, P < 0.001). In detail, the T1 relaxation times of the tumor rim showed the highest correlation coefficient (r = 0.84, P < 0.001), followed by the central (r = 0.78, P < 0.001), and peritumoral (r = 0.73, P < 0.001) defined regions.

Specific histopathological and LA-ICP-MS results study group B

With regard to the increased intra- and peri-tumoral enhancement following the administration of the elastin-specific contrast agent in group B, the corresponding Miller's elastic van Gieson staining revealed a high correlation between the in vivo imaging findings and the ex-vivo measurement of elastin fibers (r = 0.84, P < 0.001). In addition, in order to reliably quantify the amount of the gadolinium-bound elastin-specific probe, LA-ICP-MS testing was conducted and revealed a high correlation of the mass-spectrometry-based gadolinium concentration, histopathologically stained elastin areas (r = 0.59; P < 0.05) and the elastin-specific MR-based RE

(r = 0.73; P < 0.01). The simultaneous presence of the gadolinium-bound elastin-specific probe and elastic fibers was predominantly detected in the tumor rim and the peritumoral region. The spatial distribution of phosphor, zinc, iron and gadolinium in the samples showed no distinctive distribution within the samples.

Specific histopathological and fluorescence imaging results study group C
In embolized tumors (group C) on H&E staining, no viable tumor cells were identified. The tumor region merely presented sporadic cell outlines without nuclei highly suggestive of coagulative necrosis which was validated by high expression levels of TUNEL and the disappearance of PCNA expression. In 40 µm embolics, the TUNEL staining, representative of cell death, was not only confined to the tumor region but extended up to 25 % of the tumor diameter into the adjacent liver parenchyma. Correspondingly, the hypoxia markers HIF-1α and pimonidazole were most pronounced in these perishing tumor regions but were also observed to exceed the tumor margins in a radius of up to 50% of the tumor diameter in 40 µm and up to 10 % in 100µm microspheres. In order to evaluate the distribution of idarubicin-loaded embolics, fluorescence imaging was performed and revealed that there was a greater quantity of intra-tumoral blood vessels containing 40 µm embolics compared to 100 µm microspheres (26.3 ± 9.1, 3.5 ± 2.1 blood vessels per tumor, P = 0.04). 40 µm DEBs were observed to fully invade the tumor center, whereas 100 µm embolics were primarily identified within the tumor rim. Fluorescence imaging demonstrated that idarubicin was still mainly loaded onto the spheres and merely eluted within a 100 µm radius from embolized vessels with both microsphere sizes.

Resulting clinical applications and further scientific questions

The presented diagnostic and therapeutic study arms investigated the applicability, practicality and efficacy of various non-invasive MRI sequences in the course of liver carcinogenesis to improve early detectability and evaluate therapy responsiveness. Overall, the main findings of these studies were that native T1 mapping, elastin-specific MRI, perfusion- and diffusion-weighted MRI as well as the pHe-sensitive BIRDS sequence serve as reliable, quantitative biomarkers to assess tumor microenvironmental changes and potentially tumor response to treatment. Furthermore, Oncozene® microspheres in 40 µm and 100 µm diameter both induce anti-tumoral effects, including rapid devascularization and consecutive tumor necrosis with unaffected high acidity levels that can be visualized with the help of multiparametric MRI.

The longitudinal T1 relaxation time is an intrinsic reflection of the structural composition of various tissues and is particularly influenced by the ECM disposition and water volume fraction. In the clinical setting, native T1 mapping has been initially applied in cardiovascular imaging as an auxiliary imaging biomarker for the assessment and discrimination of primary myocardial diseases which ultimately led to the incorporation of native T1 mapping into the official cardiovascular guidelines (33, 34, 57). Hepatocyte specific contrast supported T1 mapping has already been successfully applied to identify and differentiate various intrahepatic lesions, including HCC (58). Nonetheless, native T1 mapping has become of emerging interest, not alone due to its independency of contrast medium and therefore improved renal protection profile. The differentiation and estimation of liver fibrosis was shown to have a superior diagnostic accuracy in native T1 mapping compared to ultrasound elastography (59). However, there have been limited attempts to further apply native T1 mapping to detect and characterize liver tumors and their TME. In this study, an inversion-recovery sequence based on a MOLLI pulse sequence was adopted to enable a clinical practicable quantification of T1 tissue relaxation times in a single breath hold and with steady-state free precession readouts. Although saturation recovery sequences such as the saturation recovery single-shot acquisition (SASHA) overcome the confounding effects of magnetization transfer and T2 influence in MOLLI sequences, SASHA demonstrates a higher variability and heterogeneity of T1 values with a resulting inability to detect small T1 variances (60). In this study, the longest T1 values were measured inside the tumor with gradually decreasing relaxation times towards the periphery and extra-tumoral tissue. Prolonged native T1 values are based on an increase in interstitial space, predominantly related to an excess of water or an overexpression of collagen. High native T1 values are also influenced by steatosis and iron accumulation (61). The T1 gradient observed in this study aligns with the corresponding

histopathological findings of central tumor necrosis and a divergent structural composition of the tumor rim. As demonstrated in myocardial infarction, coagulative necrosis leads to an increase in diffusion which ultimately causes consecutive interstitial edema (31). The high native T1 relaxation times in the tumor margin rather indicate a more densely packed cellular rim with an increased capillary perfusion and an inflated synthesis of extracellular tissue (58, 62).

Collagen and elastin, as the most abundant ECM proteins, were shown to be profoundly dysregulated in tumoral tissue as a result of tumor hypoxia effects on the TME and contribute to an increased extracellular stiffness (24, 63). This study illustrates that higher extracellular collagen content leads to prolonged native T1 relaxation times that can be distinguished from healthy parenchyma in native T1-weighted MRI (34, 62). Similar to the pathologically altered collagen expression, HIF-1α-catalyzed accumulation of dysfunctional, fragmented elastin fibers was observed in HCC (64). While Maehara et al. found no direct association between radiographical, contrast-enhanced CT and histologically validated elastic fiber accumulation, the results of this study suggest an improvement in the detectability of a pathologic ECM configuration with the help of an elastin-specific molecular MR probe. Previously, ESMA has been successfully applied in cardiovascular and renal imaging to specifically characterize the atherosclerotic plaque burden, changes in the aortic wall, and ECM alterations in renal fibrosis (29, 30, 65). However, no attempt has been made until now to visualize and quantify tumor microenvironmental changes in the course of liver carcinogenesis. The dysregulation of Type I collagen as the major constituent of the ECM has already been associated with tumor growth and poor prognosis (66, 67). During the progression of liver fibrosis and cirrhosis, the elastin-to-collagen ratio gradually increases. Although elastin expression is upregulated from the onset of injury, an accumulation of elastin fibers is predominantly observed later as the disease progresses, as opposed to collagen content (68, 69). Since HCC predominantly develops within cirrhotic liver parenchyma, the quantification of elastin may serve as a potential imaging indicator of early HCC disease progression and risk assessment of HCC development. The elastin-specific MRI enhancement seen in viable tumor tissue highly correlated with increased elastic fiber depositions. Due to the secondary function of elastin as an essential element in the structural composition of blood vessels (27), an increased elastin content may, therefore, also be directly relatable to an increased capillary network and therefore be indirectly suggestive of the hypervascularity of the tumor. The results of DCE-MRI confirmed this hypothesis by showing that with an hyperenhancement of the tumor rim in untreated controls correlated with increased vascular perfusion. These findings are also congruent with DWI in which the lowest ADC signal intensity was measured in the tumor rim. Since the DWI-derived

ADC value is also affected by the underlying tissue vascularity (70), the obtained ADC values may reflect the dense cellularity and increased capillary network of the viable tumor rims.

Furthermore, the MR spectroscopy-based quantification of the pHe using the novel imaging sequence BIRDS detected a pronounced acidosis within the tumor regions compared to physiological values in healthy liver parenchyma. This phenomenon may derive from an exorbitantly exacerbated, aerobic glucose consumption of the tumor, described by the Warburg effect, and a consecutive by-product accumulation of lactate and protons that gradually acidify the TME. Tumor hypoxia and acidosis may be seen as natural selectors for apoptosis-resistant tumor cells (71). A consequence of this hypoxic selection may be, in part, the oxygen-independent hyperglycolysis which stabilizes HIF-1α inside the tumor and therefore sustains tumor growth and tumor viability (72). Another factor contributing to the tumor resistance mechanism is the acidification of the TME. The effect of a diminished microenvironmental pH not only has a deleterious local impact but also affects the responsiveness of infiltrating immune cells. An increasing accumulation of acidic lactate and protons was demonstrated to decrease signaling cytokine production, and impair activation and proliferation of tumor-associated T cells (73). Therefore, the acidification of the TME most likely represents a "niche engineering strategy" to promote tumor progression and immune evasion (38-40, 74). Given this profound effect on the local cell integrity and immune response, the non-invasive quantification of the pHe addresses an unmet clinical need for the identification and characterization of metabolic abnormalities in tumors. Especially in the context of precision therapy, knowledge about the specific configuration of tumors and their TME are useful for personalized oncologic therapy regimes. Therefore, BIRDS is a promising, non-invasive and radiation-free approach that reliably monitors the tissue pHe. This molecular imaging method is less sensitive to magnetic field inhomogeneities and is also favorable for its independency of tissue perfusion, contrast agent concentrations and temperature variations (75). Chemical exchange saturation transfer (CEST) is an existing, clinically available MR-based technique for the measurement of the pHe. CEST relies on the mitigation of the bulk water signal due to the chemical transfer of selectively saturated, exchangeable, solute protons such as proteins, amino acids, or sugars (76). Although CEST provides a slightly higher resolution than BIRDS, it lacks sensitivity and standardization because it requires a large number of exchangeable groups and largely varies dependent on radiofrequency power and magnetic field strength (72, 76).

The therapeutic study arm (group C) was initiated to assess the MRI capability to detect and monitor treatment related effects on the tumor and tumor microenvironment in terms of tumor perfusion, diffusion and tumor pHe following chemoembolization with two different microsphere sizes. The induced chemo-embolic effects measured in this experimental treatment arm comply

with previous studies demonstrating that smaller calibrated microspheres advance farther into peripheral vasculature leading to a broader extent of tissue ischemia and toxicity inside the tumor but also in surrounding healthy liver parenchyma (77-80). 40 µm DEBs induced larger extents of hypoxia without a detectable increase in VEGF plasma concentration, indicating that they do not aggravate neo-angiogenesis. This finding should be treated with caution due the naturally existent hypervascularity of VX2 tumors and the prolonged process of VEGF gene transcription until a detectable increase in VEGF concentration is reached (19). Although the investigated 40 µm and 100 µm particles showed differences in depth of vessel penetration and consecutive chemotherapeutic agent coverage, both particle types equally caused coagulative tumor necrosis indicating that the main anti-tumoral, short-term mechanism of action was ischemia due to devascularization rather than chemotherapeutic effects.

Multiparametric MRI proved highly beneficial in the identification and characterization of various tumor regions and alterations in the TME. Following chemoembolization treatment, DCE-MRI demonstrated an acute reduction in tumor vascularity and decreased blood perfusion of the hypervascular VX2 tumors, confirming the sensitivity of this imaging method (81). Furthermore, in DWI, the tumor rim was undistinguishable from the tumor core suggesting an immediate post-embolic reduction of cellularity and complete necrosis. Since the DWI-derived ADC value is also influenced by capillary perfusion, this finding further confirms the anti-tumoral effects induced by devascularization. No immediate post-embolic change in tumor pHe was measured. This might be explained by the abrupt onset of vascular occlusion following DEB-TACE with a subsequent exacerbation of hypoxia which may intensify hyperglycolysis and the subsequent acidification of the TME early after TACE (82). In a longitudinal monitoring study of post-TACE effects on the TME, molecular pHe mapping proved to be sensitive to small changes in local tumor pHe and demonstrated a gradual normalization of the tumor pHe following conventional TACE treatment (83). Therefore, while devascularization and tumor necrosis initiation upon locoregional treatment are visible on MRI almost immediately post-procedurally, the normalization of the tumor pHe is a gradual accomplishment with a time frame of over 7 days (83). These findings suggest a high sensitivity of BIRDS to serve as a reliable, quantitative biomarker to longitudinally monitor therapeutic effects on the tumor and TME.

These studies examined the TME in VX2 tumors of non-hepatic origin without an underlying liver cirrhosis as VX2 tumors present the most common liver tumor model due to their similarity to HCC in their hypervascular and hyperglycolytic nature (84). However, their rapid and metastatic tumor growth often lead to an inherent tumor core necrosis at baseline which may have affected therapeutic effects of DEB-TACE. Nonetheless, central tumor core necrosis is also frequently

observed in human-derived HCC and therefore, may have contributed to a reliable assessment of the HCC tumor phenotype in MRI. The VX2 rabbit liver tumor model is also favorable in its suitability for TACE therapy with clinically standardized equipment and its applicability on clinical 3T MRI scanners. However, the assessment of the toxicity profile of idarubicin-eluting Oncozene® microspheres was limited by both the small sample size and the relatively short-termed acquisition of terminal imaging. Therefore, longitudinal studies with pre- as well as multiple post-procedural imaging reference points would provide a more distinctive and reliable assessment of the long-term anti-tumoral efficacy, tolerability and effects on the TME composition accompanying tumor growth and following therapeutic interventions.

In conclusion, multiparametric MRI identified quantitative, non-invasive imaging biomarkers to reliably detect and characterize variances in the tumor and tumor microenvironmental phenotype as well as therapy-related changes following DEB-TACE. Native T1 mapping based on the MOLLI technique accurately defined tumor regions with regard to their viability and highly correlated with an aberrant, tumor-associated ECM expression. The implementation of novel, elastin-specific and pHe-sensitive molecular contrast agents resulted in an improved, distinctive characterization of the tumor microenvironment and may be used to detect and characterize HCC in earlier stages. Therefore, these additional imaging techniques may add to the toolbox of radiologists when assessing liver tumors in clinical practice. The comprehensive MRI biomarker panel may present a non-invasive alternative to biopsies and may help to assess the susceptibility to treatment and the response to treatment in a longitudinal fashion. Additional longitudinal and human-subjected studies are warranted to establish these promising imaging instruments as reliable early markers for HCC and treatment-induced effects on the tumor microenvironment.

References

1.	Bray F, Ferlay J, Soerjomataram I, Siegel RL, Torre LA, Jemal A. Global cancer statistics 2018: GLOBOCAN estimates of incidence and mortality worldwide for 36 cancers in 185 countries. CA Cancer J Clin. 2018;68(6):394-424.

2.	Colli A, Fraquelli M, Casazza G, Massironi S, Colucci A, Conte D, Duca P. Accuracy of ultrasonography, spiral CT, magnetic resonance, and alpha-fetoprotein in diagnosing hepatocellular carcinoma: a systematic review. Am J Gastroenterol. 2006;101(3):513-23.

3.	Llovet JM, Fuster J, Bruix J, Barcelona-Clinic Liver Cancer G. The Barcelona approach: diagnosis, staging, and treatment of hepatocellular carcinoma. Liver Transpl. 2004;10(2 Suppl 1):S115-20.

4.	Bruix J, Llovet JM. Prognostic prediction and treatment strategy in hepatocellular carcinoma. Hepatology. 2002;35(3):519-24.

5.	Golabi P, Fazel S, Otgonsuren M, Sayiner M, Locklear CT, Younossi ZM. Mortality assessment of patients with hepatocellular carcinoma according to underlying disease and treatment modalities. Medicine (Baltimore). 2017;96(9):e5904.

6.	El-Serag HB. Hepatocellular carcinoma. N Engl J Med. 2011;365(12):1118-27.

7.	Tsurusaki M, Murakami T. Surgical and Locoregional Therapy of HCC: TACE. Liver Cancer. 2015;4(3):165-75.

8.	Lencioni R, de Baere T, Soulen MC, Rilling WS, Geschwind JF. Lipiodol transarterial chemoembolization for hepatocellular carcinoma: A systematic review of efficacy and safety data. Hepatology. 2016;64(1):106-16.

9.	Chen P, Yuan P, Chen B, Sun J, Shen H, Qian Y. Evaluation of drug-eluting beads versus conventional transcatheter arterial chemoembolization in patients with unresectable hepatocellular carcinoma: A systematic review and meta-analysis. Clin Res Hepatol Gastroenterol. 2017;41(1):75-85.

10.	Hanahan D, Weinberg RA. Hallmarks of cancer: the next generation. Cell. 2011;144(5):646-74.

11.	Denko NC. Hypoxia, HIF1 and glucose metabolism in the solid tumour. Nat Rev Cancer. 2008;8(9):705-13.

12.	Challapalli A, Carroll L, Aboagye EO. Molecular mechanisms of hypoxia in cancer. Clin Transl Imaging. 2017;5(3):225-53.

13.	Fong GH. Mechanisms of adaptive angiogenesis to tissue hypoxia. Angiogenesis. 2008;11(2):121-40.

14.	Ling YH, Chen JW, Wen SH, Huang CY, Li P, Lu LH, Mei J, Li SH, Wei W, Cai MY, Guo RP. Tumor necrosis as a poor prognostic predictor on postoperative survival of patients with solitary small hepatocellular carcinoma. BMC Cancer. 2020;20(1):607.

15.	Koh DM, Collins DJ. Diffusion-weighted MRI in the body: applications and challenges in oncology. AJR Am J Roentgenol. 2007;188(6):1622-35.

16.	Wu XZ, Xie GR, Chen D. Hypoxia and hepatocellular carcinoma: The therapeutic target for hepatocellular carcinoma. J Gastroenterol Hepatol. 2007;22(8):1178-82.

17.	Muz B, de la Puente P, Azab F, Azab AK. The role of hypoxia in cancer progression, angiogenesis, metastasis, and resistance to therapy. Hypoxia (Auckl). 2015;3:83-92.

18.	Petrillo M, Patella F, Pesapane F, Suter MB, Ierardi AM, Angileri SA, Floridi C, de Filippo M, Carrafiello G. Hypoxia and tumor angiogenesis in the era of hepatocellular carcinoma transarterial loco-regional treatments. Future Oncol. 2018;14(28):2957-67.

19.	von Marschall Z, Cramer T, Hocker M, Finkenzeller G, Wiedenmann B, Rosewicz S. Dual mechanism of vascular endothelial growth factor upregulation by hypoxia in human hepatocellular carcinoma. Gut. 2001;48(1):87-96.

20.	Kim KR, Moon HE, Kim KW. Hypoxia-induced angiogenesis in human hepatocellular carcinoma. J Mol Med (Berl). 2002;80(11):703-14.

21.	Yankeelov TE, Gore JC. Dynamic Contrast Enhanced Magnetic Resonance Imaging in Oncology: Theory, Data Acquisition, Analysis, and Examples. Curr Med Imaging Rev. 2009;3(2):91-107.

22.	Barnes SL, Whisenant JG, Loveless ME, Yankeelov TE. Practical dynamic contrast enhanced MRI in small animal models of cancer: data acquisition, data analysis, and interpretation. Pharmaceutics. 2012;4(3):442-78.

23.	Wang M, Zhao X, Zhu D, Liu T, Liang X, Liu F, Zhang Y, Dong X, Sun B. HIF-1alpha promoted vasculogenic mimicry formation in hepatocellular carcinoma through LOXL2 up-regulation in hypoxic tumor microenvironment. J Exp Clin Cancer Res. 2017;36(1):60.

24.	Carloni V, Luong TV, Rombouts K. Hepatic stellate cells and extracellular matrix in hepatocellular carcinoma: more complicated than ever. Liver Int. 2014;34(6):834-43.

25.	Schrader J, Gordon-Walker TT, Aucott RL, van Deemter M, Quaas A, Walsh S, Benten D, Forbes SJ, Wells RG, Iredale JP. Matrix stiffness modulates proliferation, chemotherapeutic response, and dormancy in hepatocellular carcinoma cells. Hepatology. 2011;53(4):1192-205.

26.	Yasui Y, Abe T, Kurosaki M, Higuchi M, Komiyama Y, Yoshida T, Hayashi T, Kuwabara K, Takaura K, Nakakuki N, Takada H, Tamaki N, Suzuki S, Nakanishi H, Tsuchiya K, Itakura J, Takahashi Y, Hashiguchi A, Sakamoto M, Izumi N. Elastin Fiber Accumulation in Liver Correlates with the Development of Hepatocellular Carcinoma. PLoS One. 2016;11(4):e0154558.

27.	Kendall TJ, Dolman GE, Duff CM, Paish EC, Zaitoun A, Irving W, Fallowfield JA, Guha IN. Hepatic elastin content is predictive of adverse outcome in advanced fibrotic liver disease. Histopathology. 2018;73(1):90-100.

28.	Botnar RM, Wiethoff AJ, Ebersberger U, Lacerda S, Blume U, Warley A, Jansen CH, Onthank DC, Cesati RR, Razavi R, Marber MS, Hamm B, Schaeffter T, Robinson SP, Makowski MR. In vivo assessment of aortic aneurysm wall integrity using elastin-specific molecular magnetic resonance imaging. Circ Cardiovasc Imaging. 2014;7(4):679-89.

29.	Brangsch J, Reimann C, Kaufmann JO, Adams LC, Onthank DC, Thone-Reineke C, Robinson SP, Buchholz R, Karst U, Botnar RM, Hamm B, Makowski MR. Concurrent Molecular Magnetic Resonance Imaging of Inflammatory Activity and Extracellular Matrix Degradation for the Prediction of Aneurysm Rupture. Circ Cardiovasc Imaging. 2019;12(3):e008707.

30.	Makowski MR, Wiethoff AJ, Blume U, Cuello F, Warley A, Jansen CH, Nagel E, Razavi R, Onthank DC, Cesati RR, Marber MS, Schaeffter T, Smith A, Robinson SP, Botnar RM. Assessment of atherosclerotic plaque burden with an elastin-specific magnetic resonance contrast agent. Nat Med. 2011;17(3):383-8.

31.	Germain P, El Ghannudi S, Jeung M-Y, Ohlmann P, Epailly E, Roy C, Gangi A. Native T1 mapping of the heart - a pictorial review. Clin Med Insights Cardiol. 2014;8(Suppl 4):1-11.

32.	Ugander M, Bagi PS, Oki AJ, Chen B, Hsu LY, Aletras AH, Shah S, Greiser A, Kellman P, Arai AE. Myocardial edema as detected by pre-contrast T1 and T2 CMR delineates area at risk associated with acute myocardial infarction. JACC Cardiovasc Imaging. 2012;5(6):596-603.

33.	Bull S, White SK, Piechnik SK, Flett AS, Ferreira VM, Loudon M, Francis JM, Karamitsos TD, Prendergast BD, Robson MD, Neubauer S, Moon JC, Myerson SG. Human non-contrast T1 values and correlation with histology in diffuse fibrosis. Heart. 2013;99(13):932-7.

34.	Nakamori S, Dohi K, Ishida M, Goto Y, Imanaka-Yoshida K, Omori T, Goto I, Kumagai N, Fujimoto N, Ichikawa Y, Kitagawa K, Yamada N, Sakuma H, Ito M. Native T1 Mapping and Extracellular Volume Mapping for the Assessment of Diffuse Myocardial Fibrosis in Dilated Cardiomyopathy. JACC Cardiovasc Imaging. 2018;11(1):48-59.

35.	Li Z, Sun J, Hu X, Huang N, Han G, Chen L, Zhou Y, Bai W, Yang X. Assessment of liver fibrosis by variable flip angle T1 mapping at 3.0T. J Magn Reson Imaging. 2016;43(3):698-703.

36.	Adams LC, Ralla B, Jurmeister P, Bressem KK, Fahlenkamp UL, Hamm B, Busch J, Makowski MR. Native T1 Mapping as an In Vivo Biomarker for the Identification of Higher-Grade Renal Cell Carcinoma: Correlation With Histopathological Findings. Invest Radiol. 2019;54(2):118-28.

37.	Sun J, Li J, Guo Z, Sun L, Juan C, Zhou Y, Gu H, Yu Y, Hu Q, Kan Q, Yu Z. Overexpression of Pyruvate Dehydrogenase E1alpha Subunit Inhibits Warburg Effect and Induces Cell Apoptosis Through Mitochondria-Mediated Pathway in Hepatocellular Carcinoma. Oncol Res. 2019;27(4):407-14.

38.	Goetze K, Walenta S, Ksiazkiewicz M, Kunz-Schughart LA, Mueller-Klieser W. Lactate enhances motility of tumor cells and inhibits monocyte migration and cytokine release. Int J Oncol. 2011;39(2):453-63.

39.	Rofstad EK, Mathiesen B, Kindem K, Galappathi K. Acidic extracellular pH promotes experimental metastasis of human melanoma cells in athymic nude mice. Cancer Res. 2006;66(13):6699-707.

40.   Estrella V, Chen T, Lloyd M, Wojtkowiak J, Cornnell HH, Ibrahim-Hashim A, Bailey K, Balagurunathan Y, Rothberg JM, Sloane BF, Johnson J, Gatenby RA, Gillies RJ. Acidity generated by the tumor microenvironment drives local invasion. Cancer Res. 2013;73(5):1524-35.

41.   Anemone A, Consolino L, Arena F, Capozza M, Longo DL. Imaging tumor acidosis: a survey of the available techniques for mapping in vivo tumor pH. Cancer Metastasis Rev. 2019;38(1-2):25-49.

42.   Percie du Sert N, Hurst V, Ahluwalia A, Alam S, Avey MT, Baker M, Browne WJ, Clark A, Cuthill IC, Dirnagl U, Emerson M, Garner P, Holgate ST, Howells DW, Karp NA, Lazic SE, Lidster K, MacCallum CJ, Macleod M, Pearl EJ, Petersen OH, Rawle F, Reynolds P, Rooney K, Sena ES, Silberberg SD, Steckler T, Wurbel H. The ARRIVE guidelines 2.0: Updated guidelines for reporting animal research. PLoS Biol. 2020;18(7):e3000410.

43.   Hong K, Khwaja A, Liapi E, Torbenson MS, Georgiades CS, Geschwind JF. New intra-arterial drug delivery system for the treatment of liver cancer: preclinical assessment in a rabbit model of liver cancer. Clin Cancer Res. 2006;12(8):2563-7.

44.   Moreira PL, An YH. Animal models for therapeutic embolization. Cardiovasc Intervent Radiol. 2003;26(2):100-10.

45.   Geschwind JF, Artemov D, Abraham S, Omdal D, Huncharek MS, McGee C, Arepally A, Lambert D, Venbrux AC, Lund GB. Chemoembolization of liver tumor in a rabbit model: assessment of tumor cell death with diffusion-weighted MR imaging and histologic analysis. J Vasc Interv Radiol. 2000;11(10):1245-55.

46.   Elsayes KM, Narra VR, Yin Y, Mukundan G, Lammle M, Brown JJ. Focal hepatic lesions: diagnostic value of enhancement pattern approach with contrast-enhanced 3D gradient-echo MR imaging. Radiographics. 2005;25(5):1299-320.

47.   Rofsky NM, Lee VS, Laub G, Pollack MA, Krinsky GA, Thomasson D, Ambrosino MM, Weinreb JC. Abdominal MR imaging with a volumetric interpolated breath-hold examination. Radiology. 1999;212(3):876-84.

48.   Hyder F. Dynamic imaging of brain function. Methods Mol Biol. 2009;489:3-21.

49.   Michaely HJ, Morelli JN, Budjan J, Riffel P, Nickel D, Kroeker R, Schoenberg SO, Attenberger UI. CAIPIRINHA-Dixon-TWIST (CDT)-volume-interpolated breath-hold examination (VIBE): a new technique for fast time-resolved dynamic 3-dimensional imaging of the abdomen with high spatial resolution. Invest Radiol. 2013;48(8):590-7.

50.   Coman D, Peters DC, Walsh JJ, Savic LJ, Huber S, Sinusas AJ, Lin M, Chapiro J, Constable RT, Rothman DL, Duncan JS, Hyder F. Extracellular pH mapping of liver cancer on a clinical 3T MRI scanner. Magn Reson Med. 2020;83(5):1553-64.

51.   Coman D, Trubel HK, Rycyna RE, Hyder F. Brain temperature and pH measured by (1)H chemical shift imaging of a thulium agent. NMR Biomed. 2009;22(2):229-39.

52.   Coman D, Trubel HK, Hyder F. Brain temperature by Biosensor Imaging of Redundant Deviation in Shifts (BIRDS): comparison between TmDOTP5- and TmDOTMA. NMR Biomed. 2010;23(3):277-85.

53.   Duran R, Mirpour S, Pekurovsky V, Ganapathy-Kanniappan S, Brayton CF, Cornish TC, Gorodetski B, Reyes J, Chapiro J, Schernthaner RE, Frangakis C, Lin M, Sun JD, Hart CP, Geschwind JF. Preclinical Benefit of Hypoxia-Activated Intra-arterial Therapy with Evofosfamide in Liver Cancer. Clin Cancer Res. 2017;23(2):536-48.

54.   Savic LJ, Schobert IT, Peters D, Walsh JJ, Laage-Gaupp FM, Hamm CA, Tritz N, Doemel LA, Lin M, Sinusas A, Schlachter T, Duncan JS, Hyder F, Coman D, Chapiro J. Molecular Imaging of Extracellular Tumor pH to Reveal Effects of Locoregional Therapy on Liver Cancer Microenvironment. Clin Cancer Res. 2020;26(2):428-38.

55.   Ahmed M, Kumar G, Gourevitch S, Levchenko T, Galun E, Torchilin V, Goldberg SN. Radiofrequency ablation (RFA)-induced systemic tumor growth can be reduced by suppression of resultant heat shock proteins. Int J Hyperthermia. 2018;34(7):934-42.

56.   Kuznetsova A, Brockhoff PB, Christensen RHB. lmerTest Package: Tests in Linear Mixed Effects Models. 2017. 2017;82(13):26.

57.   Puntmann VO, Peker E, Chandrashekhar Y, Nagel E. T1 Mapping in Characterizing Myocardial Disease: A Comprehensive Review. Circ Res. 2016;119(2):277-99.

58.   Peng Z, Li C, Chan T, Cai H, Luo Y, Dong Z, Li ZP, Feng ST. Quantitative evaluation of Gd-EOB-DTPA uptake in focal liver lesions by using T1 mapping: differences between hepatocellular carcinoma, hepatic focal nodular hyperplasia and cavernous hemangioma. Oncotarget. 2017;8(39):65435-44.

59.   Li J, Liu H, Zhang C, Yang S, Wang Y, Chen W, Li X, Wang D. Native T1 mapping compared to ultrasound elastography for staging and monitoring liver fibrosis: an animal study of repeatability, reproducibility, and accuracy. Eur Radiol. 2020;30(1):337-45.

60.   Teixeira T, Hafyane T, Stikov N, Akdeniz C, Greiser A, Friedrich MG. Comparison of different cardiovascular magnetic resonance sequences for native myocardial T1 mapping at 3T. J Cardiovasc Magn Reson. 2016;18(1):65.

61.   Haaf P, Garg P, Messroghli DR, Broadbent DA, Greenwood JP, Plein S. Cardiac T1 Mapping and Extracellular Volume (ECV) in clinical practice: a comprehensive review. J Cardiovasc Magn Reson. 2016;18(1):89.

62.   Robbers LF, Baars EN, Brouwer WP, Beek AM, Hofman MB, Niessen HW, van Rossum AC, Marcu CB. T1 mapping shows increased extracellular matrix size in the myocardium due to amyloid depositions. Circ Cardiovasc Imaging. 2012;5(3):423-6.

63.   Nissen NI, Karsdal M, Willumsen N. Collagens and Cancer associated fibroblasts in the reactive stroma and its relation to Cancer biology. J Exp Clin Cancer Res. 2019;38(1):115.

64.   Maehara J, Masugi Y, Abe T, Tsujikawa H, Kurebayashi Y, Ueno A, Ojima H, Okuda S, Jinzaki M, Shinoda M, Kitagawa Y, Oda Y, Honda H, Sakamoto M. Quantification of intratumoral collagen and elastin fibers within hepatocellular carcinoma tissues finds correlations with clinico-patho-radiological features. Hepatol Res. 2019.

65.   Sun Q, Baues M, Klinkhammer BM, Ehling J, Djudjaj S, Drude NI, Daniel C, Amann K, Kramann R, Kim H, Saez-Rodriguez J, Weiskirchen R, Onthank DC, Botnar RM, Kiessling F, Floege J, Lammers T, Boor P. Elastin imaging enables noninvasive staging and treatment monitoring of kidney fibrosis. Sci Transl Med. 2019;11(486).

66.   Levental KR, Yu H, Kass L, Lakins JN, Egeblad M, Erler JT, Fong SF, Csiszar K, Giaccia A, Weninger W, Yamauchi M, Gasser DL, Weaver VM. Matrix crosslinking forces tumor progression by enhancing integrin signaling. Cell. 2009;139(5):891-906.

67.   Butcher DT, Alliston T, Weaver VM. A tense situation: forcing tumour progression. Nat Rev Cancer. 2009;9(2):108-22.

68.   Pellicoro A, Aucott RL, Ramachandran P, Robson AJ, Fallowfield JA, Snowdon VK, Hartland SN, Vernon M, Duffield JS, Benyon RC, Forbes SJ, Iredale JP. Elastin accumulation is regulated at the level of degradation by macrophage metalloelastase (MMP-12) during experimental liver fibrosis. Hepatology. 2012;55(6):1965-75.

69.   Shikata T, Skai T. Elastogenesis in the liver. Acta Pathol Jpn. 1974;24(1):21-31.

70.   Wu H, Liu H, Liang C, Zhang S, Liu Z, Liu C, Liu Y, Hu M, Li C, Mei Y. Diffusion-weighted multiparametric MRI for monitoring longitudinal changes of parameters in rabbit VX2 liver tumors. J Magn Reson Imaging. 2016;44(3):707-14.

71.   Fang JS, Gillies RD, Gatenby RA. Adaptation to hypoxia and acidosis in carcinogenesis and tumor progression. Semin Cancer Biol. 2008;18(5):330-7.

72.   Gillies RJ, Robey I, Gatenby RA. Causes and consequences of increased glucose metabolism of cancers. J Nucl Med. 2008;49 Suppl 2:24S-42S.

73.   Cassim S, Pouyssegur J. Tumor Microenvironment: A Metabolic Player that Shapes the Immune Response. Int J Mol Sci. 2019;21(1).

74.   Bellone M, Calcinotto A, Filipazzi P, De Milito A, Fais S, Rivoltini L. The acidity of the tumor microenvironment is a mechanism of immune escape that can be overcome by proton pump inhibitors. Oncoimmunology. 2013;2(1):e22058.

75.   Coman D, Huang Y, Rao JU, De Feyter HM, Rothman DL, Juchem C, Hyder F. Imaging the intratumoral-peritumoral extracellular pH gradient of gliomas. NMR Biomed. 2016;29(3):309-19.

76.   van Zijl PC, Yadav NN. Chemical exchange saturation transfer (CEST): what is in a name and what isn't? Magn Reson Med. 2011;65(4):927-48.

77.   Malagari K, Kiakidis T, Pomoni M, Moschouris H, Emmanouil E, Spiridopoulos T, Sotirchos V, Tandeles S, Koundouras D, Kelekis A, Filippiadis D, Charokopakis A, Bouma E, Chatziioannou A, Dourakis S, Koskinas J, Karampelas T, Tamvakopoulos K, Kelekis N, Kelekis D. Pharmacokinetics, Safety, and Efficacy of Chemoembolization with Doxorubicin-Loaded Tightly Calibrated Small Microspheres in Patients with Hepatocellular Carcinoma. Cardiovasc Intervent Radiol. 2016;39(10):1379-91.

78.		Malagari K, Pomoni M, Moschouris H, Kelekis A, Charokopakis A, Bouma E, Spyridopoulos T, Chatziioannou A, Sotirchos V, Karampelas T, Tamvakopoulos C, Filippiadis D, Karagiannis E, Marinis A, Koskinas J, Kelekis DA. Chemoembolization of hepatocellular carcinoma with HepaSphere 30-60 mum. Safety and efficacy study. Cardiovasc Intervent Radiol. 2014;37(1):165-75.

79.		Odisio BC, Ashton A, Yan Y, Wei W, Kaseb A, Wallace MJ, Vauthey JN, Gupta S, Tam AL. Transarterial hepatic chemoembolization with 70-150 microm drug-eluting beads: assessment of clinical safety and liver toxicity profile. J Vasc Interv Radiol. 2015;26(7):965-71.

80.		Padia SA, Shivaram G, Bastawrous S, Bhargava P, Vo NJ, Vaidya S, Valji K, Harris WP, Hippe DS, Kogut MJ. Safety and efficacy of drug-eluting bead chemoembolization for hepatocellular carcinoma: comparison of small-versus medium-size particles. J Vasc Interv Radiol. 2013;24(3):301-6.

81.		Yeo DM, Oh SN, Jung CK, Lee MA, Oh ST, Rha SE, Jung SE, Byun JY, Gall P, Son Y. Correlation of dynamic contrast-enhanced MRI perfusion parameters with angiogenesis and biologic aggressiveness of rectal cancer: Preliminary results. J Magn Reson Imaging. 2015;41(2):474-80.

82.		Zachary JF. Mechanisms and Morphology of Cellular Injury, Adaptation, and Death. Pathologic basis of veterinary disease/ [edited by] James F Zachary. Sixth edition ed. St. Louis, Missouri, United States: Elsevier; 2017. p. 2-43.e19.

83.		Savic LJ, Schobert IT, Peters D, Walsh JJ, Laage-Gaupp FM, Hamm CA, Tritz N, Doemel LA, Lin M, Sinusas A, Schlachter T, Duncan JS, Hyder F, Coman D, Chapiro J. Molecular Imaging of Extracellular Tumor pH to Reveal Effects of Locoregional Therapy on Liver Cancer Microenvironment. Clin Cancer Res. 2019.

84.		Parvinian A, Casadaban LC, Gaba RC. Development, growth, propagation, and angiographic utilization of the rabbit VX2 model of liver cancer: a pictorial primer and "how to" guide. Diagn Interv Radiol. 2014;20(4):335-40.

Figure legends
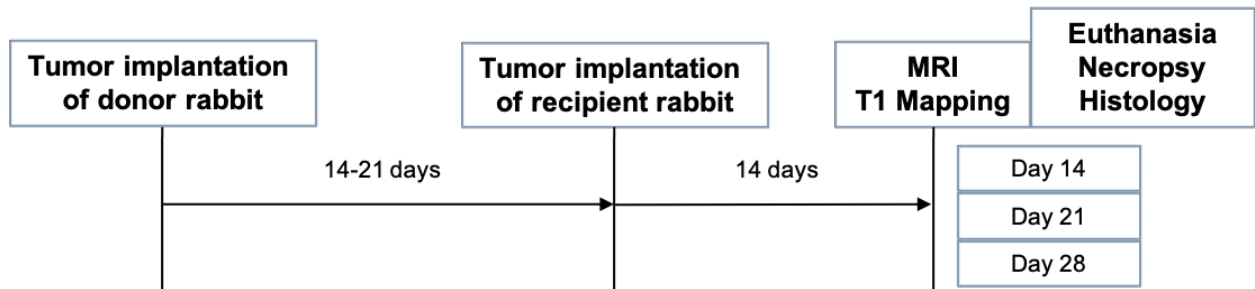
Figure 1: Experimental study design for the diagnostic T1 mapping study arm (A). This research was originally published in *Keller S, Borde T, Brangsch J, Adams LC, Kader A, Reimann C, Gebert P, Hamm B, Makowski M. Native T1 Mapping Magnetic Resonance Imaging as a Quantitative Biomarker for Characterization of the Extracellular Matrix in a Rabbit Hepatic Cancer Model. Biomedicines. 2020 Oct 13;8(10):412.* This flowchart was adapted from the above-mentioned publication for clarification.
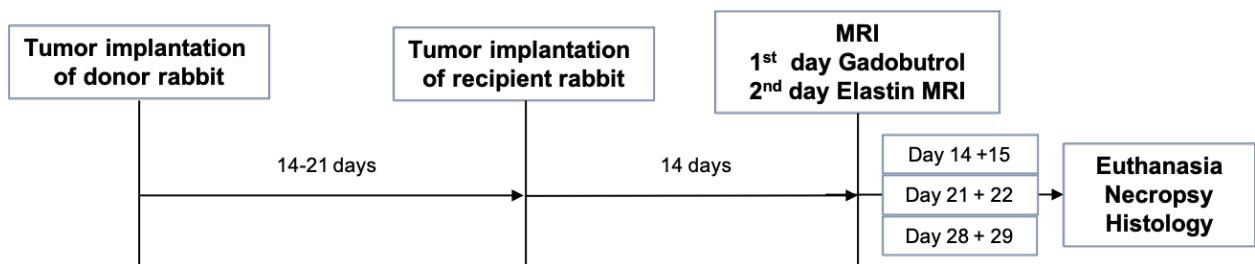
Figure 2: Experimental study design for the diagnostic Elastin-specific MRI study arm (B). This research was originally published in *Keller S, Borde T, Brangsch J, Reimann C, Kader A, Schulze D, Buchholz R, Kaufmann JO, Karst U, Schellenberger E, Hamm B, Makowski MR. Assessment of the hepatic tumor extracellular matrix using elastin-specific molecular magnetic resonance imaging in an experimental rabbit cancer model. Sci Rep. 2020 Nov 27;10(1):20785.* This flowchart was adapted from the above-mentioned publication for clarification.
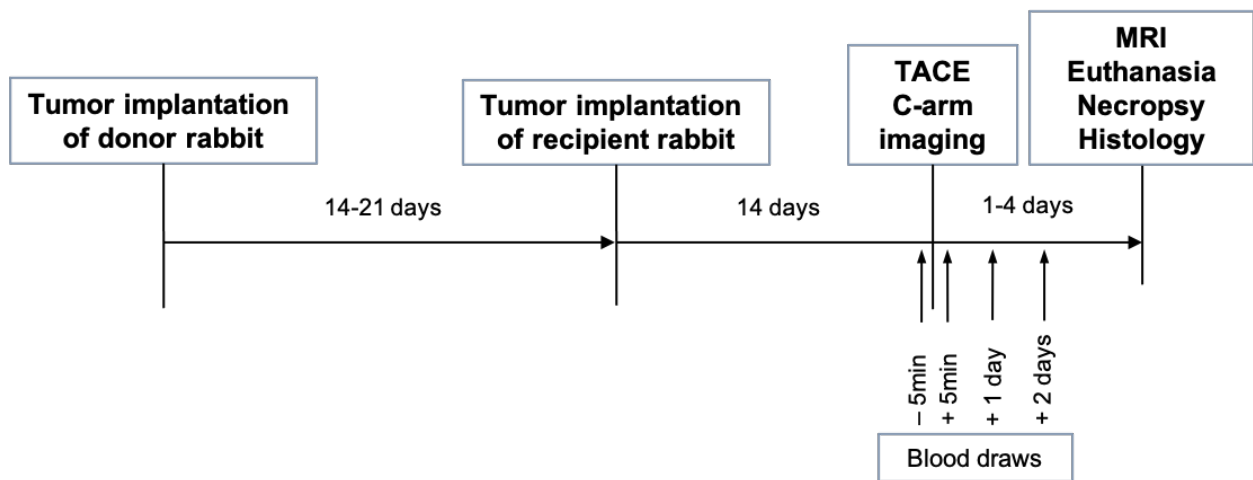
Figure 3: **Experimental study design for the experimental, translational DEB-TACE treatment arm (C).** This research was originally published in *Borde T, Laage Gaupp F, Geschwind JF, Savic LJ, Miszczuk M, Rexha I, Adam L, Walsh JJ, Huber S, Duncan JS, Peters DC, Sinusas A, Schlachter T, Gebauer B, Hyder F, Coman D, van Breugel JMM, Chapiro J. Idarubicin-Loaded ONCOZENE Drug-Eluting Bead Chemoembolization in a Rabbit Liver Tumor Model: Investigating Safety, Therapeutic Efficacy, and Effects on Tumor Microenvironment. J Vasc Interv Radiol. 2020 Oct;31(10):1706-1716.e1.* This flowchart depicting the study design of the DEB-TACE treatment arm was implemented from the above-mentioned publication for visual support of the study design.
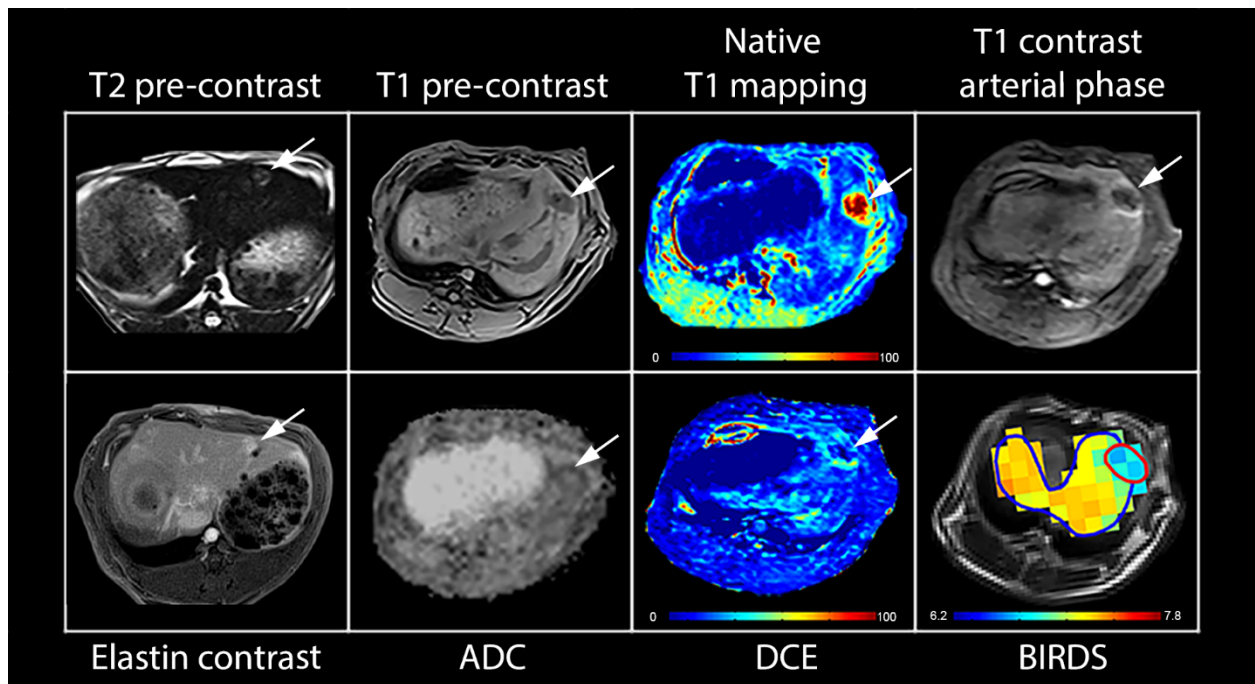
Figure 4: Overview of non-invasive MRI sequences in untreated animals (study groups A-C). This research was partly published in *Borde T, Laage Gaupp F, Geschwind JF, Savic LJ, Miszczuk M, Rexha I, Adam L, Walsh JJ, Huber S, Duncan JS, Peters DC, Sinusas A, Schlachter T, Gebauer B, Hyder F, Coman D, van Breugel JMM, Chapiro J. Idarubicin-Loaded ONCOZENE Drug-Eluting Bead Chemoembolization in a Rabbit Liver Tumor Model: Investigating Safety, Therapeutic Efficacy, and Effects on Tumor Microenvironment. J Vasc Interv Radiol. 2020 Oct;31(10):1706-1716.e1.* AND *Keller S, Borde T, Brangsch J, Reimann C, Kader A, Schulze D, Buchholz R, Kaufmann JO, Karst U, Schellenberger E, Hamm B, Makowski MR. Assessment of the hepatic tumor extracellular matrix using elastin-specific molecular magnetic resonance imaging in an experimental rabbit cancer model. Sci Rep. 2020 Nov 27;10(1):20785.* AND *Keller S, Borde T, Brangsch J, Adams LC, Kader A, Reimann C, Gebert P, Hamm B, Makowski M. Native T1 Mapping Magnetic Resonance Imaging as a Quantitative Biomarker for Characterization of the Extracellular Matrix in a Rabbit Hepatic Cancer Model. Biomedicines. 2020 Oct 13;8(10):412.* This figure was created in summary of the above-mentioned, three published articles and depicts the different, non-invasive MRI sequences performed in these studies.

IV. Affidavit / Eidesstattliche Versicherung

„Ich, Tabea Borde, versichere an Eides statt durch meine eigenhändige Unterschrift, dass ich die vorgelegte Dissertation mit dem Thema: *Quantitative bildbasierte Prädiktoren zur Charakterisierung der Tumormikroumgebung in Lebertumoren für die Tumordetektierung und Evaluierung des Therapieansprechen / Quantitative Imaging Biomarkers to Characterize the Tumor Microenvironment in Liver Tumors for Tumor Detection and Therapy Response Assessment* selbstständig und ohne nicht offengelegte Hilfe Dritter verfasst und keine anderen als die angegebenen Quellen und Hilfsmittel genutzt habe.

Alle Stellen, die wörtlich oder dem Sinne nach auf Publikationen oder Vorträgen anderer Autoren/innen beruhen, sind als solche in korrekter Zitierung kenntlich gemacht. Die Abschnitte zu Methodik (insbesondere praktische Arbeiten, Laborbestimmungen, statistische Aufarbeitung) und Resultaten (insbesondere Abbildungen, Graphiken und Tabellen) werden von mir verantwortet.

Ich versichere ferner, dass ich die in Zusammenarbeit mit anderen Personen generierten Daten, Datenauswertungen und Schlussfolgerungen korrekt gekennzeichnet und meinen eigenen Beitrag sowie die Beiträge anderer Personen korrekt kenntlich gemacht habe (siehe Anteilserklärung). Texte oder Textteile, die gemeinsam mit anderen erstellt oder verwendet wurden, habe ich korrekt kenntlich gemacht.

Meine Anteile an etwaigen Publikationen zu dieser Dissertation entsprechen denen, die in der untenstehenden gemeinsamen Erklärung mit dem Erstbetreuer, angegeben sind. Für sämtliche im Rahmen der Dissertation entstandenen Publikationen wurden die Richtlinien des ICMJE (International Committee of Medical Journal Editors; www.icmje.og) zur Autorenschaft eingehalten. Ich erkläre ferner, dass ich mich zur Einhaltung der Satzung der Charité – Universitätsmedizin Berlin zur Sicherung Guter Wissenschaftlicher Praxis verpflichte.

Weiterhin versichere ich, dass ich diese Dissertation weder in gleicher noch in ähnlicher Form bereits an einer anderen Fakultät eingereicht habe.

Die Bedeutung dieser eidesstattlichen Versicherung und die strafrechtlichen Folgen einer unwahren eidesstattlichen Versicherung (§§156, 161 des Strafgesetzbuches) sind mir bekannt und bewusst."

_____   _____

Datum   Unterschrift

V. Detailed statement of contributions / Ausführliche Anteilserklärung an den erfolgten Publikationen im Rahmen des Promotionsverfahren zum MD/PhD

Tabea Borde hatte folgenden Anteil an den folgenden Publikationen:

Borde T, Laage Gaupp F, Geschwind JF, Savic LJ, Miszczuk M, Rexha I, Adam L, Walsh JJ, Huber S, Duncan JS, Peters DC, Sinusas A, Schlachter T, Gebauer B, Hyder F, Coman D, van Breugel JMM, Chapiro J. Idarubicin-Loaded ONCOZENE Drug-Eluting Bead Chemoembolization in a Rabbit Liver Tumor Model: Investigating Safety, Therapeutic Efficacy, and Effects on Tumor Microenvironment. J Vasc Interv Radiol. 2020.

Beitrag im Einzelnen:

- Konzept und Design der Studie in Zusammenarbeit mit den Letztautoren (J.M.M.vB, J.C.), dabei insb. die Erarbeitung der Hypothesen und Fragestellungen sowie die Planung der Verbindung der Studienkomponenten (Tierexperiment – DEB-TACE mit zwei unterschiedlichen Mikrosphärendurchmessern und simultane Charakterisierung des Tumormikromileus mit neuen MRT-Sequenzen prä- und post-therapeutisch).
- Ausgiebige Literaturrecherche zum Thema Vektoren und Kalibrierung der Mikrosphären für TACE zur geeigneten Auswahl der Mikrosphären in Zusammenarbeit mit Boston Scientific.
- Planung und Organisation sowohl der Tierakquirierung (Bestellung der Tiere von Charles River Laboratories) als auch der Tierhaltung (im Yale Translational Research Imaging Center) und eigenständige Durchführung der prä-, peri- sowie post-operativen Nachsorge (tägliche klinische Untersuchung der Tiere, regelmäßige Temperatur- und Herzfrequenzüberprüfung sowie Applikation post-therapeutischer Schmerzmedikation).
- Randomisierung der Studientiere in die Kontroll-, 40μm- und 100μm-Gruppe.
- Planung, Organisation, Koordination und Terminierung der operativen Durchführung der Studie, insbesondere da mehrere Zentren (Magnetic Resonsance Research Center, Translational Research Imaging Center, Department of Biomedical Engineering und Boston Scientific) involviert waren.
- Durchführung der Tumorimplantation sowohl der Donor-, als auch der Studientiere in Zusammenarbeit mit J.C. und F.LG.
- Durchführung der transarteriellen Chemoembolisation in Zusammenarbeit mit J.C., F.LG. und T.S.
- Eigenständige Blutprobenentnahme zu den jeweiligen Zeitpunkten (prä- sowie post-therapeutisch). Aus der konsekutiven Auswertung eigenständig erschaffenes Diagramm „Figure 3".
- Bildakquirierung (MRT-Durchführung) und software-basierte Bildanalyse der CT und neuen MRT-Sequenzen, sowie Extrahierung von T1, DCE, ADC und BIRDS maps aus

den Rohdaten und Quantifizierung der Parameter unter Supervision des Magnetic Resonance Research Center (D.C.P., F.H., D.C., J.J.W., S.H.). Daraus entstanden die selbstständig erschaffenen Graphiken/Diagramme „Figure 2, 4 und 5".

- Selbstständige Euthanasie, Autopsie und Gewebeprobenentnahme nach Beendigung der MRT-Bildgebung, sowie direktes Prozessieren und geeignete Lagerung der Gewebeproben.
- Histopathologische Aufarbeitung der Proben mithilfe eines Pathologen und mikroskopische, quantitative Auswertung und Analyse der Histologiebefunde (daraus entstandene Graphik „Figure 6").
- Organisation der externen Durchführung der Fluoreszenzmikroskopie sowie der VEGF Antikörperanalyse, jedoch eigenständige Auswertung der Daten und selbständige Erstellung der Graphiken „Figure 7 und E1".
- Korrelation der Bildgebungsresultate (der DCE-, DWI- und BIRDS-Sequenzen) mit den makroskopischen, histopathologischen (H&E, PCNA, TUNEL, HIF-1α, Pimonodazole) und fluoreszenzmikroskopischen Befunden und Formulierung geeigneter Zusammenhänge im Diskussionsteil.
- Eigenständige Wahl und Durchführung der Statistik (explizit Test auf Normalverteilung, Kruskal-Wallis Test, um die Charakteristika der Studientiere zu vergleichen sowie Mann-Whitney U Test, um die Unterschiede zwischen den einzelnen Gruppen zu vergleichen). Aus den Ergebnissen meiner statistischen Auswertung resultierende Diagramme „Figure 3, 5, E1".
- Die Datenvisualisierung aller Graphiken „Figures 2, 4, 6 und 7" entstanden ausschließlich selbstständig.
- Vollständig selbstständiger Entwurf und Finalisierung des Manuskripts/ der Publikation inklusive Literaturauswahl, dann Revision anhand der Anmerkungen der Koautoren, selbstständige Einreichung bei JVIR und Adressierung der Kommentare der Reviewer.
- Vorstellung der Studie auf den wissenschaftlichen Kongressen WCIO (World Conference of Interventional Oncology) und dem RSNA (Radiological Society of North America).

Keller S, Borde T, Brangsch J, Reimann C, Kader A, Schulze D, Buchholz R, Kaufmann JO, Karst U, Schellenberger E, Hamm B, Makowski MR. Assessment of the hepatic tumor extracellular matrix using elastin-specific molecular magnetic resonance imaging in an experimental rabbit cancer model. Sci Rep. 2020.

Beitrag im Einzelnen:

- Konzept und Design der Studie in Zusammenarbeit mit der Erstautorin (S.K.), dabei insb. die Erarbeitung der Hypothesen und Fragestellungen, inwiefern die Applizierung eines Elastin-spezifischen Kontrastmittels die Detektion und Charakterisierung von soliden

Lebertumoren erleichtern bzw. welche zukünftig hilfreichen Neuinformationen dabei entstehen können.

- Ausgiebige Literaturrecherche zur Anwendung von Elastin-spezifischen Kontrastmitteln und deren Aussagekraft.

- Unterstützung in der Planung und Organisation sowohl der Tierakquirierung als auch der Tierhaltung (in der Charité Mitte und Virchow) und Durchführung der prä-, peri- sowie post-operativen Nachsorge (regelmäßige klinische Untersuchung sowie Applikation post-therapeutischer Schmerzmedikamente).

- Mithilfe in der Planung, Organisation und zeitliche Koordination der Tumorimplantationen und konsekutiver MRT-Bildgebung.

- Teils selbstständige Tumorimplantation sowohl der Donor-, als auch der Studientiere.

- Bildakquirierung (teils selbstständige Durchführung der MRT-Bildgebung) und software-basierte Bildanalyse der Elastin-kontrastmittelverstärkten MRT-Sequenzen inklusive der Extrahierung des Elastin-Enhancements aus den MRT-Rohdaten in Zusammenarbeit mit S.K.

- Selbstständige Euthanasie, Autopsie und Gewebeprobenentnahme nach Beendigung der MRT-Bildgebung, sowie direktes Prozessieren und geeignete Lagerung der Gewebeproben.

- Histopathologische Aufarbeitung der Proben mithilfe von S.K. und quantitative Auswertung und Analyse der Histologiebefunde.

- Korrelation der Bildgebungsresultate (der Elastin-kontrastmittelverstärkten Sequenzen) mit den makroskopischen, histopathologischen (extrazelluläre Elastinkonzentration) und Massenspektronomie-Resultaten in Zusammenarbeit mit S.K. (dabei Erstellung der Graphik „Figure 1" und „Figure 4").

- In Zusammenarbeit mit S.K. Schreiben des Manuskripts inklusive Literaturwahl. Darüber hinaus Hauptanteil in der Revision des Manuskriptes.

Keller S, Borde T, Brangsch J, Adams LC, Kader A, Reimann C, Gebert P, Hamm B, Makowski M. Native T1 Mapping Magnetic Resonance Imaging as a Quantitative Biomarker for Characterization of the Extracellular Matrix in a Rabbit Hepatic Cancer Model. Biomedicines. 2020.

Beitrag im Einzelnen:

- Konzept und Design der Studie in Zusammenarbeit mit der Erstautorin (S.K.), dabei insb. die Erarbeitung der Hypothesen und Fragestellungen, inwiefern das native T1 Mapping die Detektion und Charakterisierung von soliden Lebertumoren erleichtern bzw. beschleunigen kann.

- Ausgiebige Literaturrecherche zur Aussagekraft und zu den bisherigen Anwendungsfeldern von nativem T1 Mapping.
- Unterstützung in der Planung und Organisation sowohl der Tierakquirierung als auch der Tierhaltung (in der Charité Mitte und Virchow) und Durchführung der prä-, peri- sowie post-operativen Nachsorge (regelmäßige klinische Untersuchung sowie Applikation post-therapeutischer Schmerzmedikamente).
- Mithilfe in der Planung, Organisation und zeitliche Koordination der Tumorimplantationen und konsekutiver MRT-Bildgebung.
- Teils selbstständige Tumorimplantation sowohl der Donor-, als auch der Studientiere.
- Bildakquirierung (teils selbstständige Durchführung der MRT-Bildgebung) und software-basierte Bildanalyse insbesondere der nativen T1-Sequenzen inklusive der Extrahierung von T1 Maps aus den MRT-Rohdaten in Zusammenarbeit mit S.K.
- Selbstständige Euthanasie, Autopsie und Gewebeprobenentnahme nach Beendigung der MRT-Bildgebung, sowie direktes Prozessieren und geeignete Lagerung der Gewebeproben.
- Histopathologische Aufarbeitung der Proben mithilfe von S.K. und quantitative Auswertung und Analyse der Histologiebefunde.
- Korrelation der Bildgebungsresultate (der T1 Maps) mit den makroskopischen, histopathologischen (wie z.B. der Kollagenkonzentration) Ergebnissen in Zusammenarbeit mit S.K. (dabei Erstellung der Graphik „Figure 2" und „Figure 3").
- In Zusammenarbeit mit S.K. Schreiben des Manuskripts inkl. Literaturwahl. Insb. vollständig eigenständige Formulierung der Diskussion. Darüber hinaus Hauptanteil in der Revision des Manuskriptes.

_____

Unterschrift, Datum und Stempel des/der erstbetreuenden Hochschullehrers/in

_____

Unterschrift des Doktoranden/der Doktorandin

VI. Publications including the excerpt of the journal summary list

Selected Categories: "RADIOLOGY, NUCLEAR MEDICINE and MEDICAL IMAGING":

Borde T, Laage Gaupp F, Geschwind JF, Savic LJ, Miszczuk M, Rexha I, Adam L, Walsh JJ, Huber S, Duncan JS, Peters DC, Sinusas A, Schlachter T, Gebauer B, Hyder F, Coman D, van Breugel JMM, Chapiro J. Idarubicin-Loaded ONCOZENE Drug-Eluting Bead Chemoembolization in a Rabbit Liver Tumor Model: Investigating Safety, Therapeutic Efficacy, and Effects on Tumor Microenvironment. J Vasc Interv Radiol. 2020 Oct;31(10):1706-1716.e1. doi: 10.1016/j.jvir.2020.04.010.

https://doi.org/10.1016/j.jvir.2020.04.010

Publication received: 19 November 2019

Journal Data Filtered By: **Selected JCR Year: 2018** Selected Editions: SCIE,SSCI
Selected Categories: **"RADIOLOGY, NUCLEAR MEDICINE and MEDICAL
IMAGING"** Selected Category Scheme: WoS
Gesamtanzahl: 129 Journale

Rank	Full Journal Title	Total Cites	Journal Impact Factor	Eigenfactor Score
1	JACC-Cardiovascular Imaging	8,801	10.975	0.026160
2	MEDICAL IMAGE ANALYSIS	7,694	8.880	0.013370
3	IEEE TRANSACTIONS ON MEDICAL IMAGING	19,545	7.816	0.024990
4	RADIOLOGY	54,641	7.608	0.061300
5	JOURNAL OF NUCLEAR MEDICINE	27,551	7.354	0.037990
6	EUROPEAN JOURNAL OF NUCLEAR MEDICINE AND MOLECULAR IMAGING	15,406	7.182	0.024760
7	CLINICAL NUCLEAR MEDICINE	4,922	6.498	0.007680
8	INTERNATIONAL JOURNAL OF RADIATION ONCOLOGY BIOLOGY PHYSICS	45,833	6.203	0.046810
9	INVESTIGATIVE RADIOLOGY	6,563	6.091	0.011150
10	Circulation-Cardiovascular Imaging	5,456	5.813	0.018480
11	NEUROIMAGE	99,720	5.812	0.132720
12	ULTRASOUND IN OBSTETRICS & GYNECOLOGY	12,336	5.595	0.020140
13	European Heart Journal-Cardiovascular Imaging	5,498	5.260	0.021650
14	RADIOTHERAPY AND ONCOLOGY	17,873	5.252	0.027470
15	Photoacoustics	512	5.250	0.001330
16	JOURNAL OF CARDIOVASCULAR MAGNETIC RESONANCE	5,113	5.070	0.014020
17	ULTRASCHALL IN DER MEDIZIN	2,238	4.613	0.003700
18	HUMAN BRAIN MAPPING	22,040	4.554	0.043230
19	JOURNAL OF NUCLEAR CARDIOLOGY	3,711	4.112	0.004480
20	EUROPEAN RADIOLOGY	19,597	3.962	0.033870

Selected JCR Year: 2018; Selected Categories: "RADIOLOGY, NUCLEAR MEDICINE and MEDICAL IMAGING"

Rank	Full Journal Title	Total Cites	Journal Impact Factor	Eigenfactor Score
21	RADIOGRAPHICS	11,768	3.923	0.009170
22	Biomedical Optics Express	9,547	3.910	0.021750
23	MAGNETIC RESONANCE IN MEDICINE	32,648	3.858	0.034990
24	SEMINARS IN NUCLEAR MEDICINE	2,245	3.798	0.002710
25	Journal of the American College of Radiology	4,191	3.785	0.009760
26	JOURNAL OF MAGNETIC RESONANCE IMAGING	17,147	3.732	0.027800
27	KOREAN JOURNAL OF RADIOLOGY	2,687	3.730	0.004800
28	INTERNATIONAL JOURNAL OF HYPERTHERMIA	3,552	3.589	0.004020
29	EJNMMI Physics	394	3.475	0.001350
30	NMR IN BIOMEDICINE	7,511	3.414	0.014790
31	MOLECULAR IMAGING AND BIOLOGY	2,543	3.341	0.005360
32	Journal of Cardiovascular Computed Tomography	1,711	3.316	0.004430
33	COMPUTERIZED MEDICAL IMAGING AND GRAPHICS	2,464	3.298	0.002990
34	AMERICAN JOURNAL OF NEURORADIOLOGY	23,231	3.256	0.028010
35	MEDICAL PHYSICS	26,715	3.177	0.030870
36	AMERICAN JOURNAL OF ROENTGENOLOGY	33,633	3.161	0.028540
37	CANCER IMAGING	1,406	3.153	0.002220
38	Quantitative Imaging in Medicine and Surgery	1,072	3.074	0.002420
39	PHYSICS IN MEDICINE AND BIOLOGY	27,458	3.030	0.031970
40	EJNMMI Research	1,408	3.000	0.004320
41	EUROPEAN JOURNAL OF RADIOLOGY	12,871	2.948	0.019480
42	Radiation Oncology	5,669	2.895	0.012980

Selected JCR Year: 2018; Selected Categories: "RADIOLOGY, NUCLEAR MEDICINE and MEDICAL IMAGING"

Rank	Full Journal Title	Total Cites	Journal Impact Factor	Eigenfactor Score
43	MAGNETIC RESONANCE MATERIALS IN PHYSICS BIOLOGY AND MEDICINE	1,600	2.836	0.003630
44	JOURNAL OF VASCULAR AND INTERVENTIONAL RADIOLOGY	8,813	2.828	0.011270
45	Clinical Neuroradiology	798	2.800	0.002250
46	Practical Radiation Oncology	1,563	2.794	0.005010
47	RADIATION RESEARCH	8,561	2.779	0.006480
48	SEMINARS IN RADIATION ONCOLOGY	2,395	2.741	0.003600
49	STRAHLENTHERAPIE UND ONKOLOGIE	2,949	2.717	0.004500
50	ULTRASONICS	7,026	2.598	0.009090
51	JOURNAL OF DIGITAL IMAGING	2,191	2.572	0.003680
52	JOURNAL OF BIOMEDICAL OPTICS	13,787	2.555	0.016940
53	Physica Medica-European Journal of Medical Physics	2,641	2.532	0.006270
54	NEURORADIOLOGY	5,656	2.504	0.007020
55	NUCLEAR MEDICINE AND BIOLOGY	3,858	2.492	0.004230
56	ULTRASONIC IMAGING	1,117	2.490	0.000860
57	Diagnostic and Interventional Imaging	1,359	2.486	0.003400
58	JOURNAL OF NEURORADIOLOGY	985	2.467	0.001440
59	Dose-Response	997	2.451	0.001460
60	Zeitschrift fur Medizinische Physik	558	2.322	0.001360
61	ACADEMIC RADIOLOGY	5,625	2.267	0.008230
62	INTERNATIONAL JOURNAL OF RADIATION BIOLOGY	4,537	2.266	0.003740
63	ULTRASOUND IN MEDICINE AND BIOLOGY	10,769	2.205	0.012790
64	International Journal of Computer Assisted Radiology and Surgery	2,416	2.155	0.005160

Selected JCR Year: 2018; Selected Categories: "RADIOLOGY, NUCLEAR MEDICINE and MEDICAL IMAGING"

Selected Category: "MULTIDISCIPLINARY SCIENCES":

Keller S, Borde T, Brangsch J, Reimann C, Kader A, Schulze D, Buchholz R, Kaufmann JO, Karst U, Schellenberger E, Hamm B, Makowski MR. Assessment of the hepatic tumor extracellular matrix using elastin-specific molecular magnetic resonance imaging in an experimental rabbit cancer model. Sci Rep. 2020 Nov 27;10(1):20785.

Publication received: 20 June 2020

Journal Data Filtered By: **Selected JCR Year: 2018** Selected Editions: SCIE,SSCI Selected Categories: **"MULTIDISCIPLINARY SCIENCES"** Selected Category Scheme: WoS
Gesamtanzahl: 69 Journale

Rank	Full Journal Title	Total Cites	Journal Impact Factor	Eigenfactor Score
1	NATURE	745,692	43.070	1.285010
2	SCIENCE	680,994	41.037	1.070190
3	National Science Review	1,842	13.222	0.006500
4	Science Advances	21,901	12.804	0.110010
5	Nature Communications	243,793	11.878	1.103290
6	Nature Human Behaviour	1,230	10.575	0.006550
7	PROCEEDINGS OF THE NATIONAL ACADEMY OF SCIENCES OF THE UNITED STATES OF AMERICA	661,118	9.580	1.022190
8	Science Bulletin	3,569	6.277	0.009840
9	Scientific Data	3,240	5.929	0.015610
10	Frontiers in Bioengineering and Biotechnology	1,994	5.122	0.006540
11	Journal of Advanced Research	2,691	5.045	0.004780
12	Research Synthesis Methods	1,932	5.043	0.005420
13	GigaScience	2,674	4.688	0.012510
14	Annals of the New York Academy of Sciences	46,385	4.295	0.025840
15	Scientific Reports	302,086	4.011	1.061540
16	Journal of the Royal Society Interface	12,933	3.224	0.029190
17	NPJ Microgravity	203	3.111	0.000670
18	PHILOSOPHICAL TRANSACTIONS OF THE ROYAL SOCIETY A-MATHEMATICAL PHYSICAL AND ENGINEERING SCIENCES	19,227	3.093	0.028200

scientific reports

Check for updates

OPEN

Assessment of the hepatic tumor extracellular matrix using elastin-specific molecular magnetic resonance imaging in an experimental rabbit cancer model

Sarah Keller[1✉], Tabea Borde[1], Julia Brangsch[1], Carolin Reimann[1], Avan Kader[1], Daniel Schulze[2], Rebecca Buchholz[3], Jan O. Kaufmann[1,4,5], Uwe Karst[3], Eyk Schellenberger[1], Bernd Hamm[1] & Marcus R. Makowski[1,6]

To investigate the imaging performance of an elastin-specific molecular magnetic resonance imaging (MRI) probe with respect to the extracellular matrix (ECM) in an experimental hepatic cancer model. Twelve rabbits with hepatic VX2 tumors were examined using 3 T MRI 14, 21, and 28 days after tumor implantation for two subsequent days (gadobutrol, day 1; elastin-specific probe, day 2). The relative enhancement (RE) of segmented tumor regions (central and margin) and the peritumoral matrix was calculated using pre-contrast and delayed-phase T1w sequences. MRI measurements were correlated to histopathology and element-specific and spatially resolved mass spectrometry (MS). Mixed-model analysis was performed to assess the performance of the elastin-specific probe. In comparison to gadobutrol, the elastin probe showed significantly stronger RE, which was pronounced in the tumor margin (day 14–28: $P \leq 0.007$). In addition, the elastin probe was superior in discriminating between tumor regions ($\chi^2(4) = 65.87$; $P < 0.001$). MRI-based measurements of the elastin probe significantly correlated with the ex vivo elastinstain (R = .84; $P < 0.001$) and absolute gadolinium concentrations (ICP-MS: R = .73, $P < 0.01$). LA-ICP-MS imaging confirmed the colocalization of the elastin-specific probe with elastic fibers. Elastin-specific molecular MRI is superior to non-specific gadolinium-based contrast agents in imaging the ECM of hepatic tumors and the peritumoral tissue.

Abbreviations

ECM	Extracellular matrix
ESMA	Elastin-specific molecular agent
EvG	Miller's elastic van Gieson
FELASA	Federation of Laboratory Animal Science Associations
GRE	Gradient-recalled-echo (sequence)
H&E	Hematoxylin and eosin
HCC	Hepatocellular carcinoma
ICP-MS	Inductively coupled plasma mass spectroscopy
LA-ICP-MS	Laser ablation-inductively coupled plasma-mass spectrometry

[1]Department of Radiology, Charité - Universitätsmedizin Berlin, corporate member of Freie Universität Berlin, Humboldt-Universität Zu Berlin, and Berlin Institute of Health, Charitéplatz 1, 10117 Berlin, Germany. [2]Department of Education Science and Psychology, FU Berlin, Berlin, Germany. [3]Institute of Inorganic and Analytical Chemistry, Westfälische Wilhelms-Universität Münster, Münster, Germany. [4]Division 1.5 Protein Analysis, Federal Institute for Materials Research and Testing (BAM), Berlin, Germany. [5]Department of Chemistry, Humboldt-Universität Zu Berlin, Berlin, Germany. [6]Department of Diagnostic and Interventional Radiology, School of Medicine & Klinikum Rechts Der Isar, Technical University of Munich, Munich (TUM), Munich, Germany. ✉email: sarah.keller@charite.de

60

MRI	Magnetic resonance imaging
RE	Relative enhancement
US	Ultrasound
VIBE	Volumetric interpolated breath-hold examination

The prevalence of hepatocellular carcinoma (HCC) is globally increasing with a high mortality rate[1]. Despite advances in therapeutic and diagnostic strategies in the last decades, the tumor resistance to treatment remains a major challenge for targeted therapy[2]. The tumor responsiveness to local and systemic therapy is not only dependent on the reduction of tumor cell proliferation, but also on the sensitivity of the peritumoral extracellular matrix (ECM) towards anticancer agents[3,4] in various primary liver cancers and metastasis[5–7]. In the tumor microenvironment, stromal cells express an altered ECM that provides mechanical and biochemical protection to tumor cells and the surrounding microenvironment[2]. Collagens, laminins and fibronectins, in particular, directly and indirectly, interact with tumor cells and are able to change the function and phenotype due to external stimuli, such as therapy[8,9]. Elastin, another component of the ECM has recently been identified as an independent predictor of HCC development[10]. The VX2 rabbit model for liver cancer is a well-studied model for testing and evaluation of preclinical interventional[11,12] and systemic therapies[13] on an HCC surrogate tumor. A recent ultrasound-based therapy study has linked the importance of the ECM for therapy options by using microbubbles to influence the interstitial fluid pressure in this model[14]. Furthermore, it could already be shown that brachytherapy using the genetically engineered peptide polymer elastin-like polypeptide labelled with I(131) in the VX2 liver tumors has a strong labelling efficiency and thus a high antitumor effect[15]. Non-invasive magnetic resonance imaging (MRI) biomarkers could enhance the current knowledge about ECM interactions following tumor progression and therapy. However, no molecular contrast agents have yet been approved for the imaging of hepatic tumors in clinical routine.

Among the recently available standard extracellular MRI contrast agents, gadobutrol (gadolinium-DO3A-butriol, Gadovist 1.0; Bayer Schering Pharma, Berlin, Germany) is one of the first commercially available 1 M gadolinium chelates belonging to the class of macrocyclic, neutral gadolinium complexes[16–18]. Various comparative studies of 0.5 M and 1 M gadobutrol in experimental and clinical HCC have confirmed its effectiveness in tumor detection. In particular, gadobutrol 1 M shows high contrast efficiency and thus increased detectability even of small intrahepatic tumors[17,19]. In intramuscular VX2 rabbit tumors, 1 M gadobutrol showed increased contrast enhancement, better tumor-to-muscle differentiation and better delineation of the tumor border than 0.5 M gadopentatate dimeglumine[20]. However, with regard to the histopathological grading of HCC in patients, gadobutrol has not yet been shown to have a predictive effect[21]. Furthermore, there are no studies that have investigated whether gadobutrol can differentiate the different tumor regions and their ECM. With reference to the above, these data are of particular interest for a better assessment of the therapeutic effects of invasive and systemic procedures.

Molecular elastin-specific MR contrast agents have been already successfully used to study the ECM remodeling in cardiovascular disease with results indicating a large translational potential[22–24]. In this context, elastin-specific molecular MRI could not only quantify the elastin content in arteriosclerotic plaques on the basis of signal intensity, but also predict potential rupture sites in the course of an aortic aneurysm in follow-up studies[22,23]. In a mouse model for Marfan's disease, elastin-specific MRI reliably detected a decrease in aortic wall elastin concentration compared to wild-type controls[25]. To date, there are no records of studies that have used elastin-specific molecular MRI to characterize the ECM in hepatic tumors. Assuming that hepatic tumors have an increased expression of collagens, including elastin[10], the hypothesis arises that elastin-specific contrast agents allow for a more clearly defined enhancement and differentiation of tumor regions based on the composition of their ECM than conventional gadolinium-based contrast agents.

The aim of this study was to test the potential of an elastin-specific molecular MR probe to assess and quantify the peritumoral matrix in a rabbit VX2 hepatic cancer model.

Results

MR imaging. The average tumor volume measured in the native T1 sequences was 0.41 (±0.38) cm³. After intravenous contrast agent administration of gadobutrol on day 1, there was a shallow enhancement of the tumor regions, accentuated during the venous and late contrast agent phase. Tumor enhancement was visually potentiated after administration of the elastin-specific probe on day 2 (Fig. 1A). The increased enhancement using the elastin-specific probe corresponded to the ex vivo histological EvG stain (Fig. 1B). The pronounced enhancement following the injection of the elastin-specific probe was confirmed by the quantitative MR image analysis.

Relative enhancement (RE). Time and region had a significant impact on RE when compared to the null model ($\chi^2(14) = 69.23$, $P < 0.001$). More importantly, the applied contrast agent had an additional significant effect above time and region ($\chi^2(15) = 120.83$, $P < 0.001$). The elastin-specific contrast agent showed a significant higher RE compared to gadobutrol in the central, marginal, and peritumoral region. This difference was pronounced in the tumor margin (Fig. 2). Post hoc tests were carried out to gain further insight into the differences of the agents depending on regions and time points. In the post hoc analysis, tumor areas showed significant differences between gadobutrol and elastin-specific contrast uptake in the tumor margin on day 14 (difference 1.86; $P < 0.001$), day 21 (difference 1.68; $P = 0.007$), and day 28 (difference 1.81; $P < 0.001$). In the peritumoral region, gains of elastin-specific probes were observed on day 14 (difference 1.01; $P = 0.03$) and day 28 (difference 1.18; $P = 0.005$), in the central regions on day 21 (difference 1.44; $P = 0.034$) and day 28 (difference 1.75; $P < 0.001$) (Table 1). The RE difference between the two agents in normal liver parenchyma and back muscles was not sig-

61
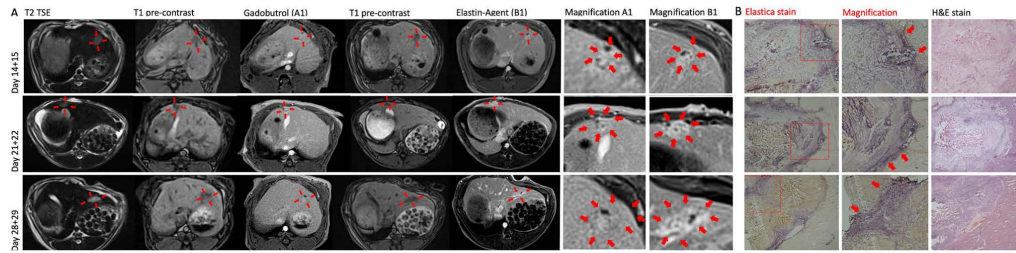
Figure 1. In vivo and ex vivo imaging of untreated VX2 liver tumors. (**A**) MR imaging of the liver at three different time points (day 14 + 15, 21 + 22, 28 + 29) following implantation. Left–right: T2w imaging, unenhanced T1 weighted imaging (day 1), gadobutrol enhanced T1 weighted imaging (day 1, A1), unenhanced T1 weighted imaging (day 2), elastin-specific MR probe T1 weighted imaging (day 2, B1), magnification of A1 and B1. (**B**) Histopathology using Elastica van Giesson and H&E stain. Strong expression of elastic fibers in the hepatic tumor, pronounced in the tumor margin. 2 × magnification (Elastica and H&E stain), 10 × magnification (Elastica stain magnification).
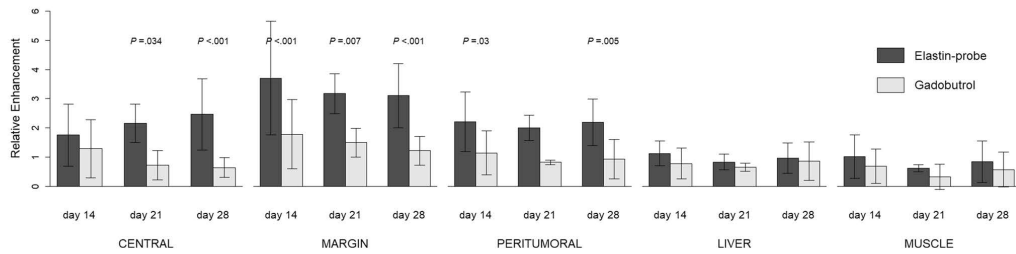
Figure 2. Relative Enhancement (RE) depending on the contrast agent and latency time for the different regions. RE for the liver and muscle is included as reference. Error bars represent standard deviation. P values indicate significant differences between the two agents. R[36] (Version 1.2.5001, R-Development-Core-Team, 2019) was used to create the graphics.

Time	Region	CA difference	t	P
14 days	Central	.40	1.30	1.00
	Margin	**1.86**	6.01	**<.001**
	Peritumoral	**1.01**	3.25	**.030**
	Liver	.28	.91	1.00
	Muscle	.26	.826	1.00
21 days	Central	**1.44**	3.23	**.034**
	Margin	**1.68**	3.67	**.007**
	Peritumoral	1.18	3.77	.168
	Liver	.18	.41	1.00
	Muscle	.29	.66	1.00
28 days	Central	**1.75**	5.67	**<.001**
	Margin	**1.81**	5.85	**<.001**
	Peritumoral	**1.18**	3.83	**.005**
	Liver	.03	.09	1.00
	Muscle	.19	.60	1.00

Table 1. Differences in relative enhancement (RE) between the enhancement of the elastin-specific probe and gadobutrol. Positive difference values indicate an advantage of the elastin-specific probe. CA contrast agent. Bold print: significant differences ($P \leq .05$).

	Gadobutrol				
	Central	**Margin**	**Peritumoral**	**Liver**	**Muscle**
Central	**1.52*****	− .59*	− .08	.13	.35
Margin	− 1.24*****	**2.43*****	.51	.71**	.93**
Peritumoral	− .04	1.20*****	**1.58*****	.20	.42
Liver	1.12*****	2.36*****	1.16*****	**.90*****	.22
Muscle	1.26*****	2.50*****	1.30*****	− .14	**.72****
	Elastin-specific probe				

Table 2. Differentiability of the regions based on the relative enhancement (RE) after application of gadobutrol (upper right section) and the elastin-specific probe (lower left section) together for all examination time points. Diagonal (bold print): strength of region discrimination (Bonferroni-corrected) using the elastin-specific probe compared to gadobutrol. Upper section: crude differences in gadobutrol RE between regions (central, margin, peritumoral, liver, muscle). Lower section: crude differences in elastin-specific RE between regions (central, margin, peritumoral, liver, muscle). *$P<.05$; **$P<.01$; ***$P<.001$.
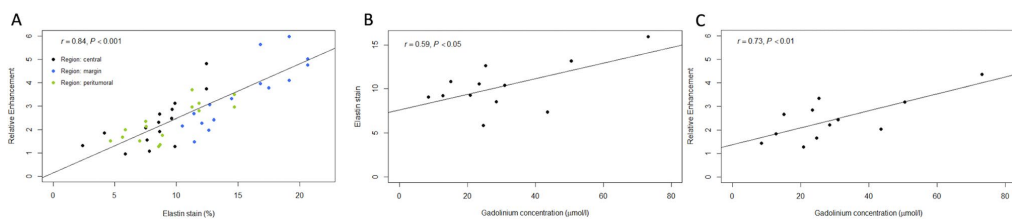
Figure 3. Associations of in vivo MR RE and ex vivo histological and mass spectrometry quantification of elastin in the tumor regions. (**A**) Correlation of in vivo RE and ex vivo quantification of the elastin stain area on cryosections. The RE of elastin probe measurements significantly correlates (R = 0.84, $P<0.001$) with the histopathological expression of elastic fibers (elastin stain) in the three tumor regions. (**B**) Linear regression shows a significant correlation between the elastin stain and the ICP-MS gadolinium concentration (μmol/l) of the whole tumor (R = 0.59; $P<0.05$). (**C**) Linear regression shows a significant correlation of the RE and gadolinium concentration (μmol/l) (R = 0.73; $P<0.01$). This indicates a close association between the amount of in vivo binding of the elastin-specific molecular probe and the overall gadolinium detected in tissue. R[36] (Version 1.2.5001, R-Development-Core-Team, 2019) was used to create the graphics.

nificant at all time points ($P=1.00$). Taken together for all time points, the RE using the elastin-specific probe differed significantly between the tumor regions ($\chi^2(4)=65.87$, $P<0.001$). In detail, there were significant differences in the RE of the elastin-specific probe between the tumor center and margin (difference − 1.24; $P<0.001$), the tumor margin and the peritumoral region (difference 1.20, $P<0.001$) and the peritumoral region and the liver parenchyma (difference 1.16, $P<0.001$) (Table 2). In contrast, the RE of gadobutrol was more unspecific and only distinguished between central and margin (difference − 0.59; $P<0.05$) and between margin and liver (difference 0.71; $P<0.01$). The difference in RE between margin and peritumoral tissue and between peritumoral and liver parenchyma was not significant (difference 0.51; $P=0.065$ and difference 0.20; $P=1.00$, respectively).

Histopathology. Viable tumors were found in all animals. Tumor regions were visualized on H&E and EvG stained sections and corresponded to the respective slight on the acquired MR images (Fig. 1). The in vivo RE measurements of the three tumor areas correlated significantly to the ex vivo EvG stain area measurements (R = 0.84, $P<0.001$) (Fig. 3A).

ICP-MS. The average concentration of gadolinium in the whole tumor was quantified using ICP-MS. The ICP-MS gadolinium concentration (μmol/l) of the whole tumor correlated significantly to histopathological elastin area stains (%) (R = 0.59; $P<0.05$) and the elastin-specific MR-based RE (R = 0.73; $P<0.01$) (Fig. 3B,C).

LA-ICP-MS. The gadolinium distribution was determined by LA-ICP-MS within the three regions and the surrounding liver parenchyma following the in vivo elastin-specific MRI on the second day. The colocalization of the gadolinium-bound elastin-specific probe with elastic fibers was pronounced in the tumor margin and the peritumoral region and corresponded to increased zinc distribution. The spatial distribution of P, Zn and Gd in the samples were not specifically distributed within the samples (Fig. 4).

4

63
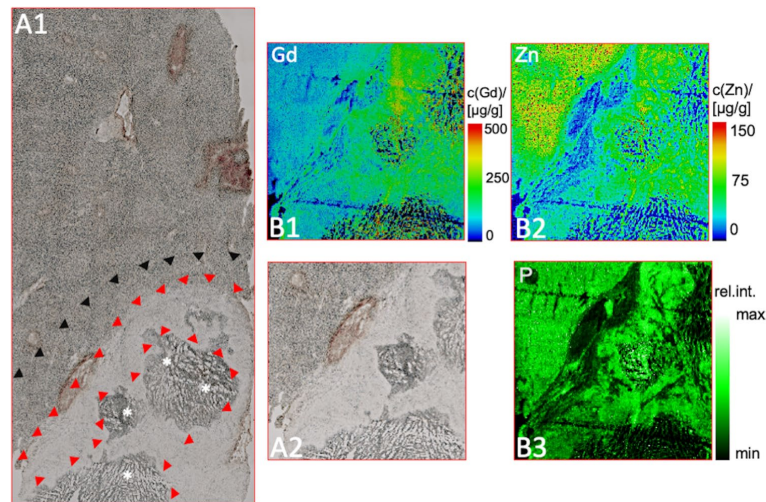
Figure 4. LA-ICP-MS for the assessment of the gadolinium distribution in the tumor areas. (**A1**, **A2**) Unstained cryosection for anatomical matching of the tumor (**A2** magnification). The arrowheads mark the tumor margin (red) and the peritumoral region (black). The asterisks (*) highlight the central zone. (**B1**) Specific gadolinium distribution of the magnified area (A2) confirms gadolinium in all tumor regions, predominantly in the tumor margin (green signal). (**B2**, **B3**) Control measurements regarding zinc (Zn) and phosphorous (P) do not show a specific distribution inside the tumor.

Discussion

The major finding of this study is that molecular MR imaging using the elastin-specific probe enables the discrimination of the different tumor regions and the peritumoral matrix with a higher accuracy compared to conventional gadolinium-based contrast agents in VX2 hepatic tumors. Mass spectroscopic and histopathological quantification of elastin accurately confirmed imaging-derived increases in elastin-specific contrast enhancement on MRI especially in the tumor margins. The concise differentiation of the tumor center, margin and immediate peritumoral space addresses an unmet clinical need for a non-invasive imaging protocol to detect metabolic alterations and assess therapy responsiveness. The imaging findings of the current study have been correlated to different modalities of ex vivo MS- and histopathology-based quantification techniques, thus providing a ground truth validation for the in vivo measurements. Therefore, this finding may improve the standard imaging protocol of treatment studies in experimentally induced hepatic cancer models in the future and potentially in patients.

Three tumor-associated regions were differentiated to address the variability of cells and ECM and thus the varying responsiveness to therapeutic agents and interventional studies. Whereas the central tumor region is mainly composed of necrotic and inactive cells, viable cells within the tumor margin contribute to tumor growth and progression. These cells interact within an elastic extracellular microenvironment, that provides not only chemical signals but also physical stimuli through stiffness[26,27]. The peritumoral matrix including fibroblasts, inflammatory cells, lymphatic vascular networks and different collagens as well as elastic fibers, has long been thought of as a stromal barrier to contain tumor progression by regulating various anti-cancer pathways. However, it has been shown that once transformed into a tumor-associated neighborhood by various stimuli, the stromal-derived effects can actively contribute to the tumor aggressiveness and responsiveness to anti-tumor therapies[2,28]. In a recently published US- based study the application of US microbubbles of different intensity and the response of the interstitial fluid pressure in the ECM was investigated[14]. It can be anticipated that more therapeutic studies will focus on the ECM tumor component in the future.

Few studies aimed to prove the linkage between the elastic ECM and peritumoral matrix, tumorigenesis and tumor progression. Yasui et al.[10] confirmed the predictive role of increased elastin fiber accumulation within the hepatic ECM for the development of HCC in patients. Maehara et al.[29] examined histopathological specimens of explanted human HCC and observed increased elastin and elastin-collagen components within the tumors. Moreover, increased elastin levels were associated with increased inflammatory cell infiltration, smaller capsule formation, and higher percentage of scirrhous stroma[29]. Their ratio of elastin to collagen was significantly higher in the tumor fibrous capsule ($P < 0.007$). However, whereas iodine-based contrast-enhanced CT correlated to the tumor collagen content, it failed to specifically detect elastic fibers. The finding of Maehara et al.[29] corresponds to our study results that conventional GBCAs are inferior to the elastin-specific MR agent in terms of elastin in tissue. Non-invasive MR imaging using the elastin-specific molecular probe produced image data with a high spatial resolution and clear contrast enhancement in the viable tumor regions, thus underlining the priority of targeted MRI in hepatic cancer research. Especially in the area of targeted therapies of tumor associated ECM

64
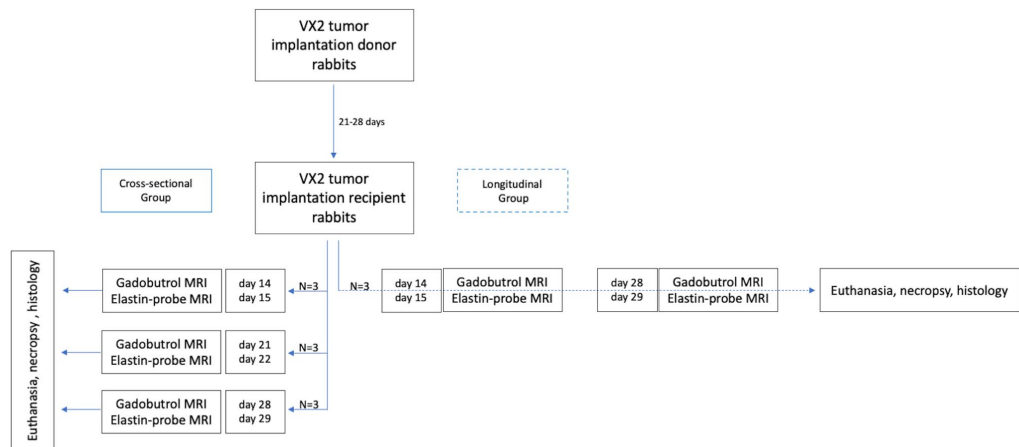
Figure 5. Experimental in vivo study design. In the vertical direction, the flow chart illustrates the VX2 rabbit tumor model and multimodal imaging on sequential time points. Left column: groups of three tumor-bearing rabbits were assigned to one MRI time point (day 14 + 15, 21 + 22, and 28 + 29 after tumor implantation) and euthanized following the scan. Right column: a group of three rabbits was assigned to two longitudinal MRI scans at each time point (14 + 15 and 28 + 29 days) and euthanized following the scan at time point 29.

components or cancer to stroma signaling cross-talks, such as sorafenib and erlotinib, elastin-specific molecular imaging could act as a potential imaging biomarker to demonstrate the tumor responsiveness to the therapeutic agent.

Some limitations of this study have to be acknowledged. Firstly, the study cohort consisting of N = 9 cross-sectional and N = 3 longitudinal rabbits was relatively small but comparable to previously published research in this area[30–32]. Secondly, the MRI was performed in free breathing, but under deep sedation which considerably reduces breathing motion. Thirdly, even though we observed a clear pattern of elastin-specific contrast agent accumulation within the tumor regions, a longitudinal effect on the specific enhancement patterns was not observed, indicating that tumor remodeling with regards to elastic fibers does not seem to take place in untreated settings within the first four weeks following tumor implantation. The missing tumor remodeling could be used on the other hand to use the available data as a baseline imaging component for longitudinal studies with longer time frames.

In conclusion, our data confirm the diagnostic potential of the elastin-specific targeted MRI for imaging and quantitative assessment of the intra- and peritumoral matrix in a hepatic cancer animal model. Molecular MRI using the elastin-specific probe enables the discrimination of the different tumor regions and the peritumoral matrix with a higher accuracy compared to conventional gadolinium-based contrast agents in VX2 hepatic tumors. This technique might be useful to assess systemic and local treatment effects in future experimental and clinical studies.

Materials and methods

Animal model.   All experimental protocols were performed according to the guidelines and regulations of the Federation of Laboratory Animal Science Associations (FELASA) and the local Guidelines and Provisions for Implementation of the Animal Welfare Act, as approved by the Regional Office for Health and Social Affairs Berlin (LAGeSo) (registration number 0178/17). Twelve female New Zealand white rabbits (Charles River Laboratories, Sulzfeld, Germany) aged 11–17 weeks, mean weight (standard deviation) 3.2 ± 0.3 kg were used for this experimental study. VX2 cells were injected into the hindlimb muscles of six female donor rabbits and grown for 21–30 days to a size of 1.5–2.0 cm as previously described[33]. Harvested chunks were minced and implanted into the left liver lobe by mini laparotomy into the receiver rabbits (N = 12). Anesthesia was performed using intravenous injections of Buprenorphin (Temgesic, 0.03 mg/kg body weight) and subcutaneous injections of medetomidine hydrochloride (Cepetor, 0.25 mg/kg body weight), and ketamine hydrochloride (Ketamin, 30 mg/kg body weight). Carprofen (Rimadyl, 4.0 mg/kg body weight) was injected as an analgesic for the following three days after all surgical procedures.

According to the study protocol (Fig. 5), the rabbits were randomized into four groups following tumor implantation. Three cross-sectional groups with N = 3 rabbits each received an MRI scan 14 + 15, 21 + 22, or 28 + 29 days after tumor implantation immediately followed by euthanasia using intravenous injection of pentobarbital sodium (Narcoren, 300 mg/kg body weight), and necropsy. A longitudinal group with N = 3 tumor bearing rabbits was additionally imaged 14 + 15 and 28 + 29 days after tumor implantation and euthanized on day 29.

65

Gadolinium-based elastin probe. The elastin-specific molecular agent (ESMA; Lantheus Medical Imaging, North Billerica, MA) is composed of the D-amino-acid homophenylalanine, which is coupled by a rigid hydrazine aminomethylbenzoic acid linker to a gadolinium-diethylenetriaminepentaacetic acid complex[22]. Ex vivo measurements obtained a longitudinal relaxivity for the agent bound to mice aortas of 8.65 ± 0.42 mmol/ l^{-1} s^{-1} at 3 T[22]. In this study, a clinical dose of 0.2 mmol/kg was used and administered as a bolus via the ear vein.

MR imaging. MRI was performed under deep sedation using a 3 T clinical scanner (mMR Biograph, Siemens Medical Solutions, Erlangen, Germany). The rabbits were imaged in prone position using a clinically approved head-neck coil. Each rabbit was scanned on two consecutive days. Animals received an intravenous injection of gadobutrol (Gadovist 1.0 mmol/ml, Bayer Healthcare AG, Berlin) 0.2 mmol/kg on the first day. On the second day an elastin-specific gadolinium-based probe was administered at 0.2 mmol/kg. Anatomic images were acquired using a T2-weighted (TR/TE 5500/90 ms, FOV 180×180 mm², voxel size $0.5 \times 0.5 \times 1.0$ mm³, NSA 3) and a clinically approved three-dimensional (3D) gradient-recalled-echo (GRE) sequence, which is routinely applied as a standard sequence for liver imaging and liver tumor detection[34] (T1 volumetric interpolated breath-hold examination (VIBE), TR/TE 5.0/2.18 ms, FOV 180×180 mm², voxel size $0.7 \times 0.7 \times 1.0$ mm³, NSA 2), before and 20 min after injection of the contrast agent. The T1 VIBE sequence allows improved MR imaging by providing dynamic contrast–enhanced thin-section images with fat saturation and a high signal-to-noise ratio[35]. Additional pre-contrast scans were performed for each animal on the second day prior to injection of the elastin-specific probe to detect any residual retention of gadobutrol in the liver of the animals.

Image postprocessing. MR images were analyzed by two radiologists in consensus using HOROS (v 4.0.0.0RC1; Nimble Co LLC d/b/a Purview in Annapolis, MD USA; https://horosproject.org). Tumors were manually segmented into a central and marginal region. Additional regions of interest (ROIs) covered the peritumoral matrix, normal liver parenchyma and the back muscles of the same slight. The central area also covered the tumor necrosis, the marginal area included microscopically densely packed the "vital" tumor cells and the tumor fibrous capsule.

The relative enhancement (RE) was assessed using the following formula:

$$RE = \frac{(SI_{postcontrast} - SI_{precontrast})}{SI_{precontrast}}. \tag{1}$$

Histology. Following the MRI scan, liver tumors were explanted and immediately frozen at $-80\,°C$. 10 µm cryosections mounted on adhesion slides (SuperFrost Plus, Thermo Scientific) were stained with Miller's elastic van Gieson histochemical stain (EvG) and hematoxylin and eosin stain (H&E) to visualize the tumor, ECM and elastic fibers. A light microscope (BzX800, Keyence, Japan) was used for examination of the slides. Digitalized images (TIFF file format) were stored for computer-assisted image analysis (ImageJ software, version 1.51, Wayne Rasband, National Institutes of Health; https://imagej.nih.gov/ij/). To measure the %EvG stain area per region all structures within the specific color profile were automatically segmented. By dividing the segmented area by the respective region (e.g. peritumoral), the %EvG stain area was determined.

Laser ablation-inductively coupled plasma-mass spectrometry (LA-ICP-MS) for elemental bioimaging. The LA-ICP-MS analysis for quantitative imaging of gadolinium (Gd), iron (Fe), zinc (Zn), and phosphor (P) was conducted as previously described[24]. Due to the different sample composition, a scan speed of 45 µm/s with unchanged 800 ml/min helium (He) as transport gas was used in this analysis. In this analysis the averaged intensities of the scanned lines of the standards demonstrated a linear correlation with a $R^2 = 0.996$ over the concentration range. The limit of detection (LOD) and limit of quantification (LOQ) were calculated using 3σ- and 10σ-criteria and were as follows: 12 ng/g and 40 ng/g for Gd, 5.9 µg/g and 20 µg/g for Fe and 2.0 µg/g and 6.6 µg/g for Zn, respectively.

Inductively coupled plasma mass spectroscopy (ICP-MS). For the ICP-MS analysis, samples were digested in 70% nitric acid at 37 °C overnight immediately after the last imaging session, followed by dilution with deionized water for ICP-MS analysis. A standard curve was acquired with each sample set for gadolinium concentration determination.

Statistical analysis. The statistical software 'R'[36] (Version 1.2.5001, R-Development-Core-Team, 2019) with the package lmerTest providing mixed model methods[37] was used for statistical analysis. First, we used analyses of variance (ANOVAs) for each time point separately to analyze the cross-sectional part of the data. Additionally, we applied Bonferroni corrected t-tests to compare the differences between both agents for all regions and time points. Second, we applied a mixed model to account for the cross-sectional and longitudinal combined study design with planned missings. RE was the dependent variable. Time latency (14, 21, or 28 days), region (central, margin, peritumoral, liver, and muscle), and the agent (gadobutrol or elastin-specific probe), as well as their interactions, were the independent variables. To display the overall effect of a variable, we used likelihood ratio tests; the effects of specific variable stages were assessed with t-tests following Satterthwaite's method[38].

Ethics approval and consent to participate. According to ARRIVE guidelines this study was approved by the local guidelines and provisions for the implementation of the Animal Welfare Act and regulations of the Federation of Laboratory Animal Science Associations (FELASA; registration number 0178/17).

Data availability
The datasets used and/or analyzed during the current study are available from the corresponding author on reasonable request.

References

1. Jindal, A., Thadi, A. & Shailubhai, K. Hepatocellular carcinoma: etiology and current and future drugs. *J. Clin. Exp. Hepatol.* **9**, 221–232. https://doi.org/10.1016/j.jceh.2019.01.004 (2019).
2. Carloni, V., Luong, T. V. & Rombouts, K. Hepatic stellate cells and extracellular matrix in hepatocellular carcinoma: more complicated than ever. *Liver Int.* **34**, 834–843. https://doi.org/10.1111/liv.12465 (2014).
3. Sherman-Baust, C. A. *et al.* Remodeling of the extracellular matrix through overexpression of collagen VI contributes to cisplatin resistance in ovarian cancer cells. *Cancer Cell* **3**, 377–386. https://doi.org/10.1016/s1535-6108(03)00058-8 (2003).
4. Sethi, T. *et al.* Extracellular matrix proteins protect small cell lung cancer cells against apoptosis: a mechanism for small cell lung cancer growth and drug resistance in vivo. *Nat. Med.* **5**, 662–668. https://doi.org/10.1038/9511 (1999).
5. Ma, H. P. *et al.* Collagen 1A1 (COL1A1) is a reliable biomarker and putative therapeutic target for hepatocellular carcinogenesis and metastasis. *Cancers (Basel).* https://doi.org/10.3390/cancers11060786 (2019).
6. Salarian, M. *et al.* Precision detection of liver metastasis by collagen-targeted protein MRI contrast agent. *Biomaterials* **224**, 119478. https://doi.org/10.1016/j.biomaterials.2019.119478 (2019).
7. Fang, M., Yuan, J., Peng, C. & Li, Y. Collagen as a double-edged sword in tumor progression. *Tumour Biol.* **35**, 2871–2882. https://doi.org/10.1007/s13277-013-1511-7 (2014).
8. Levental, K. R. *et al.* Matrix crosslinking forces tumor progression by enhancing integrin signaling. *Cell* **139**, 891–906. https://doi.org/10.1016/j.cell.2009.10.027 (2009).
9. Lu, P., Weaver, V. M. & Werb, Z. The extracellular matrix: a dynamic niche in cancer progression. *J. Cell Biol.* **196**, 395–406. https://doi.org/10.1083/jcb.201102147 (2012).
10. Yasui, Y. *et al.* Elastin fiber accumulation in liver correlates with the development of hepatocellular carcinoma. *PLoS ONE* **11**, e0154558. https://doi.org/10.1371/journal.pone.0154558 (2016).
11. Jiang, T., Zhang, X., Ding, J., Duan, B. & Lu, S. Inflammation and cancer: inhibiting the progression of residual hepatic VX2 carcinoma by anti-inflammatory drug after incomplete radiofrequency ablation. *Int. J. Clin. Exp. Pathol.* **8**, 13945–13956 (2015).
12. Zhou, C. *et al.* Combining transcatheter arterial embolization with iodized oil containing Apatinib inhibits HCC growth and metastasis. *Sci. Rep.* **10**, 2964. https://doi.org/10.1038/s41598-020-59746-1 (2020).
13. Kong, W. T. *et al.* Early treatment response to sorafenib for rabbit VX2 orthotic liver tumors: evaluation by quantitative contrast-enhanced ultrasound. *Tumour Biol.* **36**, 2593–2599. https://doi.org/10.1007/s13277-014-2877-x (2015).
14. Zhang, Q. *et al.* Effect of ultrasound combined with microbubble therapy on interstitial fluid pressure and VX2 tumor structure in rabbit. *Front. Pharmacol.* **10**, 716. https://doi.org/10.3389/fphar.2019.00716 (2019).
15. Liu, X. *et al.* Brachytherapy using elastin-like polypeptides with (131)I inhibit tumor growth in rabbits with VX2 liver tumor. *Dig. Dis. Sci.* **61**, 2921–2927. https://doi.org/10.1007/s10620-016-4212-4 (2016).
16. Staks, T. *et al.* Pharmacokinetics, dose proportionality, and tolerability of gadobutrol after single intravenous injection in healthy volunteers. *Invest. Radiol.* **29**, 709–715. https://doi.org/10.1097/00004424-199407000-00008 (1994).
17. Kawai, J., Takahashi, M., Kato, N., Takashima, K. & Miyazawa, T. Comparison of a 1.0 molar and a 0.5 molar formulation of gadobutrol in dynamic MR imaging of the liver in rats with hepatocellular carcinoma. *Magn. Reson. Imaging* **17**, 91–97. https://doi.org/10.1016/s0730-725x(98)00144-1 (1999).
18. Tombach, B. & Heindel, W. Value of 10-M gadolinium chelates: review of preclinical and clinical data on gadobutrol. *Eur. Radiol.* **12**, 1550–1556. https://doi.org/10.1007/s00330-001-1242-9 (2002).
19. Kim, Y. K., Lee, Y. H., Kim, C. S., Han, Y. M. & Hwang, S. B. Double-dose 1.0-M gadobutrol versus standard-dose 0.5-M gadopentetate dimeglumine in revealing small hypervascular hepatocellular carcinomas. *Eur. Radiol.* **18**, 70–77. https://doi.org/10.1007/s00330-007-0630-1 (2008).
20. Chang, J. M. *et al.* Dynamic contrast-enhanced magnetic resonance imaging evaluation of VX2 carcinoma in a rabbit model: comparison of 1.0-M gadobutrol and 0.5-M gadopentetate dimeglumine. *Invest. Radiol.* **45**, 655–661. https://doi.org/10.1097/RLI.0b013e3181ed55b4 (2010).
21. Schelhorn, J. *et al.* Evaluation of combined Gd-EOB-DTPA and gadobutrol magnetic resonance imaging for the prediction of hepatocellular carcinoma grading. *Acta Radiol.* **57**, 932–938. https://doi.org/10.1177/0284185115616293 (2016).
22. Makowski, M. R. *et al.* Assessment of atherosclerotic plaque burden with an elastin-specific magnetic resonance contrast agent. *Nat. Med.* **17**, 383–388. https://doi.org/10.1038/nm.2310 (2011).
23. Botnar, R. M. *et al.* In vivo assessment of aortic aneurysm wall integrity using elastin-specific molecular magnetic resonance imaging. *Circ. Cardiovasc. Imaging* **7**, 679–689. https://doi.org/10.1161/CIRCIMAGING.113.001131 (2014).
24. Brangsch, J. *et al.* Concurrent molecular magnetic resonance imaging of inflammatory activity and extracellular matrix degradation for the prediction of aneurysm rupture. *Circ. Cardiovasc. Imaging* **12**, e008707. https://doi.org/10.1161/CIRCIMAGING.118.008707 (2019).
25. Okamura, H. *et al.* Assessment of elastin deficit in a Marfan mouse aneurysm model using an elastin-specific magnetic resonance imaging contrast agent. *Circ. Cardiovasc. Imaging* **7**, 690–696. https://doi.org/10.1161/CIRCIMAGING.114.001658 (2014).
26. Ng, M. R. & Brugge, J. S. A stiff blow from the stroma: collagen crosslinking drives tumor progression. *Cancer Cell* **16**, 455–457. https://doi.org/10.1016/j.ccr.2009.11.013 (2009).
27. Engler, A. J., Sen, S., Sweeney, H. L. & Discher, D. E. Matrix elasticity directs stem cell lineage specification. *Cell* **126**, 677–689. https://doi.org/10.1016/j.cell.2006.06.044 (2006).
28. Chen, F. *et al.* New horizons in tumor microenvironment biology: challenges and opportunities. *BMC Med.* **13**, 45. https://doi.org/10.1186/s12916-015-0278-7 (2015).
29. Maehara, J. *et al.* Quantification of intratumoral collagen and elastin fibers within hepatocellular carcinoma tissues finds correlations with clinico-patho-radiological features. *Hepatol. Res.* https://doi.org/10.1111/hepr.13484 (2019).
30. Vossen, J. A. *et al.* Diffusion-weighted and Gd-EOB-DTPA-contrast-enhanced magnetic resonance imaging for characterization of tumor necrosis in an animal model. *J. Comput. Assist. Tomogr.* **33**, 626–630. https://doi.org/10.1097/RCT.0b013e3181953df3 (2009).

67

31. Wang, D. *et al.* Four-dimensional transcatheter intraarterial perfusion (TRIP)-MRI for monitoring liver tumor embolization in VX2 rabbits. *Magn. Reson. Med.* **60**, 970–975. https://doi.org/10.1002/mrm.21678 (2008).
32. Moon, J. *et al.* Correlation of quantitative dynamic contrast-enhanced MRI with microvascular density in necrotic, partial necrotic, and viable liver tumors in a rabbit model. *J. Appl. Clin. Med. Phys.* **17**, 418–427. https://doi.org/10.1120/jacmp.v17i5.6314 (2016).
33. Geschwind, J. F. *et al.* Chemoembolization of liver tumor in a rabbit model: assessment of tumor cell death with diffusion-weighted MR imaging and histologic analysis. *J. Vasc. Interv. Radiol.* **11**, 1245–1255 (2000).
34. Elsayes, K. M. *et al.* Focal hepatic lesions: diagnostic value of enhancement pattern approach with contrast-enhanced 3D gradient-echo MR imaging. *Radiographics* **25**, 1299–1320. https://doi.org/10.1148/rg.255045180 (2005).
35. Rofsky, N. M. *et al.* Abdominal MR imaging with a volumetric interpolated breath-hold examination. *Radiology* **212**, 876–884. https://doi.org/10.1148/radiology.212.3.r99se34876 (1999).
36. *R: A Language and Environment for Statistical Computing* (R Foundation for Statistical Computing, Vienna, Austria, 2019).
37. Kuznetsova, A., Brockhoff, P. B. & Christensen, R. H. B. lmerTest package: tests in linear mixed effects models. **82**, 26. https://doi.org/10.18637/jss.v082.i13 (2017).
38. Satterthwaite, F. E. An approximate distribution of estimates of variance components. *Biometrics* **2**, 110–114 (1946).

Author contributions

Funding

Competing interests

The authors declare no competing interests.

Additional information

Correspondence and requests for materials should be addressed to S.K.

Reprints and permissions information is available at www.nature.com/reprints.

Publisher's note Springer Nature remains neutral with regard to jurisdictional claims in published maps and institutional affiliations.

Selected Category: "MEDICINE, RESEARCH and EXPERIMENTAL":

Keller S, Borde T, Brangsch J, Adams LC, Kader A, Reimann C, Gebert P, Hamm B, Makowski M. Native T1 Mapping Magnetic Resonance Imaging as a Quantitative Biomarker for Characterization of the Extracellular Matrix in a Rabbit Hepatic Cancer Model. Biomedicines. 2020 Oct 13;8(10):412.

Publication received: 12 August 2020

Journal Data Filtered By: **Selected JCR Year: 2019** Selected Editions: SCIE,SSCI
Selected Categories: **"MEDICINE, RESEARCH and EXPERIMENTAL"**
Selected Category Scheme: WoS
Gesamtanzahl: 138 Journale

Rank	Full Journal Title	Total Cites	Journal Impact Factor	Eigenfactor Score
1	NATURE MEDICINE	85,220	36.130	0.168730
2	Science Translational Medicine	34,479	16.304	0.116030
3	JOURNAL OF CLINICAL INVESTIGATION	109,020	11.864	0.125830
4	JOURNAL OF EXPERIMENTAL MEDICINE	63,562	11.743	0.067350
5	TRENDS IN MOLECULAR MEDICINE	10,618	11.099	0.018720
6	Annual Review of Medicine	6,267	9.716	0.009390
7	MOLECULAR ASPECTS OF MEDICINE	6,207	9.577	0.005750
8	MOLECULAR THERAPY	17,977	8.986	0.030980
9	EMBO Molecular Medicine	8,366	8.821	0.022770
10	Theranostics	12,995	8.579	0.029740
11	Clinical and Translational Medicine	1,349	7.919	0.003280
12	Wiley Interdisciplinary Reviews-Nanomedicine and Nanobiotechnology	2,819	7.689	0.004240
13	Molecular Therapy-Nucleic Acids	5,024	7.032	0.013550
14	JCI Insight	7,697	6.205	0.034400
15	Cold Spring Harbor Perspectives in Medicine	7,647	6.000	0.016800
16	ALTEX-Alternatives to Animal Experimentation	1,413	5.787	0.002210
17	JOURNAL OF BIOMEDICAL SCIENCE	4,499	5.762	0.006380
18	EBioMedicine	8,133	5.736	0.029330
19	npj Vaccines	596	5.699	0.002400
20	Cancer Biology & Medicine	1,389	5.432	0.003640

Selected JCR Year: 2019; Selected Categories: "MEDICINE, RESEARCH and EXPERIMENTAL"

Rank	Full Journal Title	Total Cites	Journal Impact Factor	Eigenfactor Score
21	EXPERIMENTAL AND MOLECULAR MEDICINE	5,536	5.418	0.010300
22	Translational Research	4,043	5.411	0.008350
23	Stem Cell Reviews and Reports	2,737	5.316	0.004100
24	CLINICAL SCIENCE	11,443	5.223	0.013850
25	Nanomedicine-Nanotechnology Biology and Medicine	11,123	5.182	0.014400
26	Stem Cell Research & Therapy	8,268	5.116	0.017170
27	EPMA Journal	987	4.901	0.001110
28	Nucleic Acid Therapeutics	1,030	4.875	0.003610
29	Biomarker Research	768	4.866	0.002100
30	Biomedicines	1,156	4.717	0.002850
31	mAbs	4,906	4.634	0.011110
32	BIOMEDICINE & PHARMACOTHERAPY	25,449	4.545	0.041300
33	CANCER GENE THERAPY	2,914	4.534	0.002860
34	Molecular Therapy-Methods & Clinical Development	1,686	4.533	0.006820
35	JOURNAL OF CELLULAR AND MOLECULAR MEDICINE	14,713	4.486	0.018920
36	JOURNAL OF MOLECULAR MEDICINE-JMM	7,543	4.427	0.009210
37	AMYLOID-JOURNAL OF PROTEIN FOLDING DISORDERS	1,486	4.323	0.002920
38	MOLECULAR PHARMACEUTICS	18,599	4.321	0.026080
39	Wiley Interdisciplinary Reviews-Systems Biology and Medicine	1,230	4.275	0.002180
40	HUMAN GENE THERAPY	5,631	4.273	0.008140
41	CYTOTHERAPY	6,557	4.218	0.008100

Selected JCR Year: 2019; Selected Categories: "MEDICINE, RESEARCH and EXPERIMENTAL"

biomedicines

MDPI

Native T1 Mapping Magnetic Resonance Imaging as a Quantitative Biomarker for Characterization of the Extracellular Matrix in a Rabbit Hepatic Cancer Model

Sarah Keller [1],* , **Tabea Borde [1,2]**, **Julia Brangsch [1]**, **Lisa C. Adams [1]**, **Avan Kader [1]** , **Carolin Reimann [1]**, **Pimrapat Gebert [3]**, **Bernd Hamm [1]** and **Marcus Makowski [1,2]**

[1] Department of Radiology, Charité—Universitätsmedizin Berlin, Corporate Member of Freie Universität Berlin, Humboldt-Universität zu Berlin, and Berlin Institute of Health, Charitéplatz 1, 10117 Berlin, Germany; tb.borde@gmail.com (T.B.); julia.brangsch@charite.de (J.B.); Lisa.adams@charite.de (L.C.A.); avan.kader@charite.de (A.K.); carolin.reimann@charite.de (C.R.); bernd.hamm@charite.de (B.H.); marcus.makowski@tum.de (M.M.)

[2] Department of Diagnostic and Interventional Radiology, School of Medicine & Klinikum Rechts der Isar, Technical University of Munich, Munich (TUM), Ismaninger Str. 22, 81675 München, Germany

[3] Department of Biometry and Epidemiology, Charité—Universitätsmedizin Berlin, Corporate Member of Freie Universität Berlin, Humboldt-Universität zu Berlin, and Berlin Institute of Health, Charitéplatz 1, 10117 Berlin, Germany; pimrapat.gebert@charite.de

* Correspondence: sarah.keller@charite.de; Tel.: +49-(0)-30-450-627-145

check for updates

Abstract: To characterize the tumor extracellular matrix (ECM) using native T1 mapping magnetic resonance imaging (MRI) in an experimental hepatic cancer model, a total of 27 female New Zealand white rabbits with hepatic VX2 tumors were examined by MRI at different time points following tumor implantation (day 14, 21, 28). A steady-state precession readout single-shot MOLLI sequence was acquired in a 3 T MRI scanner in prone position using a head-neck coil. The tumors were segmented into a central, marginal, and peritumoral region in anatomical images and color-coded T1 maps. In histopathological sections, stained with H&E and Picrosirius red, the regions corresponded to central tumor necrosis and accumulation of viable cells with fibrosis in the tumor periphery. Another region of interest (ROI) was placed in healthy liver tissue. T1 times were correlated with quantitative data of collagen area staining. A two-way repeated-measures ANOVA was used to compare cohorts and tumor regions. Hepatic tumors were successfully induced in all rabbits. T1 mapping demonstrated significant differences between the different tumor regions ($F(1.43,34.26) = 106.93$, $p < 0.001$) without interaction effects between time points and regions ($F(2.86,34.26) = 0.74$, $p = 0.53$). In vivo T1 times significantly correlated with ex vivo collagen stains (area %), (center: r = 0.78, $p < 0.001$; margin: r = 0.84, $p < 0.001$; peritumoral: r = 0.73, $p < 0.001$). Post hoc tests using Sidak's correction revealed significant differences in T1 times between all three regions ($p < 0.001$). Native T1 mapping is feasible and allows the differentiation of tumor regions based on ECM composition in a longitudinal tumor study in an experimental small animal model, making it a potential quantitative biomarker of ECM remodeling and a promising technique for future treatment studies.

Keywords: magnetic resonance imaging; extracellular matrix; liver cancer; rabbits; VX2; T1 mapping

1. Introduction

The extracellular matrix (ECM) is a major component of tumoral stroma and has attracted much attention as a key regulator of cell and tissue function [1,2]. For a long time regarded as a mere mechanical link between cells, the ECM has since been shown to influence tissue migration, adhesiolysis,

and repair through the regulation of biochemical and biophysical pathways [3,4]. While the production and degradation of proteins as a major component of the ECM are strictly balanced in healthy tissue, these processes often become dysregulated in cancer [5,6]. More specifically, the upregulation of collagen as the most abundant ECM component appears to play a prominent role in the tumor activating orchestra. For primary [7,8] and secondary [1,9,10] liver cancers, it has been shown that collagen upregulation seems to play a substantial role in angiogenesis, tumor cell infiltration and thus sensitivity to anticancer agents.

In recent years, native (unenhanced) T1 mapping has developed into a useful, noninvasive imaging method to quantitatively characterize tissue properties. T1 mapping measures longitudinal T1 relaxation time in milliseconds, which primarily depends on the molecular microenvironment of water molecules in the tissue. As a result, various changes in the extracellular space, such as increased water content in edema [11,12], protein deposition [13], or increased collagen formation [14,15], for example in fibrosis, can be detected using native T1 mapping.

Therefore, remodeling of the ECM with increasing collagen accumulation can be quantified by T1 mapping. T1 mapping is most commonly performed using the modified look-locker inversion recovery sequence (MOLLI). In the myocardium, MOLLI-based T1 mapping has shown excellent diagnostic performance with regard to the detection of tissue changes in patients compared to controls. The strongest correlations were found between the histopathologically quantified collagen volume fraction and T2 mapping results as an indicator of edema [16]. Based on these capabilities, T1 mapping has been increasingly used for the diagnosis and differentiation of a variety of cardiac diseases such as myocardial fibrosis, myocardial infarction, or myocarditis [14,17,18], as well as systemic disorders such as amyloidosis and siderosis [13].

In the liver, native T1 mapping has been successfully applied as an imaging biomarker for the diagnosis and grading of fibrosis, and thus as a predictor of clinical outcome [19–21]. In experimentally induced liver fibrosis in a rabbit model [22], T1 mapping showed promising results in differentiating early and advanced liver fibrosis histopathologically classified by METAVIR [23]. However, despite its clinical practicability and its capability to reliably differentiate tissue alterations, only limited data are available on the potential of native T1 mapping for the detection and characterization of tumors. In a recent preclinical study, Zormpas-Petridis et al. found T1 mapping to reliably distinguish regions with different levels of tumor cell differentiation in an experimental mouse model of neuroblastoma [24]. In patients, native T1 mapping was successfully used to identify higher-grade renal cell carcinoma histologically validated by the collagen volume fraction [25]. However, to the best of our knowledge, there is as yet no preclinical or clinical study that has systematically investigated native T1 mapping sequences to characterize liver tumors in terms of ECM composition.

Therefore, the objective of this study was to assess native T1 mapping in a VX2 hepatic tumor rabbit model at different time points after tumor implantation. It was hypothesized (1) that due to its signaling characteristics, native T1 relaxation times are higher in the necrotic tumor center compared to the tumor margin and peritumoral tissue; (2) that native T1 mapping as a noninvasive, contrast-free tool reliably distinguishes tumor areas from normal liver tissue; and (3) that native T1 times correlate with collagen content in histopathological sections.
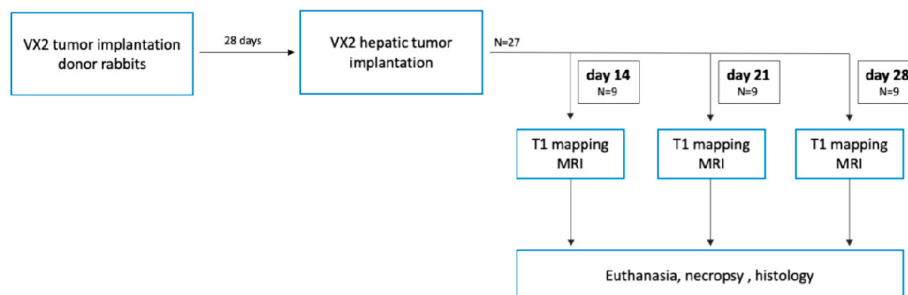
2. Experimental Section

2.1. Animal Model

This study was approved by the responsible authority and was conducted in accordance with local guidelines and provisions for the implementation of the Animal Welfare Act and regulations of the Federation of Laboratory Animal Science Associations (FELASA; registration number 0178/17; date 06/11/2017) and designed in accordance with the ARRIVE guidelines. The unenhanced magnetic resonance imaging (MRI) data used here were acquired as part of a larger study evaluating different contrast agents in the rabbit model. Twenty-seven female New Zealand white rabbits (Charles River

Laboratories, Sulzfeld, Germany) aged 11 to 17 weeks with a mean weight (standard deviation) of 3.3 (0.3) kilograms were used for this experimental study. All animals were maintained in laminar flow rooms at constant temperature and humidity, with food and water provided ad libitum. VX2 cells were injected in the hindlimb of eight female donor rabbits and grown for 21–30 days as previously described [26]. The tumors were harvested and processed; approximately 4 mL of the resulting tumor chunks were subsequently implanted into the left liver lobe of the recipient animals by mini laparotomy. Donor rabbits received a perioperative anesthesia of medetomidine hydrochloride (cepetor, 0.25 mg/kg), and ketamine hydrochloride (ketamin, 30 mg/kg) subcutaneously. Carprofen (rimadyl, 4.0 mg/kg) was injected as an analgesic for three days following surgery.

According to the study protocol (Figure 1), the rabbits were divided into three subgroups with N = 9 animals that were examined by MRI with T1 mapping on day 14, day 21, or day 28 after intrahepatic tumor implantation. Immediately after MRI, the rabbits were euthanized with pentobarbital sodium (Narcoren, 300 mg/kg body weight) under general anesthesia and necropsied. Tumor and liver parenchyma samples were collected and processed for histopathological analysis.

Figure 1. Experimental in vivo study design. In the vertical direction, the flow chart illustrates the VX2 rabbit tumor model and magnetic resonance imaging (MRI) on sequential time points. Groups of N = 9 tumor-bearing rabbits were assigned to one time point (day 14, 21, and 28 after implantation) and euthanized following the scan.

2.2. MR Imaging

MRI was performed in deep sedation in a 3 T clinical scanner (mMR Biograph, Siemens Medical Solutions, Erlangen, Germany). The rabbits were imaged in prone position with a clinically approved head-neck coil. Anatomic images were acquired using a T2-weighted (TR/TE 5500/90 ms, voxel size $0.5 \times 0.5 \times 3.0$ mm^3, FOV 180×180 mm^2) and T1-weighted Dixon sequence (TR/TE 4.76/1.49 ms, voxel size $0.5 \times 0.5 \times 2.0$ mm^3, FOV 272×272 mm^2) followed by a commercially available steady-state precession readout single-shot MOLLI sequence (TR/TE 1155/2.45 ms, voxel size $1.0 \times 1.0 \times 3.0$ mm^3, FOV 250×250 mm^2). The total scanning time was approximately 12 min. T1 maps were automatically computed on a pixel-by-pixel basis. The resulting pixel-by-pixel maps were displayed by use of a customized 12-bit lookup table, and the color map was visible immediately after data acquisition. In the color map, the signal intensity (SI) of each pixel reflects the absolute T1 value of the underlying value.

2.3. Image Postprocessing

Imaging datasets were evaluated with the open source software tool Horos (version 4.0.0.0RC1, Nimble Co LLC, Annapolis, MD, USA). Regions were manually segmented using the anatomical T1-weighted sequences in conjunction with T2-weighted images into a central, marginal, and peritumoral region.

According to preliminary studies [27,28], central necrosis has low T1 and low T2 signal intensity. Viable tumor tissue is characterized by slight T2 hyperintensity and can therefore be discriminated well from necrosis and surrounding peritumoral tissue [28] (Figure 2). The peritumoral region was

defined as an area around the tumor of approximately 2 mm. The respective ROI was then copied to the axial color-coded T1 map, using an automatic co-registration tool and by visual correlation in the case of breathing artifacts (Figure 2). In the respective histological hematoxylin and eosin (H&E) stains, the central region covered the tumor necrosis, while the marginal area included viable tumor cells and the fibrous tumor capsule. The peritumoral region covered the peritumoral matrix including hepatocytes, inflammatory cells, stromal cells, etc. ROIs placed in healthy liver tissue and the autochthonous back muscles of the same image plane served as controls.
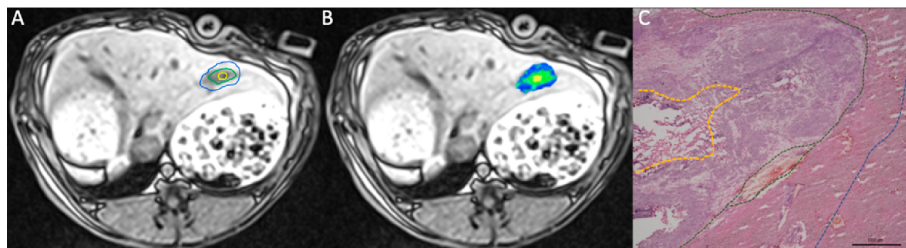
Figure 2. Schematic illustration of manually segmented tumor regions. (**A**) Axial T1-weighted images were used for delineation of the tumor center (yellow), margin (green), and the peritumoral region (blue). (**B**) Corresponding native MOLLI color-coded map depicting regional T1 times. (**C**) Corresponding segmentation in the histopathological H&E-stained sections.

2.4. Histology

Following MRI, liver tumors were harvested for necropsy. Liver tumors were explanted and immediately frozen at −80 °C. Tissues were embedded and stored using embedding medium for cryostat sectioning (Tissue-Tek, Sakura Finetek, Torrance, CA, USA), cut at −20 °C into 10 μm sections and mounted on adhesion slides (SuperFrost Plus, Thermo Scientific, Waltham, MA, USA). The sections were then stained with Picrosirius red stain and H&E to visualize collagen content and tumor composition. A light microscope (BzX800, Keyence, Japan) was used for the examination of the slides. Representative magnification (×2 and ×10) digitalized images (TIFF file format) were stored for computer-assisted image analysis using the open-access software ImageJ (ImageJ software, version 1.51, Wayne Rasband, National Institutes of Health; https://imagej.nih.gov/ij/, Bethesda, MD, USA). For image analysis of histologies, separate ROIs were drawn manually, as these deviated slightly due to the fixation process and therefore did not correlate with the MR images. The color profile of the corresponding region was automatically segmented. The percentage of collagen fibers per region was determined by dividing the percentage by the total area of the region.

2.5. Statistical Analysis

Since the end-points are semiquantitative in nature, a size of N = 9 was chosen as the balance between scientific necessity and resources available to perform the study in agreement with mandatory Animal Care and Use Committee limitations in USDA-restricted species, making it necessary to keep the numbers of animals used as low as reasonably achievable to meet study goals. All quantitative T1 mapping parameters (central, margin, peritumoral, liver) are expressed as mean and standard deviation (SD). Normal distribution was tested using normal QQ plots. Two-way repeated-measures ANOVA was performed to compare the change in T1 times between regions over time using Greenhouse–Geisser correction and Sidak's post hoc tests in SPSS (v.25, IBM, Armonk, NY, USA). Univariate correlations were calculated using Pearson's correlation, and the correlation coefficient (r) was presented. An $\alpha < 0.05$ was considered statistically significant.

3. Results

Growth of single hepatic tumors was successfully induced in all rabbits. Mean tumor size was (mean (SD)) 11 (3) mm and increased slightly between day 14 (8 (2) mm) and day 28 (12 (2) mm). The intrahepatic tumors showed a hypointense signal in unenhanced T1 images and were slightly hyperintense in T2 images. The anatomical images correlated well with the color-coded T1 maps in which the tumors were demarcated by their high signal from surrounding liver parenchyma (Figure 3).
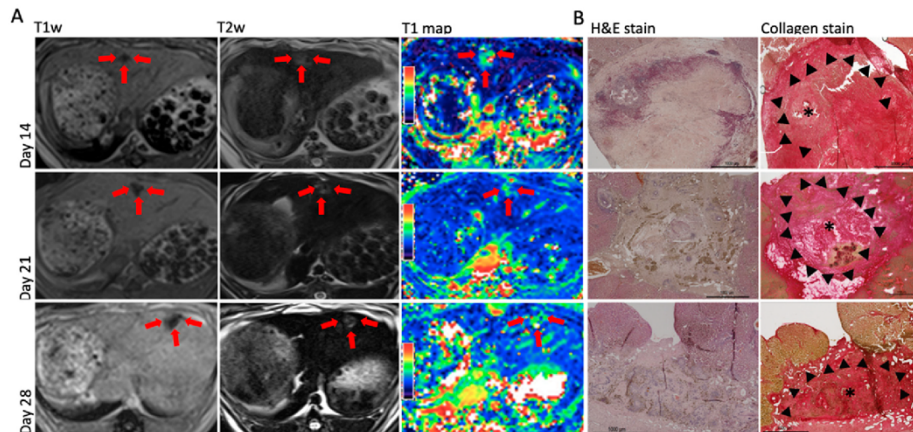
Figure 3. MRI and histological findings in experimentally implanted VX2 tumors at different time points (day 14, 21, and 28). (**A**) Axial MRI of implanted hepatic VX2 tumors (unenhanced T1wI, T2wI, color-coded T1map; (**B**) corresponding histopathological analysis: H&E stain and collagen stain. The asterisk marks the tumor center, the arrowheads the tumor margin.

3.1. Native T1 Mapping

Consistent with the image impression in the color-coded T1 map, averaged across all time points, the highest native T1 relaxation times were found in the tumor center (SD) (1721.7 (488.6) ms), followed by the tumor margin (1198.7 (291.3) ms). Shorter T1 times were found in the peritumoral region (779.7 (212.1) ms). Overall, all tumor-associated T1 times were above healthy liver parenchyma (525.9 (185.5) ms).

T1 mapping demonstrated significant differences between the segmented tumor center and margin as well as the peritumoral region and the liver parenchyma ($F(1.43, 34.26) = 106.93$, $p < 0.001$). There was no interaction effect between times and regions ($F(2.86, 34.26) = 0.74$, $p = 0.53$), nor an effect of time ($F(2, 24) = 2.14$, $p = 0.14$). T1 relaxation times were highest in the tumor center [mean (SD)] [1721.8 (488.6) ms] and decreased towards the periphery (margin: 1198.7 (291.3); peritumoral: 779.7 (212.1) ms; liver: 525.8 (185.5) ms) (Figure 4a). Post-hoc tests using Sidak's correction revealed significant differences between all three tumor regions ($p < 0.001$) (Table 1, Figure 4). T1 relaxation times in the tumor center and margin decreased slightly but not significantly over time.

3.2. Histopathological Analysis

The tumor areas were visualized in collagen-stained sections and corresponded to the respective slight in the acquired MR images (Figure 3b). We consistently found significant ($p < 0.001$) differences in collagen content in the regions investigated at all time points. The highest relative proportions of collagen fibers were consistently found in the tumor margin (31.8 (6.5)%) followed by the tumor center (22.8 (9.8)%). The peritumoral region showed the lowest collagen content (9.2 (2.5)%); however, this was still significantly higher compared to healthy liver parenchyma (0.23 (0.18)%).
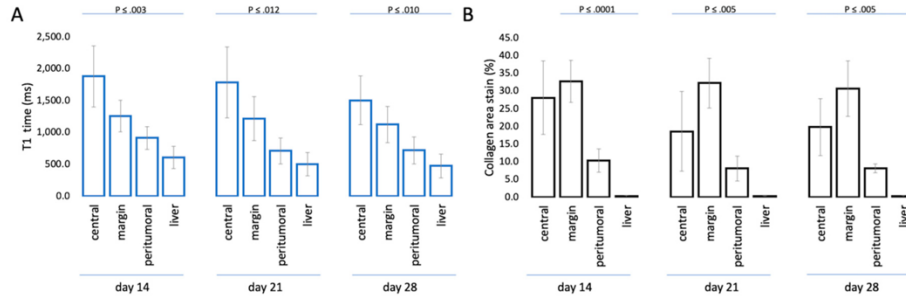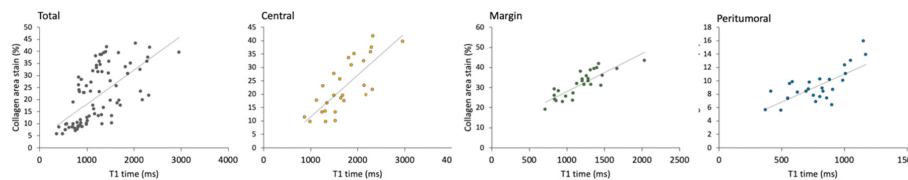
Figure 4. Association of T1 mapping and collagen staining in all animals. (**A**) Mean with standard deviation error bar of T1 times in different tumor areas 14, 21, and 28 days following tumor implantation; (**B**) mean with standard deviation error bar of the percentage collagen area stain (%) (Picrosirius red stain) at the three time points.

Table 1. Discriminatory power of T1 times (ms) between the tumor (center, margin) and peritumoral regions averaged for all time points.

Time Point	Region		Mean Difference (R1–R2) (ms)	95% Confidence Interval (CI)	*p* Value *
	R1	R2			
Day 14	center	margin	620.1	314.1–926.1	<0.001
		peritumoral	965.6	486.9–1444.4	<0.001
		liver	1272.8	778.6–1767.1	<0.001
	margin	peritumoral	345.5	100.4–590.7	<0.003
		liver	652.7	337.0–968.1	<0.001
	peritumoral	liver	307.2	134.5–479.9	<0.001
Day 21	center	margin	569.1	263.1–875.1	<0.001
		peritumoral	1074.7	595.9–1553.4	<0.001
		liver	1284.0	789.7–1778.2	<0.001
	margin	peritumoral	505.6	260.4–750.7	<0.001
		liver	714.8	399.2–1030.5	<0.001
	peritumoral	liver	209.3	36.6–382.0	0.012
Day 28	center	margin	379.7	73.7–685.8	0.010
		peritumoral	785.5	306.7–1264.2	0.001
		liver	1030.7	536.4–1524.9	<0.001
	margin	peritumoral	405.8	160.7–650.9	<0.001
		liver	650.9	335.2–966.6	<0.001
	peritumoral	liver	245.1	72.5–417.8	0.003

* Adjusted *p*-value using Sidak's method.

The in vivo T1 relaxation times of all segmented regions together correlated with histopathological ex vivo collagen stain area (r = 0.64, *p* < 0.001). Specifically, the T1 times of the marginal regions showed the highest correlation coefficient (r = 0.84, *p* < 0.001), followed by the central (r = 0.78, *p* < 0.001), and peritumoral (r = 0.73, *p* < 0.001) regions (Figure 5).

Figure 5. Association of T1 relaxation times and collagen area stain shown for all time points and areas.

4. Discussion

The main result of this study is that native T1 mapping based on specific T1 relaxation times allows the differentiation of tumor composition and the peritumoral region, which is not possible in such detail using conventional MR imaging. Native T1 mapping directly correlated with tumoral collagen content, making it a potential quantitative biomarker for ECM remodeling in hepatic tumors.

T1 longitudinal relaxation time is an intrinsic reflector of structural tissue composition in health and disease. The advent of the MOLLI pulse sequence has enabled fast and immediately available quantification of T1 tissue relaxation times in a single breath hold and thus facilitated clinical translation [29]. Currently, clinical T1 mapping is primarily used in cardiac imaging and has recently been incorporated into clinical cardiovascular guidelines. Further application areas have emerged with the use of T1 quantification to estimate liver function and the severity of liver fibrosis in humans [19–21] and animal models [22]. A recent study demonstrated superior diagnostic accuracy of T1 mapping over ultrasound elastography in early liver fibrosis [30].

Very few studies have so far investigated native T1 mapping to characterize the degree of tumor differentiation in high-grade renal cell carcinoma and neuroblastoma [24,25]. Data on native T1 mapping in clinical or experimental HCC are poor, and studies on the characterization of ECM composition using the MOLLI sequence are missing. In conjunction with a hepatocyte-specific contrast agent (Gd-EOB-DTPA), T1 mapping was shown to successfully differentiate various kinds of focal liver lesion based on morphologic imaging appearance. Using the percentage reduction T1 relaxation time (T1d%) in the hepatobiliary contrast agent phase combined with discriminant analysis, focal nodular hyperplasia, HCC, and cavernous hemangioma were distinguished with high sensitivity and specificity [31]. T1d% in the hepatocellular contrast agent phase also reliably predicted the degree of differentiation of HCC in the clinical setting [32].

Compared with published preliminary results of T1 mapping in the liver, quantitative T1 relaxation times measured without contrast agent administration show greater variation. For example, previous quantitative T1 mapping studies in the clinical setting calculated lower native T1 relaxation times (1008.6 (357.5) ms) for focal HCC compared to the values we obtained in a VX2 rabbit model. However, it must be noted that the study of Peng et al. [31] did not segment different tumor regions but averaged values across the whole tumor, which explains greater variability. Given the inherent tumor core necrosis of HCC, this approach might not be entirely representative in characterizing this type of tumor. Native T1 relaxation times found in a rabbit model of liver fibrosis by Li et al. [22] were very low (250.07 (88.12) ms) in the healthy liver parenchyma of control animals using nonenhanced liver acquisition volume acceleration (LAVA) with variable flip angle. In a recent study [30] quantifying fibrosis in a rat model using a look-locker sequence with an inversion recovery pulse comparable to our study, T1 relaxation times calculated for healthy liver parenchyma were similar to the values found in our study (525.8 (185.5) ms). The discrepancy with the aforementioned study may be attributable to technical sequence differences (e.g., LAVA versus MOLLI).

Native T1 values reflect the composite water signal from cells and extracellular space [33]. Higher native T1 values are primarily attributable to an increase in interstitial space, such as collagen, or the presence of edema [29]. In addition, other factors were shown to influence T1 relaxation such as inflammation, iron concentration, and steatosis, with higher T1 relaxation times in inflammation being primarily associated with interstitial edema [34–36]. In our study, we measured prolonged T1 times in

the tumor center with decreasing values towards the peritumoral region and the shortest T1 relaxation times in the liver parenchyma. This distribution of T1 times corresponds to the histopathological findings of central necrosis and higher tumor cell counts and fibrosis in the tumor margin. Published results on the hepatic VX2 tumor model for comparison are not available. In the setting of invasive tumor proliferation, unrestraint angiogenesis and chronic inflammation may be the two major factors that affect T1 relaxation times. The discrimination between tumor center and tumor margin may be explained by inherent central tumor necrosis frequently already present in early HCC. The longer T1 times in the less collagen-rich tumor center can be explained by the fact that water accumulation in biological tissues results in greater increases in T1 times than scarring or fibrosis [29]. Similar to acute myocardial infarction, cellular destruction by necrosis leads to higher water content and surrounding interstitial edema and consecutively to a focal increase in T1 relaxation times [33]. The good demarcation of the tumor margin can be explained in part by tumor hypervascularity along with an increased collagen content. Tumor neoangiogenesis is especially pronounced in the viable tumor rim, lengthening longitudinal relaxation time and thus contributing to demasking the tumor in T1 maps [31]. The increase in water content due to central necrosis and concomitant inflammation may have an additive effect on relaxation times that exceeds the effect of the vascular and collagen network in the tumor margin and may also partly affect the tumor rim, thus contributing to good overall detection. An interesting and important result of our study is that T1 mapping also distinguishes the peritumoral region, which tends to be occult in conventional T1 and T2 images, from adjacent healthy liver parenchyma. This finding is of particular interest for interventional studies on the model, which investigate the inflammatory response in the peritumoral ECM as a possible sign of therapy response.

Collagen—the primary ECM protein—has been found to play a key role in the promotion of tumor angiogenesis and tumor cell proliferation [3,4]. Furthermore, previous investigators have described the stimulation of abnormal collagen synthesis with the expansion of the collagen matrix in tumors. The higher extracellular collagen content prolongs longitudinal relaxation times and is directly proportional to the increase in tumoral T1 relaxation time [37]. Nakamori et al. demonstrated the ability of native T1 mapping to reliably detect and quantify the histological collagen volume fraction in the heart [15]. In this study, there was a direct correlation between native T1 relaxation times and extracellular volume with the biopsy-proven collagen volume fraction. Consistent with these results, we found a direct correlation of native T1 relaxation times with the histologically proven collagen content in the three hepatic tumor regions investigated. These results also provide valuable information on the composition of the tumor-associated ECM. Since the latter has already been linked with tumor aggressiveness and growth, native T1 relaxation times may be used as a potential quantitative parameter for the evaluation of ECM remodeling in response to both local and systemic therapies.

Our study has some limitations. MRI was performed in free breathing but in deep sedation, which considerably reduces respiratory motion artifacts. Overall tumor size was relatively small and varied across animals. Greater variability in tumor size has been shown for this rabbit model before and seems to be related to both necrosis rate and external factors [38]. In our study, interindividual variability in tumor composition, regarding the collagen content and central necrosis, as well as the tumor growth, was evident. However, systematic characterization of tumor variability and development was beyond the scope of our study, which focused on the feasibility of the MOLLI sequence for tumor tissue characterization in the experimental model. Furthermore, histologic fixation can distort anatomy, which may thus deviate from anatomy on images acquired in vivo. ROIs were therefore, as already done in preliminary studies [27], manually reconstructed for analysis as direct correlation of thistological sections with MR images is not possible. Furthermore, scarring may have a similar effect as increased collagen accumulation [39]; however, the sequence used cannot differentiate scarring from ECM expansion by excessive collagen production. Invasive tumor chunk implantation increases the risk of scarring, which may have affected T1 relaxation times in our experiments. However, there was no histopathological evidence of excessive scarring. Finally, as already mentioned above, T1 relaxation times are influenced by other factors such as iron concentration and steatosis [34–36].

While liver steatosis is unlikely in the young rabbits used in our study, a more accurate quantification of T1 relaxation times would probably be possible by simultaneous measurement of liver and tumor iron concentrations. This effect could be investigated further in future studies of T2* and T1 mapping in the VX2 tumor model.

5. Conclusions

Native T1 mapping is a reliable noninvasive method to quantify ECM components in different areas of hepatic VX2 tumors and thus contributes to the identification and characterization of primary liver tumors. Therefore, it can be used as a quantitative biomarker of ECM remodeling and a promising technique for future treatment studies.

References

1. Fang, M.; Yuan, J.; Peng, C.; Li, Y. Collagen as a double-edged sword in tumor progression. *Tumour Biol.* **2014**, *35*, 2871–2882. [CrossRef]
2. He, X.; Lee, B.; Jiang, Y. Cell-ECM Interactions in Tumor Invasion. *Adv. Exp. Med. Biol.* **2016**, *936*, 73–91.
3. Paszek, M.J.; Zahir, N.; Johnson, K.R.; Lakins, J.N.; Rozenberg, G.I.; Gefen, A.; Reinhart-King, C.A.; Margulies, S.S.; Dembo, M.; Boettiger, D.; et al. Tensional homeostasis and the malignant phenotype. *Cancer Cell.* **2005**, *8*, 241–254. [CrossRef] [PubMed]
4. Butcher, D.T.; Alliston, T.; Weaver, V.M. A tense situation: Forcing tumour progression. *Nat. Rev. Cancer* **2009**, *9*, 108–122. [CrossRef] [PubMed]
5. Page-McCaw, A.; Ewald, A.J.; Werb, Z. Matrix metalloproteinases and the regulation of tissue remodelling. *Nat. Rev. Mol. Cell Biol.* **2007**, *8*, 221–233. [CrossRef]
6. Yoshida, G.J. Regulation of heterogeneous cancer-associated fibroblasts: The molecular pathology of activated signaling pathways. *J. Exp. Clin. Cancer Res.* **2020**, *39*, 112. [CrossRef] [PubMed]
7. Sherman-Baust, C.A.; Weeraratna, A.T.; Rangel, L.B.; Pizer, E.S.; Cho, K.R.; Schwartz, D.R.; Schwartz, D.R.; Shock, T.; Morin, P.J. Remodeling of the extracellular matrix through overexpression of collagen VI contributes to cisplatin resistance in ovarian cancer cells. *Cancer Cell* **2003**, *3*, 377–386. [CrossRef]
8. Sethi, T.; Rintoul, R.C.; Moore, S.M.; MacKinnon, A.C.; Salter, D.; Choo, C.; Chilvers, E.R.; Dransfield, I.; Donnelly, S.C.; Strieter, R.; et al. Extracellular matrix proteins protect small cell lung cancer cells against apoptosis: A mechanism for small cell lung cancer growth and drug resistance in vivo. *Nat. Med.* **1999**, *5*, 662–668. [CrossRef]
9. Ma, H.P.; Chang, H.L.; Bamodu, O.A.; Yadav, V.K.; Huang, T.Y.; Wu, A.T.H.; Yeh, C.-T.; Tsai, S.-H.; Lee, W.-H. Collagen 1A1 (COL1A1) Is a Reliable Biomarker and Putative Therapeutic Target for Hepatocellular Carcinogenesis and Metastasis. *Cancers* **2019**, *11*, 786. [CrossRef]
10. Salarian, M.; Yang, H.; Turaga, R.C.; Tan, S.; Qiao, J.; Xue, S.; Gui, Z.; Peng, G.; Han, H.; Mittal, P.; et al. Precision detection of liver metastasis by collagen-targeted protein MRI contrast agent. *Biomaterials* **2019**, *224*, 119478. [CrossRef]
11. Messroghli, D.R.; Niendorf, T.; Schulz-Menger, J.; Dietz, R.; Friedrich, M.G. T1 mapping in patients with acute myocardial infarction. *J. Cardiovasc. Magn. Reson.* **2003**, *5*, 353–359. [CrossRef] [PubMed]

12. Ugander, M.; Bagi, P.S.; Oki, A.J.; Chen, B.; Hsu, L.-Y.; Aletras, A.H.; Shah, S.; Greiser, A.; Kellman, P.; Arai, A.E. Myocardial edema as detected by pre-contrast T1 and T2 CMR delineates area at risk associated with acute myocardial infarction. *Jacc Cardiovasc. Imaging* **2012**, *5*, 596–603. [CrossRef]

13. Karamitsos, T.D.; Piechnik, S.K.; Banypersad, S.M.; Fontana, M.; Ntusi, N.B.; Ferreira, V.M.; Ferreira, V.M.; Whelan, C.J.; Myerson, S.G.; Robson, M.D.; et al. Noncontrast T1 mapping for the diagnosis of cardiac amyloidosis. *Jacc Cardiovasc. Imaging* **2013**, *6*, 488–497. [CrossRef]

14. Bull, S.; White, S.K.; Piechnik, S.K.; Flett, A.S.; Ferreira, V.M.; Loudon, M.; Francis, J.M.; Karamitsos, T.D.; Prendergast, B.D.; Robson, M.D.; et al. Human non-contrast T1 values and correlation with histology in diffuse fibrosis. *Heart* **2013**, *99*, 932–937. [CrossRef] [PubMed]

15. Nakamori, S.; Dohi, K.; Ishida, M.; Goto, Y.; Imanaka-Yoshida, K.; Omori, T.; Goto, I.; Kumagai, N.; Fujimoto, N.; Ichikawa, Y.; et al. Native T1 Mapping and Extracellular Volume Mapping for the Assessment of Diffuse Myocardial Fibrosis in Dilated Cardiomyopathy. *Jacc Cardiovasc. Imaging* **2018**, *11*, 48–59. [CrossRef] [PubMed]

16. Child, N.; Suna, G.; Dabir, D.; Yap, M.L.; Rogers, T.; Kathirgamanathan, M.; Arroyo-Ucar, E.; Hinojar, R.; Mahmoud, I.; Young, C.; et al. Comparison of MOLLI, shMOLLLI, and SASHA in discrimination between health and disease and relationship with histologically derived collagen volume fraction. *Eur. Heart J. Cardiovasc. Imaging* **2018**, *19*, 768–776. [CrossRef]

17. Puntmann, V.O.; D'Cruz, D.; Smith, Z.; Pastor, A.; Choong, P.; Voigt, T.; Carr-White, G.; Sangle, S.; Schaeffter, T.; Nagel, E. Native myocardial T1 mapping by cardiovascular magnetic resonance imaging in subclinical cardiomyopathy in patients with systemic lupus erythematosus. *Circ. Cardiovasc. Imaging* **2013**, *6*, 295–301. [CrossRef] [PubMed]

18. Sibley, C.T.; Noureldin, R.A.; Gai, N.; Nacif, M.S.; Liu, S.; Turkbey, E.B.; Mudd, J.O.; Van Der Geest, R.J.; Lima, J.A.C.; Halushka, M.C.; et al. T1 Mapping in cardiomyopathy at cardiac MR: Comparison with endomyocardial biopsy. *Radiology* **2012**, *265*, 724–732. [CrossRef]

19. Ostovaneh, M.R.; Ambale-Venkatesh, B.; Fuji, T.; Bakhshi, H.; Shah, R.; Murthy, V.L.; Tracy, R.P.; Guallar, E.; Wu, C.O.; Bluemke, D.A.; et al. Association of Liver Fibrosis With Cardiovascular Diseases in the General Population: The Multi-Ethnic Study of Atherosclerosis (MESA). *Circ. Cardiovasc. Imaging* **2018**, *11*, e007241. [CrossRef]

20. Banerjee, R.; Pavlides, M.; Tunnicliffe, E.M.; Piechnik, S.K.; Sarania, N.; Philips, R.; Collier, J.D.; Booth, J.C.; Schneider, J.E.; Wang, L.M.; et al. Multiparametric magnetic resonance for the non-invasive diagnosis of liver disease. *J. Hepatol.* **2014**, *60*, 69–77. [CrossRef]

21. Pavlides, M.; Banerjee, R.; Sellwood, J.; Kelly, C.J.; Robson, M.D.; Booth, J.C.; Collier, J.; Neubauer, S.; Barmes, E. Multiparametric magnetic resonance imaging predicts clinical outcomes in patients with chronic liver disease. *J. Hepatol.* **2016**, *64*, 308–315. [CrossRef] [PubMed]

22. Li, Z.; Sun, J.; Hu, X.; Huang, N.; Han, G.; Chen, L.; Zhou, Y.; Bai, W.; Yang, X. Assessment of liver fibrosis by variable flip angle T1 mapping at 3.0T. *J. Magn. Reason. Imaging* **2016**, *43*, 698–703. [CrossRef] [PubMed]

23. Bedossa, P.; Poynard, T. An algorithm for the grading of activity in chronic hepatitis C. The METAVIR Cooperative Study Group. *Hepatology* **1996**, *24*, 289–293. [CrossRef]

24. Zormpas-Petridis, K.; Poon, E.; Clarke, M.; Jerome, N.P.; Boult, J.K.R.; Blackledge, M.D.; Carceller, F.; Koers, A.; Baorne, G.; Pearson, A.D.J.; et al. Noninvasive MRI native T1 mapping detects response to MYCN-targeted therapies in the Th-MYCN model of neuroblastoma. *Cancer Res.* **2020**, *80*. [CrossRef] [PubMed]

25. Adams, L.C.; Ralla, B.; Jurmeister, P.; Bressem, K.K.; Fahlenkamp, U.L.; Hamm, B.; Busch, J.; Makowski, M. Native T1 Mapping as an In Vivo Biomarker for the Identification of Higher-Grade Renal Cell Carcinoma: Correlation With Histopathological Findings. *Invest Radiol.* **2019**, *54*, 118–128. [CrossRef] [PubMed]

26. Geschwind, J.F.; Artemov, D.; Abraham, S.; Omdal, D.; Huncharek, M.S.; McGee, C.; Arepally, A.; Lambert, B.S.; Venbrux, A.C.; Lund, G.B. Chemoembolization of liver tumor in a rabbit model: Assessment of tumor cell death with diffusion-weighted MR imaging and histologic analysis. *J. Vasc. Interv. Radiol.* **2000**, *11*, 1245–1255. [CrossRef]

27. Deng, J.; Rhee, T.K.; Sato, K.T.; Salem, R.; Haines, K.; Paunesku, T.; Mulcahy, M.F.; Miller, F.H.; Omary, R.A.; Larson, A.C. In vivo diffusion-weighted imaging of liver tumor necrosis in the VX2 rabbit model at 1.5 Tesla. *Investig. Radiol.* **2006**, *41*, 410–414. [CrossRef]

28. Shanshan, L.; Feng, S.; Kaikai, W.; Yijun, Z.; Huiming, L.; Chuanmiao, X. Intravoxel Incoherent Motion Diffusion-weighted MR Imaging for Early Evaluation of the Effect of Radiofrequency Ablation in Rabbit Liver VX2 Tumors. *Acad, Radiol.* **2018**, *25*, 1128–1135. [CrossRef] [PubMed]

29. Haaf, P.; Garg, P.; Messroghli, D.R.; Broadbent, D.A.; Greenwood, J.P.; Plein, S. Cardiac T1 Mapping and Extracellular Volume (ECV) in clinical practice: A comprehensive review. *J. Cardiovasc. Magn. Reson.* **2016**, *18*, 89. [CrossRef]

30. Li, J.; Liu, H.; Zhang, C.; Yang, S.; Wang, Y.; Chen, W.; Li, X.; Wang, D. Native T1 mapping compared to ultrasound elastography for staging and monitoring liver fibrosis: An animal study of repeatability, reproducibility, and accuracy. *Eur. Radiol.* **2020**, *30*, 337–345. [CrossRef]

31. Peng, Z.; Li, C.; Chan, T.; Cai, H.; Luo, Y.; Dong, Z.; Li, Z.-P.; Feng, S.-T. Quantitative evaluation of Gd-EOB-DTPA uptake in focal liver lesions by using T1 mapping: Differences between hepatocellular carcinoma, hepatic focal nodular hyperplasia and cavernous hemangioma. *Oncotarget* **2017**, *8*, 65435–65444. [CrossRef]

32. Peng, Z.; Jiang, M.; Cai, H.; Chan, T.; Dong, Z.; Luo, Y.; Li, Z.-P.; Feng, S.-T. Gd-EOB-DTPA-enhanced magnetic resonance imaging combined with T1 mapping predicts the degree of differentiation in hepatocellular carcinoma. *BMC Cancer* **2016**, *16*, 625. [CrossRef] [PubMed]

33. Germain, P.; El Ghannudi, S.; Jeung, M.Y.; Ohlmann, P.; Epailly, E.; Roy, C.; Ganghi, A. Native T1 mapping of the heart—A pictorial review. *Clin. Med. Insights Cardiol.* **2014**, *8*, 1–11. [CrossRef] [PubMed]

34. Dekkers, I.A.; Lamb, H.J. Clinical application and technical considerations of T1 & T2(*) mapping in cardiac, liver, and renal imaging. *Br. J. Radiol.* **2018**, *91*, 20170825. [PubMed]

35. Unal, E.; Idilman, I.S.; Karcaaltincaba, M. Multiparametric or practical quantitative liver MRI: Towards millisecond, fat fraction, kilopascal and function era. *Expert Rev. Gastroenterol. Hepatol.* **2017**, *11*, 167–182. [CrossRef] [PubMed]

36. Henninger, B.; Kremser, C.; Rauch, S.; Eder, R.; Zoller, H.; Finkenstedt, A.; Michaely, H.J.; Schocke, M. Evaluation of MR imaging with T1 and T2* mapping for the determination of hepatic iron overload. *Eur. Radiol.* **2012**, *22*, 2478–2486. [CrossRef] [PubMed]

37. Robbers, L.F.; Baars, E.N.; Brouwer, W.P.; Beek, A.M.; Hofman, M.B.; Niessen, H.W.; van Rossum, A.C.; Marcu, B.C. T1 mapping shows increased extracellular matrix size in the myocardium due to amyloid depositions. *Circ. Cardiovasc. Imaging* **2012**, *5*, 423–426. [CrossRef] [PubMed]

38. Keller, S.; Chapiro, J.; Brangsch, J.; Reimann, C.; Collettini, F.; Sack, I.; Savic, L.J.; Hamm, B.; Goldberg, S.H.; Makowski, M. Quantitative MRI for Assessment of Treatment Outcomes in a Rabbit VX2 Hepatic Tumor Model. *J. Magn. Reason. Imaging* **2019**, *52*, 668–685. [CrossRef]

39. Tao, Q.; Lamb, H.J.; Zeppenfeld, K.; van der Geest, R.J. Myocardial scar identification based on analysis of Look–Locker and 3D late gadolinium enhanced MRI. *Int. J. Cardiovasc. Imaging* **2014**, *30*, 925–934. [CrossRef]

VII. Curriculum vitae

Mein Lebenslauf wird aus datenschutzrechtlichen Gründen in der elektronischen Version meiner Arbeit nicht veröffentlicht.

VIII. Publication list

Keller S, Borde T, Brangsch J, Adams LC, Kader A, Reimann C, Gebert P, Hamm B, Makowski M. Native T1 Mapping Magnetic Resonance Imaging as a Quantitative Biomarker for Characterization of the Extracellular Matrix in a Rabbit Hepatic Cancer Model. Biomedicines. 2020 Oct 13;8(10):412. (Impact factor: 4.717)

Keller S, Borde T, Brangsch J, Reimann C, Kader A, Schulze D, Buchholz R, Kaufmann JO, Karst U, Schellenberger E, Hamm B, Makowski MR. Assessment of the hepatic tumor extracellular matrix using elastin-specific molecular magnetic resonance imaging in an experimental rabbit cancer model. Sci Rep. 2020 Nov 27;10(1):20785. (Impact factor: 3.998)

Borde T, Laage Gaupp F, Geschwind JF, Savic LJ, Miszczuk M, Rexha I, Adam L, Walsh JJ, Huber S, Duncan JD, Peters DC, Sinusas A, Schlachter T, Gebauer B, Hyder F, Coman D, van Breugel JMM, Chapiro J. Idarubicin-Loaded ONCOZENE Drug-Eluting Bead Chemoembolization in a Rabbit Liver Tumor Model: Investigating Safety, Therapeutic Efficacy, and Effects on Tumor Microenvironment J Vasc Interv Radiol. 2020 Oct;31(10):1706-1716.e1. (Impact factor: 3.037)

Oral abstract presentations

ISMRM 2021
Borde T, Wu M, Ruschke S, Böhm C, Weiss K, Metz S, Makowski R, Karampinos D. Assessing breast density using the standardized proton density fat fraction based on chemical shift encoding-based water-fat separation.

RSNA 2020
Borde T, Nezami N, Laage Gaupp F, Savic L, Taddei T, Duran R, Lin M, Georgiades C, Hong K, Chapiro J. 3D Quantitative Tumor Burden Analysis to Optimize Allocation of Intermediate and Advanced Stage Hepatocellular Carcinoma to Locoregional Therapy: A Proposal to amend the Barcelona Clinic Liver Cancer Staging System.

CIRSE 2020
Borde T, Rukundo I, Laage Gaupp FM, Lwakatare L, Sanogo M. Percutaneous Transhepatic Biliary Drainage in Patients with Biliary Duct Obstruction in a Resource-limited Setting.

RSNA 2018

Borde T, Laage Gaupp F, Geschwind JF, Savic LJ, Miszczuk M, Rexha I, Adam L, Walsh JJ, Huber S, Duncan JD, Peters DC, Sinusas A, Schlachter T, Gebauer B, Hyder F, Coman D, van Breugel JMM, Chapiro J. Idarubicin-Loaded ONCOZENE Drug-Eluting Bead Chemoembolization in a Rabbit Liver Tumor Model: Investigating Safety, Therapeutic Efficacy, and Effects on Tumor Microenvironment.

WCIO 2018

Borde T, Laage Gaupp F, Geschwind JF, Savic LJ, Miszczuk M, Rexha I, Adam L, Walsh JJ, Huber S, Duncan JD, Peters DC, Sinusas A, Schlachter T, Gebauer B, Hyder F, Coman D, van Breugel JMM, Chapiro J. Effects of Idarubicin-Eluting Oncozene Microspheres on Pre-Clinical Tumor Microenvironment in Liver Cancer.

Prices

JVIR 2020 Editor's Award for Distinguished Laboratory Investigation supported by the Society of Interventional Radiology Foundation

IX. Acknowledgements/Danksagung